Dissertation

submitted to the
Combined Faculties for the Natural Sciences and for Mathematics
of the Ruperto-Carola University of Heidelberg, Germany

for the degree of
Doctor of Natural Sciences

Put forward by
Zhongyi Feng, M. Sc.
born in Beijing, China

Issued: 2018, Oral examination: Feb 5, 2019

Quantum technological dating of glacier ice from the last millennium and a new self-contained facility for routine measurements

Referees:

Prof. Dr. Markus Oberthaler

Prof. Dr. Norbert Frank

Abstract

The noble gas radioisotopes ^{85}Kr, ^{39}Ar and ^{81}Kr are of great importance in radiometric dating because their half-lives cover time scales from the last millennium to one million years before present. They are present as inert trace gases in the atmosphere and the exchange with other environmental reservoirs makes them ideal tracers for hydrology, oceanography and glaciology. Their very low isotopic abundance is the huge hindrance for the detection and analysis. Especially in the case of argon with a natural abundance of 8×10^{-16}, classical decay counting requires tons of water or ice and measurement times of several weeks. To reduce the sample size, techniques from the field of quantum optics are applied to capture the atoms directly rather than rely on their decay signature.
Argon Trap Trace Analysis is capable of daily measurements using samples as small as 0.5 mL STP argon and this is demonstrated here for glacier ice. A few kilograms of ice have been taken in artificial glacier caves and the measured argon ages are validated against preexisting constraints. These results and recent pilot studies have arisen a huge demand for small sample radio-argon dating. To meet this development, a second apparatus has been built in a self-sufficient laboratory container. The new machine is optimized for robustness and will increase the sample throughput capacities in the near-future. Furthermore, a setup has been built to characterize and improve the performance of the argon source, a main loss factor concerning efficiency.

Zusammenfassung

Die Edelgas Radioisotope ^{85}Kr, ^{39}Ar und ^{81}Kr sind von großer Bedeutung in der radiometrischen Datierung da ihre Halbwertszeiten Zeitskalen des letzten Jahrtausends bis zu einer Millionen Jahre vor unserer Zeit abdecken. Sie sind als Spurengase in der Atmosphäre vorhanden und der Austausch mit anderen Umweltreservoirs macht aus ihnen ideale Tracer für die Hydrologie, Ozeanographie oder Glaziologie. Das sehr geringe relative Isotopenverhältnis stellt dabei ein großes Hindernis für die Detektion und Analyse dar. Besonders im Fall von Argon mit einer natürlichen Häufigkeit von 8×10^{-16} benötigt klassische Zerfallszählung Tonnen von Wasser oder Eis und Messzeiten von mehreren Wochen. Um die Probengröße zu reduzieren werden Techniken aus dem Feld der Quantenoptik eingesetzt, welche ermöglichen die Atome direkt zu fangen statt auf deren Zerfallssignatur angewiesen zu sein.
Argon Trap Trace Analysis erlaubt es tägliche Messungen mit Proben so klein wie 0.5 mL STP Argon durchzuführen, was in dieser Arbeit für Gletschereis gezeigt wurde. Einige Kilogram Eis wurden in künstlichen Gletscherhöhlen genommen und das gemessene Argonalter gegen vorhandene Randbedingungen validiert. Diese Resultate und kürzliche Pilotstudien haben eine große Nachfrage an Radioargondatierung mit kleinen Probengrößen geweckt. Um dem entgegenzukommen wurde eine zweite Apparatur in einem unabhängigen Laborcontainer gebaut. Die neue Maschine ist auf Robustheit optimiert und wird den Probendurchsatz in naher Zukunft erhöhen. Weiterhin wurde ein Aufbau konstruiert, der es ermöglicht, die Performance der Argonquelle zu charakterisieren und zu verbessern, einem Hauptverlustfaktor der Effizienz.

Preface

I consider myself very lucky that I was given the opportunity to work on Argon Trap Trace Analysis because it is a truly unique experiment due to several reasons. From the viewpoint of a physicist, the Heidelberg collaboration between the Kirchhoff-Institute for Physics and the Institute of Environmental Physics is a prime example how interdisciplinary work is conducted to benefit so far untapped research fields. As someone like me, whose roots lie in the atomic physics, it was an inspiring and mind-opening experience to work with environmental physicists in joint projects and having input from far beyond the walls of an optical laboratory.

The challenge for an atomic physicist, besides mere measurement duties, is to increase the performance of the apparatus. The current state of a few counted atoms per hour in the case of argon is the main limitation concerning statistical uncertainties. It is a huge task to increase the efficiency of the setup either by optimizing the existing laser cooling and trapping stages or deploying new devices.

On a more technological side, the work in the optical laboratory requires knowledge and skills from all different kind of fields. It includes the expertise in laser cooling and trapping, the maintenance and setup of laser systems, the proper design and assembly of vacuum components, the ability to build electric control circuits and basic mechanical workshop proficiency. The climax has been the construction and setup of a completely new laboratory, where all of my acquired competences have been required.

The work and results presented in the following doctoral thesis describe what I have been working on during the last few years. The first part concentrates on the interdisciplinary aspect of Argon Trap Trace Analysis. Chapter 1 introduces the reader to the huge potential of noble gas radiometric dating. Chapter 2 concludes with the radio-argon dating of glacier ice by using samples of a few kilograms of ice.

The second part focuses on the atomic physical and technological aspects. Chapter 3 gives deeper insights on the theory of laser cooling and trapping and presents the required knowledge for understanding Argon Trap Trace Analysis. Chapter 4 reports on the construction and setup of a new apparatus in a self-sufficient laboratory container.

The last part focuses on potential improvements of the method. Chapter 5 presents the setup of a new test platform to characterize and possibly improve the argon source. Chapter 6 presents a short summary and gives an outlook for the project in the near future.

Acknowledgements

I would first like to thank my thesis advisors **Prof. Dr. Markus Oberthaler** and **Prof. Dr. Werner Aeschbach** for the opportunity to work on this unique and exciting project. Markus has guided me through most of my scientific career so far and discussions with him were always insightful and inspiring. Werner has opened my eyes for the many fascinating study areas outside the atomic physics laboratory that gave the work a motivating application.

I like to thank **Prof. Dr. Norbert Frank** for reviewing this thesis.

My late mother **Suju Ge** always wished for me to pursue a scientific career and it makes me immensely sad that she isn't here anymore to witness this step. I am eternally grateful for the support that she and my father **Yuanhua Feng** have given me during my whole life. I like to thank my sister **Katharina Feng** for all the happy time at home.

I am very grateful to my significant other **Angelika Klein** for everything since we met each other in the very first undergraduate physics class. Since that day our paths have been united and we grew together to the physicists, persons and partners that we are today.

Many thanks to my dear colleague **Dr. Sven Ebser** who has accompanied me during most of my time in the work group. We had countless inspiring and challenging discussions about our project over the years.

I like to thank **Dr. Helmut Strobel** for him having always the time for help and support. He inspired me a lot with his vast amount of knowledge about atomic physics, but also his technical expertise that is of great value in our laboratories.

I want to thank **Dr. Florian Ritterbusch** for introducing me to the topic of Atom Trap Trace Analysis and the good discussions about the project that we had over the years. Many thanks also to **Maximillian Schmidt** and **Lisa Ringena** for being such a great team during the ice project.

I also like to thank my other colleagues on the experiment over the years for all the exciting time in the laboratory and office: **Andreas Kamrad**, **Anke Heilmann**, **Florian Nicolai**, **Zhiguang Han**, **Felix Hahne**, **Timo Gierlich**, **Maurus Hans** and **Anika Frölian**.

I want to thank my colleagues from the Institute of Environmental Physics and our extended ATTA collaborators: **Dr. Arne Kersting**, **Stefan Bayersdorfer**, **Emeline Mathouchanh**, **Philip Hopkins**, **Viola Rädle**, **Dr. Pascal Bohleber**, **Dr. Helene Hoffmann** and **Dr. Andrea Fischer**.

The mechanical workshop, electrical workshop and administration have been an important part especially concerning the new laboratory container project. I want to thank all the people who were involved directly or indectly. Additionally, special thanks goes to: **Werner Lamade**, **Christian Herdt**, **Julia Bing**, **Siegfried Spiegel**, **Jürgen Riedl**, **Knut Azeroth**, **Alexander Dobler**, **Corinna Müller**, **Sabine Potthoff**, **Elke Schmetzer**, **Dagmar Hufnagel** and **Christiane Jäger**.

I want to thank everyone else in our work group for the great years that we spent together with conversations and discussions over coffee, seminars or the weekly breakfast. Unforgotten are the many sport events that we have participated in as a team.

I further like to thank some more people that have influenced me over the years:

- **Axel und Magdalena Klein** for accepting me into their family.
- **Michael Klein, Dilber Elmers and Sibel Klein** for all the exciting evenings in Saarland.
- **Dr. Tobias Rentrop** for introducing me to the gentleman's sport of mountain biking.
- **Dr. Daniel Linnemann** for the exploration of nearly all (non-mountain) bike routes surrounding Heidelberg.
- **Dr. Andrea Demetrio** for always lending a helping hand, figuratively speaking.
- **Simon Müller** for all the discussions on musical theory and making music together.
- **Marcell Gall** for all the conversations and support in good and bad times.

At last I want to thank everyone that I have accidentally forgotten!

Contents

List of Figures

List of Tables

Dedicated to my mother Suju Ge.

Du hast den Lebensgarten verlassen,
doch deine Blumen blühen weiter.

Part I

Application of Argon Trap Trace Analysis to Glacier Ice Dating

Chapter 1

Introduction of Noble Gas Radionuclides

The atmosphere of the Earth, a thin gas layer above the planetary surface, is a key environment for sustaining the global ecosystem. The resulting climate is the strongest and most felt environmental factor and has a huge impact on the human economy, culture and politics (Roedel and Wagner, 2017). The three most abundant gases in the atmosphere are nitrogen (78.1 %), oxygen (21.0 %), and argon (0.9 %) and the remaining constituents are commonly referred to as trace gases. These naturally or anthropogenically produced gases can hold valuable information about the climate, such as temperature, atmospheric radiation budget and air quality (Warneck, 1988; Möller, 2003; Seinfeld and Pandis, 2016).

The trace gases can enter other environmental reservoirs by the contact with the atmosphere. One example is the gas exchange on the water surface thus the tracers are contained in groundwater and the ocean. Another example is frozen air bubbles contained in fresh glacier ice, ultimately leading to the integration of the tracers into the ice matrix if the pressure inside the ice is high enough (Ohno, Lipenkov, and Hondoh, 2004).

In that sense, the age of an environmental reservoir or sample is commonly referred to as the time span since its last contact with the atmosphere. The dynamics of these reservoirs can be deployed to use them as climate archives and they provide knowledge about the paleoclimate of Earth where past human data and recordings have not been available. The missing key piece to the puzzle is to determine the age of the analyzed sample of the climate archive. A solution to this is provided by a group of radiometric age tracers. Their concentration in the sample is in equilibrium with the atmosphere, but as soon as the contact is broken, the decay of the isotopes on time scales according to their characteristic half-life reduce the concentration thus making the radiometric clock ticking.

Among the age tracers, the radioactive noble gases have ideal properties such as chemical inertness and known initial concentration. They are well mixed in the

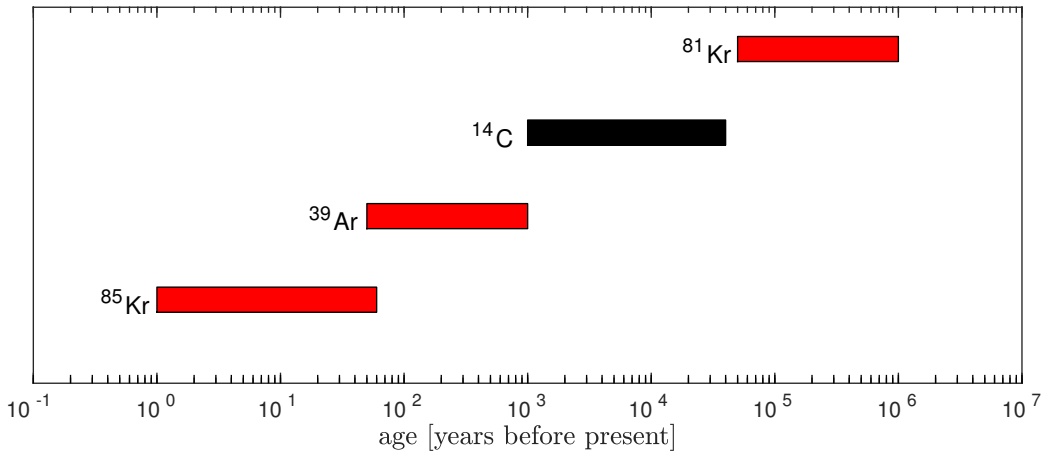

FIGURE 1.1: Dating ranges of radioisotopes. Together with ^{14}C, the noble gas trio ^{85}Kr, ^{39}Ar and ^{81}Kr cover the whole dating range from today to one million years before present.

atmosphere and are contained in water and ice. Furthermore, the half-lives of 10.76 years, 269 years and 229,000 years of the trio ^{85}Kr, ^{39}Ar and ^{81}Kr cover the whole dating range together with ^{14}C as can be seen in Figure 1.1.

Although the noble gas radionuclides posses almost perfect properties for dating purposes, their broad application has been strongly hindered by their very low atmospheric abundances. For ^{85}Kr and ^{81}Kr, it is 2×10^{-11} and 6×10^{-13} respectively. The isotopic abundance for ^{39}Ar is even three orders of magnitude lower[1] and is 8×10^{-16}. In the case of argon, this requires large sample volumes and long measurement times using classical decay counters thus applications with this tracer have been limited mainly to groundwater studies, where nearly unlimited sampling is possible (Alvarado et al., 2007).

The emerge of ^{85}Kr due to anthropogenic nuclear fission in the 1950's prevents the decay counting of the long-lived ^{81}Kr since then. This and the issues concerning sample size and measurement time have led to the development of Atom Trap Trace Analysis (ATTA) (Chen et al., 1999). It deploys techniques that have been developed in the field of atomic physics and quantum optics to capture single atoms of the desired isotope in an atom trap. The underlying laser cooling process requires multi-photon scattering and exploits small shifts in the optical resonance that arise due to differences in mass and nuclear spin between isotopes of the same element. The huge background of abundant isotopes is suppressed by million cycles of photon absorption and spontaneous emission.

The ATTA technique for krypton has been further developed since its introduction almost two decades ago and the state-of-the-art are routine measurements that

[1] One common example is to look for a marked one Euro coin that is hidden somewhere in Germany.

can be performed in two laboratories world-wide. One is located at the Argonne National Laboratory in Chicago, Illinois (Jiang et al., 2012; Lu et al., 2014) and the second is at the University of Science and Technology in Hefei, China (Jian, 2018).

The Heidelberg group has started radio-argon dating almost one decade ago and has successfully demonstrated this technique in three pilot studies concerning groundwater (Ritterbusch et al., 2014), ocean circulation (Ebser et al., 2018) and most recently, in this work, glacier ice (Feng et al., 2018). Although the proof of principle has been shown for the three environmental reservoirs, the low abundance of ^{39}Ar yields daily measurement cycles and is the main bottle neck for high sample throughput.

In the scope of this work, the increasing demand of radio-argon dating has been met by setting up a new apparatus. Furthermore, a test setup has been built to address questions that will hopefully lead to higher detection efficiency thus shortening the required measurement time for the same accuracy.

1.1 Noble Gas Properties

The elements He, Ne, Ar, Kr, Xe belong to the group of noble gases, characterized mainly by their inertness due to fully occupied valence electron shells. This chemical inactive behavior was the main reason for a late discovery although ~ 1 % of the atmospheric composition consists of noble gases. The most abundant proportion is argon and its atmospheric concentration is at least $\sim 450\times$ higher than the second most abundant noble gas element neon, as shown in Table 1.1. A non-reactive atmospheric component was first suspected in 1784 by H. Cavendish and the first detection of noble gases has been done in 1868 by Pierre Jannsen and Joseph Norman Lockyer by analyzing the spectral lines of the sun chromosphere (Sears, 2015). The new element was named helium after the Greek word for sun and was only later classified as noble gas. In 1895, Lord Rayleigh and William Ramsay discovered that nitrogen from chemical reactions has a different density than extracted nitrogen from atmospheric air hence they suspected a contribution of an element far less reactive than nitrogen. Further purification led to the discovery of argon although it was mixed with less than 1 % of the other noble gases (Rayleigh and Ramsay, 1895). The remaining noble gases were identified in 1898 (Ozima and Podosek, 1983).

The outstanding argon concentration compared to the other noble gases is due to the decay of potassium

$$^{40}\mathrm{K} + \mathrm{e}^{-} \rightarrow ^{40}\mathrm{Ar} + \gamma \tag{1.1}$$

TABLE 1.1: Proportion of noble gases in the atmosphere.

element	concentration [%]
argon	0.9340
neon	0.001818
helium	0.000524
krypton	0.000114
xenon	0.000009

with a half-life of 1.28 billion years (Dickin, 2018). The noble gas argon is therefore found in the Earth's crust from where it gets into the atmosphere thus more than 99 % of the atmospheric argon is ^{40}Ar. It is worth to note that the concentration of the other stable argon isotopes ^{36}Ar and ^{38}Ar are 0.003116 and 0.000059 respectively and therefore comparable to the other noble gases.

The availability of the noble gases in the atmosphere, their chemical inertness and the exchange with other environmental reservoirs makes this group of atoms very useful as tracers. A few examples are:

- **Noble gas thermometer.** The stable noble gases Ar, Kr and Xe have a strongly temperature dependent solubility in water. Their concentration in old groundwater can be used as paleoclimate indicator since it shows the temperature at the time of infiltration (Mazor, 1972).
- **K-Ar dating.** The decay of potassium to argon with a known decay time can be used to date the constituents of the Earth's crust (McDougall and Harrison, 1988).
- **Neutron field reconstruction.** The reconstruction of fast neutron fields due to the atomic-bomb in Hiroshima and their doses at distances is a valuable information for cancer studies. The field can be reconstructed using the ^{39}Ar concentration found in tomb stones on the graveyards in the city (Martinelli et al., 2003).

An important group of applications in environmental science uses the unstable thus radioactive isotopes of noble gases as dating method and is discussed in the next section.

1.2 Basics of Radiometric Dating

In the simplified case of a radioisotopic tracer with known half-life $t_{1/2}$ and constant initial concentration $c_0 = c(t = 0)$, the time dependent concentration $c(t)$ follows the decay curve

$$c(t) = c_0 \cdot \left(\frac{1}{2}\right)^{\frac{t}{t_{1/2}}} = c_0 \cdot e^{(-ln(2)\cdot\frac{t}{t_{1/2}})} \tag{1.2}$$

with the additional condition, that no sources of the used tracer exist in the environmental reservoir under study. The age t_{sample} of the sample with concentration $c_{\text{sample}} = c(t_{\text{sample}})$ is then

$$t_{\text{sample}} = ln\left(\frac{c_0}{c_{\text{sample}}}\right) \cdot \frac{t_{1/2}}{ln(2)}. \tag{1.3}$$

In the case of a tracer with significant variations in the initial concentration c_0 over time, calibration curves as in the case for ^{14}C are required to derive the age of the sample.

The relative precision of the inferred age t_{measured} is strongly dependent on measurement time T and actual sample age t_{sample}. For a counting detector with counting rate $\lambda_0 = \lambda(t_{\text{sample}} = 0)$, the number of detected signals is

$$N(T) = \lambda_0 T \cdot \frac{c_{\text{sample}}}{c_0} = \lambda_0 T \cdot e^{-ln(2)\cdot\frac{t_{\text{sample}}}{t_{1/2}}}. \tag{1.4}$$

If purely statistical errors are considered, the uncertainties of the detected signals is

$$\Delta N(T) = \sqrt{N(T)}. \tag{1.5}$$

The relative age error then yields

$$\frac{\Delta t_{\text{sample}}}{t_{\text{sample}}} = \frac{t_{1/2}}{ln(2)} \cdot \frac{1}{\sqrt{N(T)}t_{\text{sample}}}. \tag{1.6}$$

For the case of ^{39}Ar with a half-life $t_{1/2} = 269$ years and counting efficiency $\lambda_0 = 5\frac{\text{counts}}{h}$, Figure 1.2 shows the required measurement time T in hours for relative age errors of 10 %, 20 % and 50 % in dependence on the actual sample age t_{sample}.

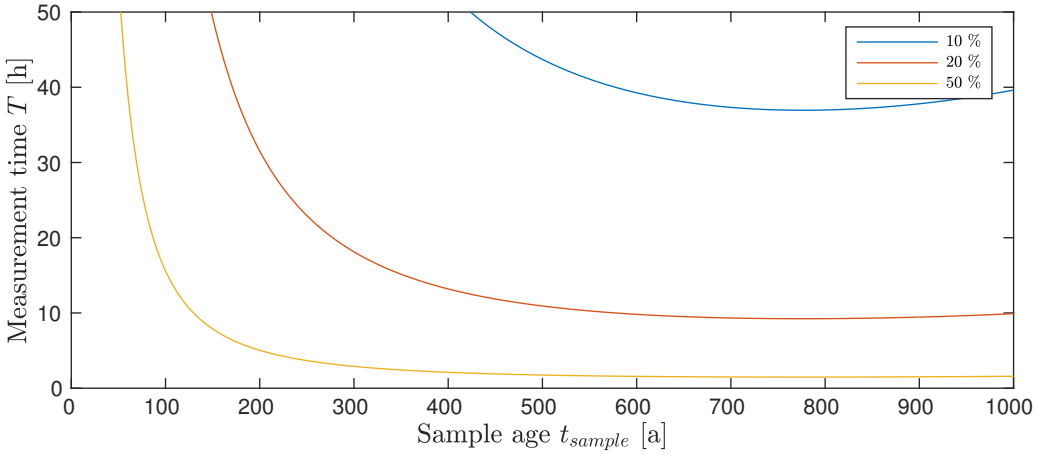

FIGURE 1.2: Relative age error of counting detectors. The required measurement times for relative errors of 10 %, 20 % and 50 % are shown in dependence on the actual sample age t_{sample}. The parameters for ^{39}Ar have been used, hence a half-life $t_{1/2} = 269$ years and a counting rate of $\lambda_0 = 5\frac{\text{counts}}{h}$.

TABLE 1.2: Radioisotopes for dating purposes

isotope	half-life [a]	dating range [a BP]	relative concentration [%]
^{85}Kr	10.76	$0 - 60$	2×10^{-11}
^{39}Ar	269	$50 - 1000$	8×10^{-16}
^{81}Kr	229,000	$50,000 - 1,000,000$	6×10^{-13}

1.3 Noble Gas Radionuclides

The radioactive isotopes ^{85}Kr, ^{39}Ar and ^{81}Kr serve as valuable tracers for dating purposes and their relevant properties are shown in Table 1.2. Together with the well-known ^{14}C, these radioisotopes cover the whole range from today to one million years before present as shown in Figure 1.1.

1.3.1 Krypton-85 - the Short-range Tracer

The short lived isotope ^{85}Kr has a half-life of 10.76 years and has the highest relative abundance among the trio of noble gas radioisotopes considered in this work. The atmospheric concentration is due to anthropogenic sources as it is one of the byproducts in nuclear fission of ^{235}U (Hippel, Albright, and Levi, 1985). The natural production of ^{85}Kr due to cosmic ray spallation in the atmosphere of the stable ^{84}Kr and ^{86}Kr yields only an estimation of 3×10^{-18} isotopic abundance (Kutschera et al., 1994) thus this process is negligible compared to nuclear fission. The main anthropogenic sources are atomic-bomb testing, nuclear reactors and reprocessing of fuel rods. Despite the short lifetime of ^{85}Kr, the atmospheric abundance has been

increasing steadily since 1950 nevertheless.

^{85}Kr can be used to identify young components in a sample due to the fact that it has not been available in sufficient amount in the atmosphere before the discovery of nuclear fission. Furthermore, it can be used to exclude any contamination of the samples with modern air using the sampling process, degassing or any other technical step.

1.3.2 Argon-39 - the Middle-range Tracer

^{39}Ar has a half-life of 269 years and its production is mainly due to cosmic ray spallation in the stratosphere (Loosli, 1983) according to

$$n + {}^{40}\text{Ar} \rightarrow 2n + {}^{39}\text{Ar}. \tag{1.7}$$

By comparing it with ^{14}C data over the last 1000 years, there is a slight variation in the atmospheric concentration of ^{39}Ar of up to 7 % (Oeschger et al., 1974), but this is usually negligible for dating purposes (Loosli, 1983).

Although argon has an outstanding atmospheric abundance among noble gases, the tracer ^{39}Ar has at least three orders of magnitude lower relative abundance compared to the krypton radioisotopes. In that sense, the high abundance of stable ^{40}Ar poses a hindrance as it cannot be separated chemically from the desirable radioisotope and is therefore a huge background for analytically methods.

Radiometric dating with ^{39}Ar offers a unique time span due to its half-life of 269 years thus covering the last millennium. A high demand for this tracer exists in the fields of groundwater studies, oceanography and glaciology since it matches the time scale of interest in these environmental reservoirs.

1.3.3 Krypton-81 - the Long-range Tracer

The long lived krypton isotope ^{81}Kr has a half-life of 229,000 years and the main atmospheric source is due to the cosmic ray spallation of ^{82}Kr, ^{83}Kr, ^{84}Kr and ^{86}Kr with p, n and γ and neutron capture ^{80}Kr(n, γ)^{81}Kr (Kutschera et al., 1994). By comparing preanthropogenic samples with modern krypton samples, the contribution of anthropogenic sources of ^{81}Kr are $\leq$ 2.5 % (Zappala et al., 2017) and are negligible. Furthermore, the short-term fluctuations of ^{81}Kr production in the atmosphere are smoothed out due to the long half-life and good atmospheric mixing thus a constant atmospheric abundance is given.

These properties make ^{81}Kr the ideal tracer in the range of fifty-thousand to one million years before present (Loosli and Oeschger, 1969) and its application has been demonstrated in many environmental studies including a million years old groundwater (Sturchio et al., 2004) and hundred thousand years old antarctic ice (Buizert et al., 2014).

Chapter 2

Radio-argon Dating of Alpine Glacier Ice

Radio-argon dating and glacier ice share a short but significant history together since the rise of the then novel tracer ^{39}Ar is closely tied to profound knowledge deducted from annual layer counting in polar ice cores (Oeschger et al., 1976; Loosli, 1983). Although calibration against existing age data from ^{32}Si and the δ^{18}O method was a huge success, the required amount of few tons of ice has excluded the field of glaciology since the beginning. A spatial and thus temporal resolution of most study sites is necessary to access the information stored in the ice and can only be realized by reducing the sample size down to a few kilograms. Argon Trap Trace Analysis (ArTTA) is the long-awaited key to these valuable climate archives and this chapter presents pilot studies on two unique sites at Chli Titlis glacier (3030 m asl, Central Switzerland) and Schaufelferner glacier (2870 m asl, Stubai Alps, Austria).

2.1 Site Description and Sample Selection

A crucial part for the execution of this project has been a collaboration with the Interdisciplinary Mountain Research group in Innsbruck, Austria and the local ice facilities for storage and preparation at the Institute of Environmental Physics in Heidelberg. The two chosen sampling sites shown in Figure 2.1 at Chli Titlis and Stubai had been the subject of previous glaciological investigations (Hoffmann, 2016) and offer practical prerequisites for this pilot study of radio-argon dating. Artificial ice tunnels have been created for touristic purposes and provide easy logistic access and sampling conditions independent from weather. The latter has led to hastily sampling in a first attempt and might be the reason for unsuccessful dating (Ebser, 2018). Organic findings in the form of micro-carbonic material (Titlis) or a bark particle and larch needle (Stubai) and visual stratigraphy in both caves provide valuable prior knowledge of the sampling sites (Bohleber, Hoffmann, and Kerch, 2018; Hoffmann, 2016) and constrain the expected age for radio-argon. However, due to the lack of data

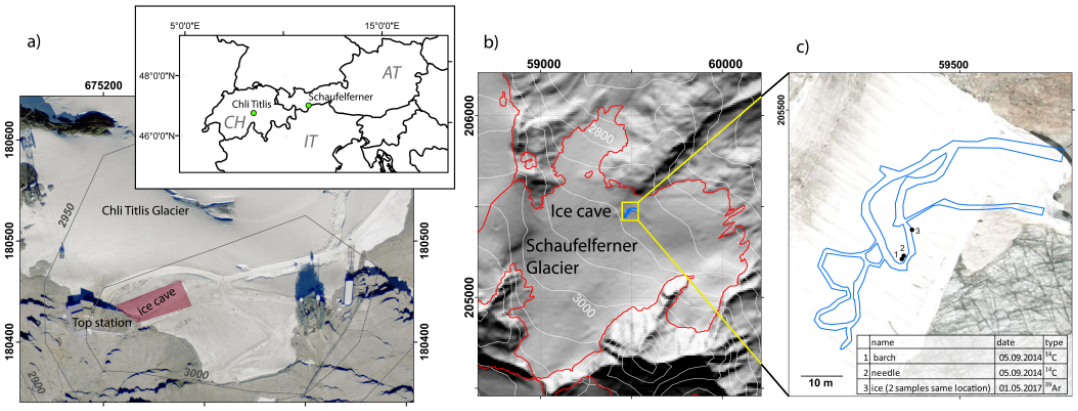

FIGURE 2.1: Site maps of a) Chli Titlis glacier cave and b) Schaufelferner glacier cave with c) a schematic view of the Schaufelferner ice tunnel and sample locations. Due to the summit location, the ice at the Chli Titlis cave is nearly stagnant, showing horizontal layers allowing straightforward sampling and relative age control via stratigraphy, i.e. older ages at greater depth. The Schaufelferner glacier cave is located downstream of the summit and has undergone substantial ice flow. Inclined layers undisturbed by folding are visible within the cave. The GPS coordinates for Chli Titlis and Schaufelferner are reported in the Swiss grid and Gauss-Krueger system, respectively. Taken from Feng et al., 2018.

and huge ambiguities in the ^{14}C calibration especially below $\sim 1,000$ years BP[1], the sole confirmation of the expectations based on existing knowledge is valuable and gives more comprehension for the studied locations. The ^{39}Ar has been extracted from abundant layers of white, bubble-rich ice. The following descriptions of the sampling sites have been adapted from Feng et al., 2018.

2.1.1 Chli Titlis

The cornice-type summit at Chli Titlis in Central Switzerland holds the glacier on the slope facing north where the investigated tunnel has been dug around 100 m into the ice at 3030 m asl. The entrance of this glacier cave is at the cable car station and it runs along bedrock.

The temperature in the caves is below zero throughout the year. Nevertheless, artificial air conditioning has been applied to compensate for the heat input of visiting tourists. Additionally, sheets cover the glacier surface to minimize summer ice melt. Despite these efforts, the negative mass balance leads to shrinking of the glacier and thus the stored record is vanishing.

[1]It is worth to note that the radiocarbon community defines before present (BP) as before the calibrated year 1950 CE. In the scope of this work, all ages refer to before 2018 CE for simplicity.

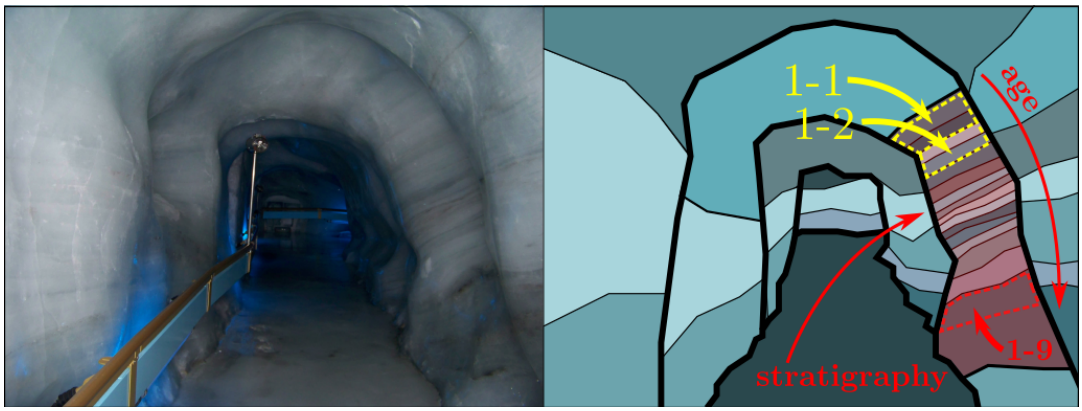

FIGURE 2.2: The sampling site at the summit of Chli Titlis. The wall in the cave shows a distinct horizontal layering, hence no evidence of layer folding. The ^{14}C age constraints reveal a strong vertical age gradient within the sampled depths. The two uppermost blocks (1-1 and 1-2) have been analyzed for ^{39}Ar. The results of 527^{+119}_{-156} years before 2018 CE for the uppermost block 1-1 and 1126^{+1286}_{-273} years before 2018 CE for block 1-2 are realistic in view of existing age evidence provided by visual stratigraphy and ^{14}C dating results. Taken from Feng et al., 2018.

The ice flow in this summit region is nearly stagnant and the walls in the cave show distinct horizontal layering as shown in the left part of Figure 2.2. This provides a clear visual stratigraphy and thus relative age control. Accordingly, the sampling strategy at this site was to obtain two blocks of neighbouring layers significantly different in age. Micro-radiocarbon dating in a previous study (Bohleber, Hoffmann, and Kerch, 2018) revealed a strong age gradient within a sampled profile of $\sim$ 2 m as sketched as shaded area in the right part of Figure 2.2. The revealed age ranges between 1248 years BP (block 1-2) and 3138 years BP (block 1-9). Even older ice with age of 5387 years BP can be found further inside of the glacier cave.

The two uppermost and thus youngest blocks 1-1 and 1-2 with weight of $\sim$ 5 kg were obtained using a chainsaw. Prior to the sample collection, the outermost layer exposed towards the tunnel has been removed to avoid contamination via cracks or melt water.

2.1.2 Schaufelferner

Schaufelferner in the Stubai Alps, Austria, is part of the Stubai glacier ski resort. The glacier covers altitudes between 2810 m asl and 3270 m asl. The glacier tongue of Schaufelferner is divided into two parts at the Eisgrat nunatak, an exposed ridge of the underlying mountain. In 2013, the ice tunnel at 2870 m asl has been drilled close to the cable car station, on the orographic right side of the nunatak. To protect the glacier from rapid shrinking due to negative mass balance, ice exposed to the surface is covered by sheets. The seasonal variability of englacial temperature

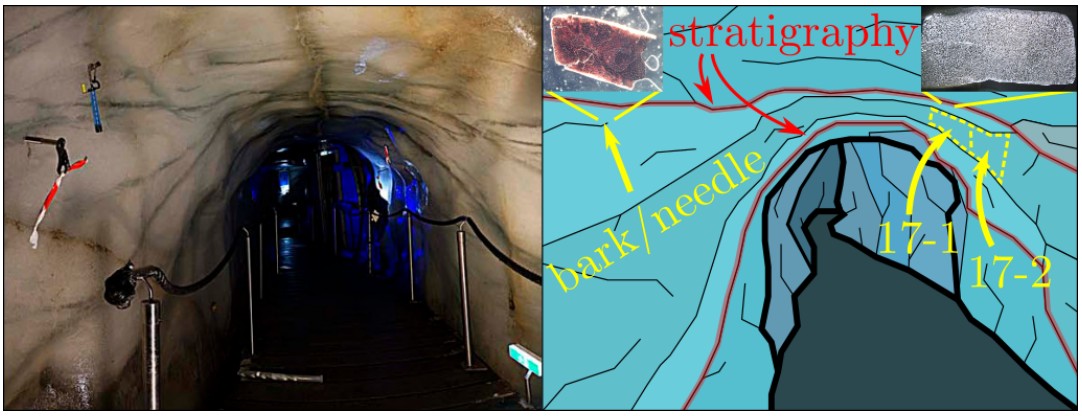

FIGURE 2.3: The Schaufelferner glacier cave. A bark particle and a larch needle have been extracted from the wall and allow for macroscopic ^{14}C dating. The ice blocks used for ^{39}Ar dating have been taken in a later campaign and samples of required size have been taken few meters apart from the original location. Great care has been applied to select a layer for ^{39}Ar as close as possible to the layer comprising the organic objects. The ^{39}Ar dating results of 193^{+53}_{-55} and 198^{+60}_{-64} years before 2018 CE agree with ^{14}C findings (see main text). Taken from Feng et al., 2018.

is subject to investigations and continuous temperature monitoring is currently underway. The clear evidence for the retreat of this glacier means that the access to this unique paleo-climate information reservoir is limited in time.

The glacier has undergone substantial deformation by flowing downwards from the top yielding tilted layering without folding as can be seen in the left part of Figure 2.3. Nevertheless, the layers are intact and are sketched in the right part of Figure 2.3. In this glacier cave, the rare finding of macroscopic objects of organic origin, a bark fragment and a larch needle, allow for conventional radiocarbon dating to constrain the age of the glacier ice (Hoffmann, 2016). The ^{14}C ages of the bark and needle are $375 - 532$ years BP and $505 - 632$ years BP at 68 % and 48 % probability respectively. The ice is therefore expected to be in the mid-range of the accessible time scale by ^{39}Ar. The sampling strategy in this glacier caves was to obtain two suitable ice blocks of the same layer in close proximity to the organic material. For radio-argon dating, the two adjacent blocks 17-1 and 17-2 were cut within one layer with roughly 4 m horizontal distance from the macroscopic particles as sketched in the right part of Figure 2.3.

2.2 Sample Preparation and Argon Extraction

The samples have been transported as ice blocks from the glacier sites to Heidelberg and were stored in a storage room at -20 °C at the Institute of Environmental Physics.

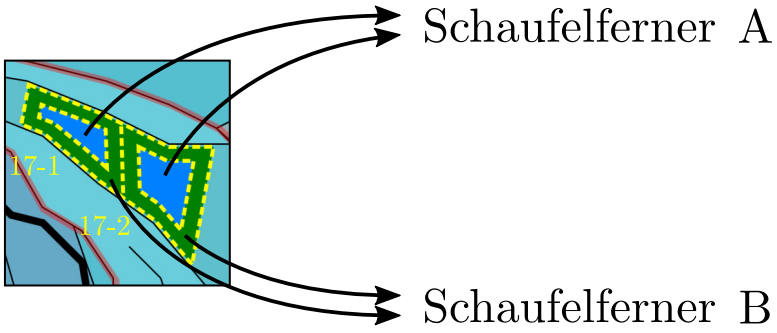

FIGURE 2.4: Preparation of Schaufelferner ice. The two adjacent ice blocks originated from the same layer hence the same age was expected. The core parts were obtained by carefully removing the outermost layer of both blocks and yield the Schaufelferner A sample. The removed layers were combined to Schaufelferner B sample. The so prepared samples were suitable to test the sampling method by chainsaw and the necessary degree of decontamination, i.e. if the outermost layer has to be removed.

The Titlis ice blocks 1-1 and 1-2 were expected to have strongly different ^{39}Ar concentrations due to the preexisting age constraints. They were prepared following a conservative decontamination approach by removing the outermost layer of the ice block. By this method, the risk of mixing by modern air due to cracks in the ice or refrozen meltwater is minimized.

The Schaufelferner ice block 17-1 and 17-2 were taken next to each other from the same layer thus no significant age difference was expected. They were prepared by two different approaches as shown in Figure 2.4. A cm-thick layer from both ice blocks was removed and the obtained core parts were combined to the sample Schaufelferner A. To test the necessary degree of decontamination and the required effort while sampling, the removed surface layers were collected, cleaned of sections evidently containing refrozen ice and combined to the sample Schaufelferner B.

The results discussed in the next section yield no difference of the ^{39}Ar concentration in samples A and B hence not much ice needs to be removed to prevent modern air contamination. Convenient and handy ice block sizes of $\sim$ 5 kg are sufficient and can be obtained by convenient chainsaw sampling.

For further sample processing, the ice had been melted in a high-vacuum environment and released air from the last millennium was collected. A two-step extraction and purification by titanium sponge getters was applied to retrieve the desired argon gas. More details on the performed ice preparation can be found in Hopkins, 2018.

2.3 ArTTA Measurements

The prepared argon samples are measured using the ultra-sensitive ArTTA method which is capable of resolving the ^{39}Ar concentrations on the part-per-quadrillion level. The techniques from the field of quantum optics are applied to control and manipulate the desired isotope solely in an ultra-high vacuum environment. Although a single resonant optical excitation is not sufficient to overcome the huge difference in abundance, multi-photon scattering solves this issue. The working principle of a magneto-optical trap (MOT) unifies this crucial process conveniently with fluorescence light suitable for detection. The very rare abundance of the radio isotope leads to only a few detected thus trapped ^{39}Ar atoms per hour and requires measurements as long as 20 hours for sufficient statistics.

2.3.1 Description of the ArTTA Setup

A simplified scheme of the ArTTA apparatus is shown in Figure 2.5. The purified argon gas sample is first compressed into a buffer volume to compensate for different sample sizes while obtaining a constant flow into the main apparatus. Argon needs to be prepared for laser cooling since the first excitation level lies deep in the vacuum ultra-violet (VUV) and beyond practically obtainable optical wavelengths. An rf-discharge provides enough energy to excite the atoms to a metastable state (Ar*) where convenient optical transitions in the near-infrared (NIR) exist. Liquid-nitrogen cooling is applied to reduce the initial velocity of the atoms.

The core of ArTTA is a magneto-optical trap (MOT) two and a half meters downstream. The capture velocity of the MOT is a few tens of meters per second. A crucial part is therefore decelerating the atoms down from thermal velocities. This cooling process has to compensate for optical Doppler shifts and is performed by a Zeeman slower (ZSL). Atoms exiting the ZSL have kinetic energies low enough to be captured in the potential well provided by the MOT. There, millions of photons are scattered resonantly in a spatially confined region and yield perfect selectivity with fluorescence light as a byproduct that is used for the detection of single ^{39}Ar atoms.

The flux into the small detection region is further increased by two transverse laser cooling stages. The first stage collects the divergent atoms from the effusive source and collimates them into a beam. The second stage compresses the beam into the trappable MOT area. To reduce off-resonant scattering in the detection region, the huge isotopic background of abundant ^{40}Ar is deexcited to the ground-state by an additional laser. The fluorescence of this process provides a direct signal for flux monitoring.

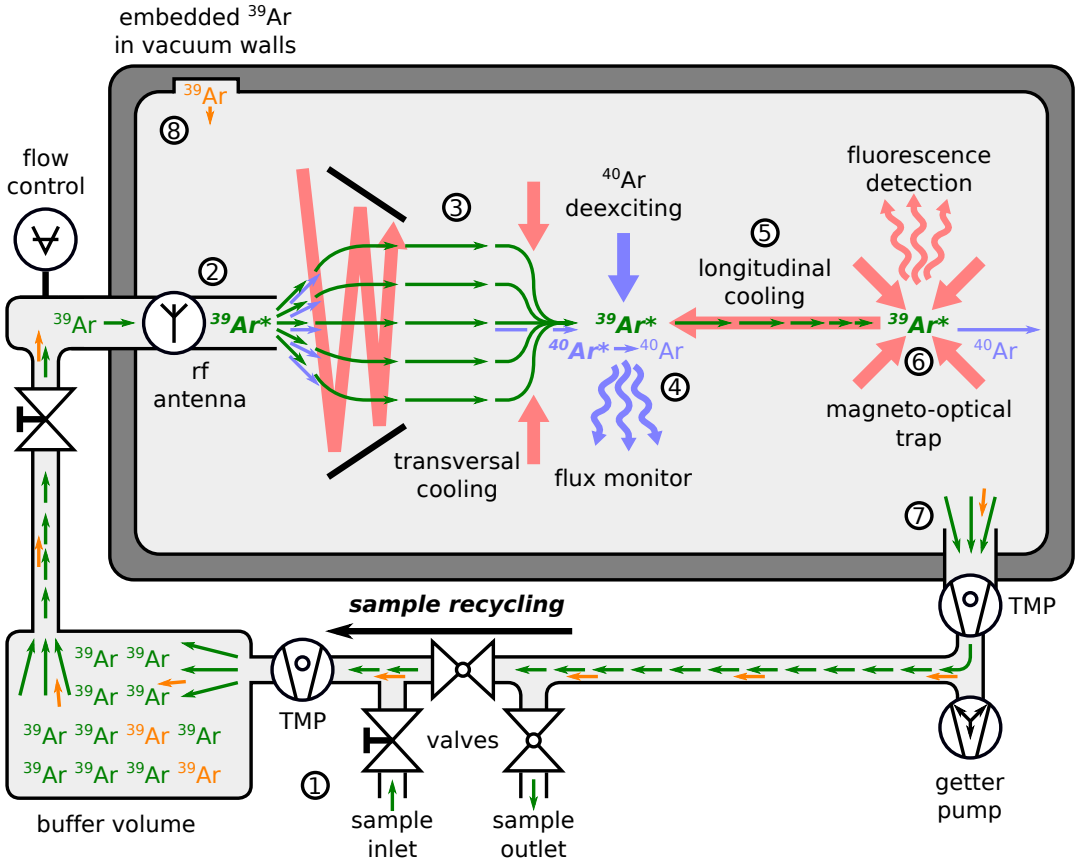

FIGURE 2.5: Setup of the Argon Trap Trace Analysis. (1) The sample is compressed into a buffer to compensate for different sample volumes. (2) Argon is excited into a metastable state for convenient optical transitions at 812 nm. (3) Transverse laser cooling is applied to increase the ^{39}Ar flux into the detection region. (4) ^{40}Ar is deexcited to the ground state and provides a signal for flux monitoring. (5) Longitudinal laser cooling slows the thermal atoms down to tens of meters per second. (6) Single ^{39}Ar atoms are captured in a magneto-optical trap and the fluorescence is monitored by a photodiode. (7) Several turbo-molecular pumps (TMP) collect the gas from the apparatus. The sample is cleaned by a getter pump and is re-compressed to the buffer volume. (8) Enriched ^{39}Ar out-gasses from the vacuum walls and contaminates the sample. This effect scales with volume and limits the analysis for smaller samples. Taken from Feng et al., 2018.

Several turbo-molecular pumps (TMP) collect the sample and a Non-Evaporable Getter removes any non-noble gas contribution due to out-gassing of the vacuum apparatus. The reclaimed and restored gas is compressed into the buffer volume again thus enabling full recycling of the sample. Due to this, the required sample size is reduced by several orders of magnitude and in principle, volumes below 0.1 mL STP argon can be handled by the setup. However, the practical sample size of the current ArTTA setup is limited by out-gassing of embedded enriched ^{39}Ar and accumulation of these atoms over time leads to an increasing background thus the integration time is limited. This is discussed in the following section.

2.3.2 Analysis of Sample Concentration

The analysis of ^{39}Ar concentration in a sample is biased by a contribution of previous embedded ^{39}Ar atoms and their out-gassing during a measurement. This argon gas enriched in ^{39}Ar can be attributed to a long-term memory effect, commonly referred to as "contamination", and a short-term memory effect, commonly referred to as "cross-sample contamination". More details concerning the origin and contribution of both effects can be found in Ebser, 2018.

In the scope of this work, a simplified model is used by assuming a constant out-gassing rate a_{out}. The additional ^{39}Ar atoms are diluted by the sample volume V_{sample}. This artificial concentration is increasing linearly in time and has to be added to the sample concentration c_{sample} yielding the time-dependent concentration

$$c(t) = c_{\text{sample}} + \frac{a_{\text{out}}}{V_{\text{sample}}} t. \tag{2.1}$$

A rate equation can be formulated by using the reference count rate λ_0 and integration over time $t = T$, leading to the total number of detected atoms

$$N_{\text{total}} = \left[c_{\text{sample}} T + \frac{1}{2} \frac{a_{\text{out}}}{V_{\text{sample}}} T^2 \right] \cdot \lambda_0. \tag{2.2}$$

The two independent parameters a_{out} and λ_0 have to be experimentally determined. An ^{39}Ar free sample is used to infer the parameter a_0. This sample with basically zero concentration has been provided (in sufficient amount) by the dark matter research collaboration Darkside (Agnes et al., 2016). With this, equation 2.2 yields the number of background atoms

$$N_{\text{background}} = \frac{1}{2} \frac{a_{\text{out}}}{V_{\text{sample}}} T^2 \cdot \lambda_0. \tag{2.3}$$

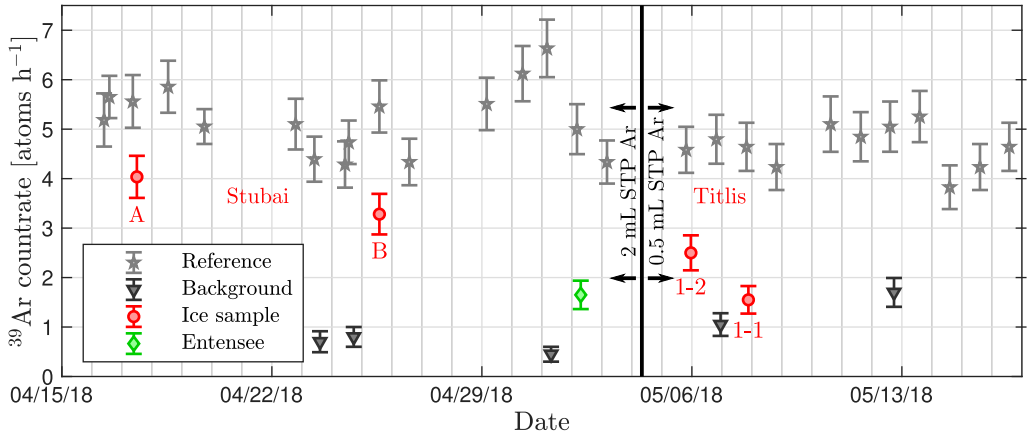

FIGURE 2.6: Time line of the ice dating project. In between sample measurements (circles), the two important parameters for the outgassing rate a_{out} and modern count rate λ_0 have been inferred from background (triangle) and reference measurements (stars). The apparatus has been operated in weekly measurement runs and the references of the runs are averaged to a local mean reference. The buffer volume has been replaced to handle sample sizes as small as 0.5 mL STP argon as in the case of Titlis. Additionally, a sample from the local waterworks Entensee has been analyzed.

The modern count rate λ_0 can be inferred independently by using samples of known concentration c_{sample}. For this purpose, a new reference sample $c_{10\times}$ with $10\times$ enrichment in ^{39}Ar compared to modern concentration has been established in Ebser, 2018. It uses argon gas highly enriched in ^{39}Ar that has been provided by (Williams et al., 2017) in the scope of an intercomparison study. The high enrichment leads to convenient short measurement times where the second term in equation 2.2 can be neglected. The number of these reference atoms is then

$$N_{\text{reference}} = c_{10\times} T \cdot \lambda_0 \tag{2.4}$$

thus providing a direct method to determine λ_0.

2.3.3 Measurement Runs and Time Line

Reference and background measurements have been performed multiple times alongside sample measurements and the time line of the ice dating project is shown in Figure 2.6. The buffer volume has been changed during that period to analyze samples as small as 0.5 mL STP.

The apparatus has been operated in a weekly cycle and the mean of all references of such a measurement run has been used as local reference. In principle, this can

TABLE 2.1: Results of glacier ice dating

sample name	conc. [%]	age [a]	atoms (bg)	T [h]	V [mL]	Wt [kg]
Titlis 1-1	$25.7^{+9.2}_{-8.5}$	527^{+119}_{-156}	50 (26)	20.00	0.5	4.3
Titlis 1-2	$5.5^{+5.6}_{-5.3}$	1126^{+1286}_{-273}	31 (25)	20.00	0.6	4.2
Schaufel. A	$60.8^{+8.9}_{-8.0}$	193^{+53}_{-55}	92 (13)	22.30	1.7	6.7
Schaufel. B	$60.0^{+10.1}_{-9.1}$	198^{+60}_{-64}	66 (10)	19.50	1.4	5.9

be done directly by applying equation 2.4 due to the good counting statistic by the typical high number of hundreds of detected atoms. But consequently for all measurements, a more advanced Bayesian analysis of the probability density function from Ebser, 2018 is used to infer the most probable reference and therefore modern count rate λ_0.

The contribution of the background is inferred from all measurements with the ^{39}Ar free sample. The most probable value is again calculated by a Bayesian analysis of the probability density functions. Notably, the out-gassing rate a_{out} is not affected by the change of the buffer volume and only depends on the actual sample size.

The raw data of the sample measurements, i.e. detected ^{39}Ar atoms, have been analyzed using the statistical model described in equation 2.2 by employing the experimentally determined parameters. In the scope of this work, the most probable values for the concentration and uncertainties corresponding to the 1σ confidence interval containing 68.3 % of measurements are reported.

2.4 Radio-argon Dating Results and Discussion

The extracted argon from the ice samples has been analyzed according to the method described in the previous section and the results are shown in Table 2.1.

The ^{39}Ar ages can be put into context with the existing age constraints given by the two different ^{14}C dating techniques, i.e. microscopic and macroscopic, and the relative age control via stratigraphy in both caves.

For the ice blocks from Chli Titlis, the ArTTA results correspond to the old end of the time span accessible by ^{39}Ar. The ^{39}Ar ages of 527^{+119}_{-156} years BP for block 1-1 and 1126^{+1286}_{-273} years BP for block 1-2 yield a minimal age difference of 207 years BP. These two adjacent blocks span a total height of $\sim$ 35 cm and the results are in agreement with what is expected due to the microscopic ^{14}C ages. The block 1-2 has been radiocarbon-dated to $1248 - 1373$ years BP and block 1-9 to $2929 - 3138$ years

BP, yielding an age gradient of $10 - 12$ years/cm. The material used for micro-radiocarbon dating of the ice samples has been prepared with combustion temperatures of ~ 800 °C and is also subject for reservoir effects. The radiocarbon ages are thus regarded as upper age limits (Hoffmann et al., 2018; Bohleber, Hoffmann, and Kerch, 2018). Furthermore, the visual stratigraphy of the near-horizontal layering provides an important relative age control thus constraining block 1-1 to younger ages than block 1-2, excluding layer folding of the glacier ice. This is again a match by the radio-argon findings which even reveals the previous unknown age of block 1-1.

The ^{39}Ar dating results for the ice from Schaufelferner glacier are mutually consistent and reveal argon ages of 193^{+53}_{-55} years BP for sample A and 198^{+60}_{-64} years BP for sample B. They match the ^{14}C dating results based on reasonable glaciological considerations of the sampling location. The very rare organic findings originate from a neighbouring layer and are conventionally radiocarbon dated to $375 - 532$ years BP for the bark particle and $505 - 632$ years BP for the larch needle. The probabilities are 68 % and 48 % respectively and arise mainly due to ambiguities in the calibration of ^{14}C ages within the time period. The reported values are the most likely age ranges calculated by OxCal v4.3.2 (Bronk Ramsey, 2017) using the IntCal13 atmospheric calibration curve (Reimer et al., 2013). More details can be found in Hoffmann, 2016 and Appendix A. Additionally and regardless of calibration issues, the ^{14}C dating results of the macroscopic particles have to be considered as upper age estimates due to potential delayed deposition into the glacier ice after their creation.

The radio-argon dated ice samples agree with the preexisting knowledge and constraints thus confirming the ArTTA ice dating method for the mid- (Schaufelferner) and far-end (Titlis) age range. The A and B sample from Schaufelferner further imply that convenient sampling by chainsaw is possible and that practical sample sizes of ~ 5 kg are sufficient. Micro-cracks due to the method are not significant and sample preparation needs only to remove those parts evidently containing modern air.

The argon age at Titlis provides further information about the uppermost block that has not been accessible by radiocarbon dating. The results at Schaufelferner support the existing presumption that the ice is a remnant of the 1850 glacier maximum thus originates from the Little Ice Age glacier advance.

2.5 The Future of Glacier Ice Dating with ArTTA

Glaciers are unique archives of climate signals and have recorded information of past times on a quasi-continuous basis, both in high-altitude regions (Haeberli and

Alean, 1985) and at summits of lower altitudes (Haeberli et al., 2004). The valuable information is stored in a very limited amount of space thus leading to hard restrictions on sample size. It is conceptually different from other research fields as groundwater studies (Ritterbusch et al., 2014) and oceanography (Ebser et al., 2018) that have been addressed by ArTTA so far, where quasi-unlimited sampling from the reservoir of interest is possible but limited by logistical and economical demands. In the case of alpine glaciers, the necessary and requested spatial resolution limits samples down to a few kilograms of ice which is a thousandfold reduction of required sample size for low-level counting (Collon, Kutschera, and Lu, 2004).

The European Alps are of special interest for ArTTA as they feature suitable age ranges, excellent logistics for sampling and allow for multi-proxy reconstruction of the Holocene climate based on instrumental and historical climate records (Dobrovolný et al., 2010). The full potential of ^{39}Ar dating manifests for the last millennium, where no other tracer is reliable. Remnants of the Little Ice Age fall into this range and the interpretation of ice layers and glacier dynamics helps to understand the highly complex climate patterns of this period (Feng et al., 2018).

In order to address the imposed questions and to cover requirements of analysis on a more frequent basis, current developments aims for higher sample throughput. The setup of a second apparatus is the result of this high demand on radio-argon dating with small samples.

Furthermore, the retreat of glaciers since 1850 (Meyer et al., 2014) endangers this exclusive climate archive and a visual example of a vanishing glacier over time is shown in Figure 2.7. The glacier surfaces of the sampling sites of this pilot study are already covered by sheets to minimize ice melt. In that sense the breakthrough of radio-argon ice dating with ArTTA has been achieved just in time to study especially those sites in danger before the stored climate records are lost forever.

FIGURE 2.7: Photographs of Great Aletsch Glacier, Switzerland from 1979, 1991 and 2002 (CC BY-SA 3.0, 2018).

Part II

Extending Sample Analysis Capacities by a new Facility

Chapter 3

Atomic Physics Fundamentals

3.1 Interaction of Atoms with External Fields

The principles of laser cooling and trapping are based on the interaction of atoms with an external field thus providing methods to manipulate and control the atomic behavior. The description in this section follows a semi-classical approach, where the atom is treated quantum-mechanically and the fields are described classically. A brief summary is presented here and more details can be found in the standard literature on this topic (Cohen-Tannoudji, Diu, and Laloë, 1977; Bransden and Joachain, 1983; Metcalf and Straten, 1999).

A simplified description for the atom is sufficient in this context, it is considered as a two-level system with ground state $|g\rangle$ and excited state $|e\rangle$. The field free Hamiltonian $\hat{H}_0$ operating on these states yields

$$\hat{H}_0|g\rangle = \hbar\omega_g|g\rangle \text{ and } \hat{H}_0|e\rangle = \hbar\omega_e|e\rangle \tag{3.1}$$

with eigenenergies $E_g = \hbar\omega_g$ for the ground state and $E_e = \hbar\omega_e$ for the excited state.

By choosing the ground state energy as zero and using $\omega_0 = \omega_e - \omega_g$. the general state of this system is then

$$|\psi(t)\rangle = c_g(t)|g\rangle + c_e(t)e^{-i\omega_o t}|e\rangle \tag{3.2}$$

with complex time-dependent coefficients $c_g(t)$ and $c_e(t)$ respectively. Following Born's rule (Born, 1926), the probability of the system to be in one of the states, e.g. the excited state, is $p(t) = |\langle e|\psi(t)\rangle|^2 = |c_e(t)|^2$.

External electric and magnetic fields can be described by adding their respective terms to a total Hamiltonian $\hat{H} = \hat{H}_0 + \hat{H}_{\text{el}}(t) + \hat{H}_{\text{mag}}(\vec{r})$. In the scope of this work, the time-dependent electric field is provided by the electric dipole of the light and only static, space-dependent magnetic fields are considered. The time evolution of

the system is given by the time-dependent Schrödinger equation

$$i\hbar\frac{\partial}{\partial t}|\psi(t)\rangle = \hat{H}|\psi(t)\rangle \tag{3.3}$$

and describes the dynamics in the system[1].

3.1.1 Atoms in Electric Fields

The general state of a two level system in equation 3.2 can be used in the time-dependent Schrödinger equation 3.3. The electric dipole Hamiltonian $\hat{H}_{\text{el}}$ has only off-diagonal elements and multiplication from the left side by $\langle g|$ and $\langle e|$ yield coupled differential equations

$$i\hbar\frac{\partial}{\partial t}c_g(t) = c_e(t)\langle g|\hat{H}_{\text{el}}|e\rangle e^{-i\omega_o t} \tag{3.4}$$

$$i\hbar\frac{\partial}{\partial t}c_e(t) = c_g(t)\langle e|\hat{H}_{\text{el}}|g\rangle e^{i\omega_o t} \tag{3.5}$$

for the time-dependent coefficients $c_g(t)$ and $c_e(t)$ respectively. The Hamiltonian for the electric field can be written as

$$\hat{H}_{\text{el}} = -\hat{d}\vec{E} \tag{3.6}$$

by replacing the vector in the classical dipole by their corresponding quantum mechanical operators.

The typical optical wavelengths used for laser cooling and trapping are several orders of magnitude larger than the electronic cloud of the atoms thus the so called electric dipole approximation neglects spatial variations of the field over the extend of an atom. A plane wave with amplitude E_0, light frequency ω_l, wave vector k and the Rabi frequency (Metcalf and Straten, 1999)

$$\Omega = \frac{E_0}{\hbar}\cos(kz - \omega_l t)\langle e|\hat{d}|g\rangle \tag{3.7}$$

then yields

$$\hat{H}_{\text{el}} = |e\rangle\hbar\Omega\langle g| + c.c. \tag{3.8}$$

at the position z of the atom.

In general, only those states that have non-vanishing Rabi frequency, i.e. $\langle e|\hat{d}|g\rangle \neq 0$, have electric dipole transitions and can be coupled by light thus can be considered

[1] The phase evolution with ω_0 is orders of magnitude higher than the time scales considered here.

for laser cooling. The transitions that are allowed are dependent on the wave functions $|g\rangle$ and $|e\rangle$ for the states involved and lead to selection rules.

The coupled equations 3.4 and 3.5 can be decoupled by a further time derivative. A second approximation neglects fast oscillations ω_l compared to the detuning $\delta = \omega_0 - \omega_l$. With the so called rotating-wave approximation, the expression for the time-dependent coefficients yields

$$\frac{d^2}{dt^2}c_g - i\delta\frac{d}{dt}c_g + \frac{\Omega^2}{4}c_g = 0 \tag{3.9}$$

for the ground state coefficient. The probability of the ground population is given by $|c_g|^2$ and normalization of the total state leads to $|c_e|^2 = 1 - |c_g|^2$. The solution of the differential equation in 3.9 is a coherent oscillation between ground state and excited state at frequency $\sqrt{\Omega^2 + \delta^2}$, the so called Rabi oscillations.

The coherent process is not directly suited for laser cooling purposes and further treatment has to include incoherent spontaneous emissions that occur at rate γ in the excited state, i.e. $\frac{d}{dt}c_e^* c_e = -\gamma c_e^* c_e$ and $\frac{d}{dt}c_e^* c_g = -\frac{\gamma}{2}c_e^* c_g$. The commutator of the total Hamiltonian with the density matrix

$$\rho = \begin{pmatrix} \rho_{gg} & \rho_{ge} \\ \rho_{eg} & \rho_{ee} \end{pmatrix} = \begin{pmatrix} c_g^* c_g & c_g^* c_e \\ c_e^* c_g & c_e^* c_e \end{pmatrix} \tag{3.10}$$

of the two level system with $|g\rangle \rightarrow \begin{pmatrix} 1 \\ 0 \end{pmatrix}$ and $|e\rangle \rightarrow \begin{pmatrix} 0 \\ 1 \end{pmatrix}$ gives the time evolution

$$i\hbar\frac{d}{dt}\hat{\rho} = \left[\hat{H}, \hat{\rho}\right] \tag{3.11}$$

of the system described by four differential equations.

This leads to the optical Bloch equations

$$\frac{d}{dt}\rho_{ee} = -\gamma\rho_{ee} + \frac{i}{2}\left(\Omega\tilde{\rho}_{ge} - \Omega^*\tilde{\rho}_{eg}\right) \tag{3.12}$$

$$\frac{d}{dt}\tilde{\rho}_{eg} = -\left(\frac{\gamma}{2} - i\delta\right)\tilde{\rho}_{eg} + \frac{i}{2}\Omega\left(\rho_{gg} - \rho_{ee}\right) \tag{3.13}$$

with $\tilde{\rho}_{eg} = \rho_{eg}e^{-i\delta t}$. The remaining two equations are given by $\rho_{gg} = 1 - \rho_{ee}$ and $\rho_{ge} = \rho_{eg}^*$. This can be solved in the steady-state with $\frac{d}{dt}\rho_{eg} = 0$ and $\frac{d}{dt}(\rho_{ee} - \rho_{gg}) = 0$.

The scattering rate of light, i.e. photons, in this case is then

$$\gamma_{textsp} = \gamma\rho_{ee} = \frac{s_0}{1 + s_0 + \frac{4\delta^2}{\gamma^2}} \cdot \frac{\gamma}{2} \tag{3.14}$$

with saturation parameter $s_0 = \frac{2\Omega^2}{\gamma^2} \propto I$, the intensity of the light. For large s_0, i.e. high laser intensities, the scattering rate γ_{textsp} approaches $\frac{\gamma}{2}$.

Additionally, high intensities and saturation on resonance lead to power broadening of the transition, increasing the effective line width by a factor of $\sqrt{1+s_0}$ from the natural line width γ.

3.1.2 Atoms in Magnetic Fields

The magnetic fields that are considered in the scope of this work are purely static and the time and energy scales of the atomic movement through the field gradients is far larger than the scales of the electric dipole interaction with the light. Thus the contributions of the magnetic fields can be treated separately.

The coupling of the atom to the magnetic field is described by the Hamiltonian

$$\hat{H}_{\text{mag}} = -\hat{\mu}\vec{B} \tag{3.15}$$

with magnetic dipole moment $\hat{\mu}$ and classical magnetic field $\vec{B}$. The magnetic moment of an atom depends on its quantum mechanical state.

The first magnetic moment is the contribution due to the orbital angular momentum and its induced magnetic field as in the classical case. In quantum mechanics however, the orbital angular momentum operator $\hat{l}$ acts on the state $|\psi\rangle$ and its eigenvalue is derived by solving the Schrödinger equation resulting in quantized lengths $|l| = \hbar\sqrt{l(l+1)}$ for $l = 0, 1, ...$ and projection $m_l = \hbar(-|l|, ..., +|l|)$ onto one axis that is usually chosen along the magnetic field direction.

The magnetic moment in field direction is then

$$\mu_l = \frac{e}{2m} m_l = \frac{\mu_B}{\hbar} m_l \tag{3.16}$$

with electron charge e, electron mass m and Bohr magneton μ_B. In presence of magnetic fields, the degenerate energy levels split into $(2l+1)$ states.

The electron spin $\hat{s}$ contributes a second magnetic moment μ_s. The length is $|s| = \hbar\sqrt{s(s+1)}$ and the projection to one axis is $m_s = \hbar(-|s|, ..., +|s|)$. The strength of the contribution is given in units of the orbital magnetic moment by the electron spin g-factor g_s yielding

$$\mu_s = g_s \mu_B m_s. \tag{3.17}$$

The last contribution that is considered here is the nuclear spin $\hat{I}$. It is treated the same as electron spin, but using a nuclear g-factor g_I and leads to

$$\mu_I = g_I \mu_B m_I. \tag{3.18}$$

In the limit of a magnetic field as considered in the scope of this work, the several magnetic moments first couple among themselves before coupling to the external field. The largest energy scale is given by coupling $\hat{l}$ and $\hat{s}$ to a total angular momentum $\hat{j} = \hat{l} + \hat{s}$. The resulting states with $j = |l - s|, ..., |l + s|$ yield the fine structure of the atom.

The total angular momentum $\hat{j}$ then couples with the nuclear spin $\hat{I}$ to $\hat{F} = \hat{j} + \hat{I}$. The hyperfine structure consists of the states with $F = |j - I|, ..., |j + I|$ with F being a good quantum number in the limit of weak fields[2]. The total magnetic moment $\hat{\mu} = \hat{\mu}_l + \hat{\mu}_s + \hat{\mu}_I$ then couples to the magnetic field.

The energy shift of the ground and excited state due to magnetic fields is small in the case of noble gases and replaces the field free states $|g\rangle$ and $|e\rangle$ by their new eigenstates $|g(\vec{r})\rangle$ and $|e(\vec{r})\rangle$. It can be therefore considered as space dependent shift of the resulting resonance frequency by

$$\Delta E = -(m_e g_e - m_g g_g)\mu_B B = -\mu_{\text{eff}} B \tag{3.19}$$

with effective magnetic moment μ_{eff} and g-factors g_g and g_e for ground and excited state respectively. The resulting shifts in the frequency are on the order of few to several hundreds of megahertz and small compared to the terahertz electric dipole transition frequencies.

3.1.3 Force on a Two-level Atom

The force on a particle in classical mechanics is given by the negative gradient of its potential energy. The expectation value of the quantum mechanical operator has to represent the classical case (Ehrenfest, 1927) and yields

$$\langle F \rangle = -\left\langle \nabla \hat{H}_{\text{pot}} \right\rangle = -\left\langle \nabla \hat{H}_{\text{mag}} \right\rangle - \left\langle \nabla \hat{H}_{\text{el}} \right\rangle. \tag{3.20}$$

The first term is the magnetic gradient force $\langle F_{\text{mag}} \rangle = \left\langle \nabla \left(\vec{\mu} \vec{B} \right) \right\rangle$ and is not discussed further in the scope of this work since it is comparably weak [3]. The gradient of the electric field Hamiltonian can be evaluated using the Rabi frequency Ω and

[2] A more general description is given by the Breit-Rabi formula. In presence of high fields, Paschen-Back effect decouples the several angular momenta and couples them directly to the external field (Griffiths, 1995; Scheck, 2007).

[3] The magnetic force becomes important for energy scales where laser cooling is not feasible due to the recoil limit (Pritchard, 1983; Bergeman, Erez, and Metcalf, 1987).

leads to

$$-\left\langle \nabla \hat{H}_{\mathrm{el}} \right\rangle = -\nabla \left\langle \hat{H}_{\mathrm{el}} \right\rangle = -\nabla \left(\mathrm{Tr} \left(\rho \hat{H}_{\mathrm{el}} \right) \right) = \hbar \nabla \Omega \rho_{ge}^{*} + c.c. \tag{3.21}$$

employing again the electric dipole approximation and rotating wave approximation.

The resulting force depends on Ω thus the exact form of the applied light field. In case of a travelling wave that is considered here, the gradient of the Rabi frequency is $\nabla\Omega = ik\Omega$[4]. Deploying the optical Bloch equations leads to the so called scattering force

$$\left\langle F_{textsp} \right\rangle = \hbar k \left(i\Omega \rho_{ge}^{*} - i\Omega^{*} \rho_{ge} \right) = \hbar k \gamma \frac{s_0}{1 + s_0 + \frac{4\delta^2}{\gamma^2}} = \hbar k \gamma \rho_{ee}. \tag{3.22}$$

It can be seen as the recoil $p = \hbar k$ of a single photon at a scattering rate $\gamma_{textsp} = \gamma\rho_{ee}$ thus the time derivative of the momentum.

A further description of the force has to include the optical Doppler shift

$$\delta_{textDoppler} = -\vec{k} \cdot \vec{v} \tag{3.23}$$

due to the change of the laboratory frame laser frequency in the frame of the moving atoms. The resonance frequency itself is changed due to external magnetic fields and shifts the transition by

$$\delta_{\mathrm{mag}} = -\frac{\mu_{\mathrm{eff}}}{\hbar} B \tag{3.24}$$

with effective magnetic moment μ_{eff} and field strength B. The total force deployed for laser cooling and trapping in the scope of this work is then

$$\left\langle F_{textsp} \right\rangle = \hbar k \gamma \frac{s_0}{1 + s_0 + \frac{4(\delta - \vec{k}\vec{v} - \frac{\mu_{\mathrm{eff}}}{\hbar} B)^2}{\gamma^2}}. \tag{3.25}$$

3.2 Atomic Physics Properties of Argon and Krypton

3.2.1 Electron Configuration and Coupling Scheme

The noble gases argon and krypton have fully occupied electronic shells with the outermost shell consisting of s and p valence electrons as in all of the main-group elements. The ground-state configuration for the 18 electrons in argon is

[4] The rotating wave approximation has been used for this (Metcalf and Straten, 1999).

$$1s^2 2s^2 2p^6 3s^2 3p^6 \tag{3.26}$$

and for the 36 electrons in krypton is

$$1s^2 2s^2 2p^6 3s^2 3p^6 3d^{10} 4s^2 4p^6 \tag{3.27}$$

with principal quantum number n and orbital angular momentum $l = 0, ..., n-1$. The nearest levels above the ground state correspond to the excitation of an electron from 3p $\rightarrow$ 4s in argon or 4p $\rightarrow$ 5s in krypton, resulting in

$$1s^2 2s^2 2p^6 3s^2 3p^5 4s \tag{3.28}$$

for argon and

$$1s^2 2s^2 2p^6 3s^2 3p^6 3d^{10} 4s^2 4p^5 5s \tag{3.29}$$

for krypton.

The remaining five 3p electrons in argon or 4p electrons in krypton have strong spin-spin and orbit-orbit interactions, leading to the LS-coupling of total spin $\hat{S}_{\text{body}} = \sum_i \hat{s_i}$ and the total angular momentum $\hat{L}_{\text{body}} = \sum_i \hat{l_i}$ to

$$\hat{J}_{\text{body}} = \hat{L}_{\text{body}} + \hat{S}_{\text{body}}. \tag{3.30}$$

The configuration can be derived using Hund's rule and gives

$$|\hat{S_z}, \hat{L_z}\rangle = |\uparrow, 1\rangle|\uparrow, 0\rangle|\uparrow, -1\rangle|\downarrow, 1\rangle|\downarrow, 0\rangle \tag{3.31}$$

which uses the rule of maximum multiplicity so that the m_s are as parallel as possible without violation of the Pauli exclusion principle. The m_l are then chosen to maximize $\hat{L}_{\text{body}}$ and yield

$$\hat{S}_{\text{body}} = \frac{1}{2} \tag{3.32}$$

and

$$\hat{L}_{\text{body}} = 1 \tag{3.33}$$

for the remaining body of five 3p or 4p electrons. The other fully occupied shells have vanishing orbital and spin angular momentum and are therefore not contributing to this.

The excited electron can be described by Racah-coupling due to the strong shielding of the core electrons and the resulting weak bonding of the excited 4s electron in

argon or 5s electron in krypton leads to large distances from the core. The orbital and spin angular momenta then couple separately to the body. The angular momentum $\hat{L}$ of the excited electron and the total angular momentum $\hat{J}_{\text{body}}$ of the body couples to

$$\hat{K} = \hat{J}_{\text{body}} + \hat{L}. \tag{3.34}$$

The spin $\hat{S}$ of the excited electron couples to a total angular momentum

$$\hat{J} = \hat{K} + \hat{S}. \tag{3.35}$$

Further excitation of the 4s or 5s electron in argon and krypton is possible by near infrared laser light. The used closed transition for laser cooling at 812 nm is $1s_5 \rightarrow 2p_9$ in Paschen-Notation and has the quantum numbers

$$n = 4, L = 0, S = \frac{1}{2}, S_{\text{body}} = \frac{1}{2}, L_{\text{body}} = 1, J_{\text{body}} = \frac{3}{2}, K = \frac{3}{2} \text{ and } J = 2 \tag{3.36}$$

for the $1s_5$ (ground) state and

$$n = 4, L = 1, S = \frac{1}{2}, S_{\text{body}} = \frac{1}{2}, L_{\text{body}} = 1, J_{\text{body}} = \frac{3}{2}, K = \frac{5}{2} \text{ and } J = 3 \tag{3.37}$$

for the $2p_9$ (excited) state.

3.2.2 Effective Magnetic Moment

In presence of magnetic fields, a good description is given by including the excited electron to the LS-coupling. The total orbital and total spin magnetic moments of body and excited electron are $\hat{L}_{\text{tot}} = \hat{L}_{\text{body}} + \hat{L}$ and $\hat{S}_{\text{tot}} = \hat{S}_{\text{body}} + \hat{S}$. In the weak field limit, they first couple to $\hat{J} = \hat{L}_{\text{tot}} + \hat{S}_{\text{tot}}$ which then couples to the magnetic field.

The magnetic moment is

$$\vec{\mu}_J = g_J \mu_B \hat{J} = g_L \mu_L \hat{L}_{\text{tot}} + g_S \mu_S \hat{S}_{\text{tot}} = \vec{\mu}_L + \vec{\mu}_S \tag{3.38}$$

with $g_L = 1$ by definition and the electron g-factor $g_S = 2.002$.

An expression for g_J is then derived by

$$\begin{aligned} g_J \hat{J}\cdot\hat{J} &= g_L \hat{L}_{\text{tot}}\cdot\hat{J} + g_S \hat{S}_{\text{tot}}\cdot\hat{J} = g_L \hat{J}\cdot\hat{L}_{\text{tot}} + g_S \hat{J}\cdot\hat{S}_{\text{tot}} \\ &= g_L \frac{\hat{J}^2 + \hat{L}_{\text{tot}}^2 - \hat{S}_{\text{tot}}^2}{2} + g_S \frac{\hat{J}^2 + \hat{S}_{\text{tot}}^2 - \hat{L}_{\text{tot}}^2}{2} \end{aligned} \tag{3.39}$$

and leads to

$$\begin{aligned} g_J = g_L &\frac{J(J+1) + L_{\text{tot}}(L_{\text{tot}}+1) - S_{\text{tot}}(S_{\text{tot}}+1)}{2J(J+1)} \\ + g_S &\frac{J(J+1) + S_{\text{tot}}(S_{\text{tot}}+1) - L_{\text{tot}}(L_{\text{tot}}+1)}{2J(J+1)}. \end{aligned} \tag{3.40}$$

The effective magnetic moment of the $1s_5(J=2) \rightarrow 2p_9(J=3)$ transition in ^{40}Ar and ^{84}Kr is

$$\mu_{\text{eff}} = (m_e g_e - m_g g_g)\mu_B \tag{3.41}$$

with $g_g = 1.5012$ and $g_e = 1.3341$. This yields an effective magnetic moment of $\mu_{\text{eff},40} = \mu_B$ for the σ^+ transition $m_g = +2 \rightarrow m_e = +3$.

A nuclear spin $\hat{I}$ can be added by $\hat{F} = \hat{J} + \hat{I}$ in the weak field limit. The g-factor g_F is then

$$\begin{aligned} g_F = &g_J \frac{F(F+1) + J(J+1) - I(I+1)}{2F(F+1)} \\ &+ \frac{m_e}{m_p} g_I \frac{F(F+1) + I(I+1) - J(J+1)}{2F(F+1)} \end{aligned} \tag{3.42}$$

with the mass ratio of electron and proton $\frac{m_e}{m_p} = \frac{1}{1836}$, nuclear spin $I = \frac{7}{2}$ and nuclear g-factor $g_I = \frac{\mu_I}{\mu_B I} = 0.45538$ for ^{39}Ar.

The $F = \frac{11}{2} \rightarrow F = \frac{13}{2}$ transition in ^{39}Ar has the same effective magnetic moment $\mu_{\text{eff},39} = \mu_B$ as for the even isotopes. Concerning the design of the magnetic fields, this is convenient for switching between the different isotopic species.

3.2.3 Multi-level Structure of Noble Gases

The discussion of laser cooling and trapping so far has focused on a simplified case of a two-level system but most atomic systems such as noble gases have a complex level structure. A common approach to use the derived formalism is to consider an

effective two-level system that can be approximated under certain conditions.

In the case of noble gases, the many levels due to principal quantum number and fine structure have energy differences far beyond the addressable range of the narrow-band laser light and are therefore of secondary importance for laser cooling and trapping. They nevertheless play a crucial role in the first excitation to a desired long-lived state (Phelps and Molnar, 1953) or for more advanced optical pumping processes (Young, Yang, and Dunford, 2002; Hickman, Franson, and Pittman, 2016). Figure 3.1 shows the lowest four s-states and the lowest ten p-states above the ground state of ^{40}Ar. The selection rule $\Delta J = \pm 1, 0$, but $0 \rightarrow 0$ is forbidden, excludes certain transitions and yields a convenient metastable state $1s_5$ with $J = 2$ where a closed transition to $2p_9$ with $J = 3$ exists. This transition at 812 nm is used as the cycle for cooling and trapping.

The hyperfine splitting of odd number noble gas isotopes has to be considered and Figure 3.2 shows the levels for the cooling transition of ^{39}Ar. The energy shifts are in reachable ranges of the laser light and this leads to occasional excitation into the wrong state. This loss channel is small but because millions of photons are scattered, it has to be closed by additional repumper frequencies. Since the branching ratios for the used transition in noble gases are in the order of 10^{-3}, the splitting in case of noble gases is negligible for the effective two-level system.

The effect of a magnetic field on the projected total angular momentum quantum number m_J or m_F leads to a lift of the degeneracy and additional levels in the otherwise effective two-level system. This is the Zeeman splitting and the energy shifts are shown in Figure 3.3 for the cooling transition of ^{39}Ar. The different effective magnetic moments μ_{eff} for ground and excited state lead to a shift of the resonance frequency of those states. An effective two-level system can be obtained by using circular light with σ^+ or σ^- polarization. The excitation in this case has to fulfill $\Delta m_{J,F} = \pm 1$ and a closed circle is given for the stretched states $m_J = 2 \rightarrow m_J = 3$ and $m_F = \frac{11}{2} \rightarrow m_F = \frac{13}{2}$ for ^{40}Ar and ^{39}Ar respectively.

3.3 Devices and Techniques in Atomic Physics

The devices to produce and control the narrow-band light required for laser cooling and trapping are the building blocks of Argon Trap Trace Analysis. This section provides a brief description of the employed techniques.

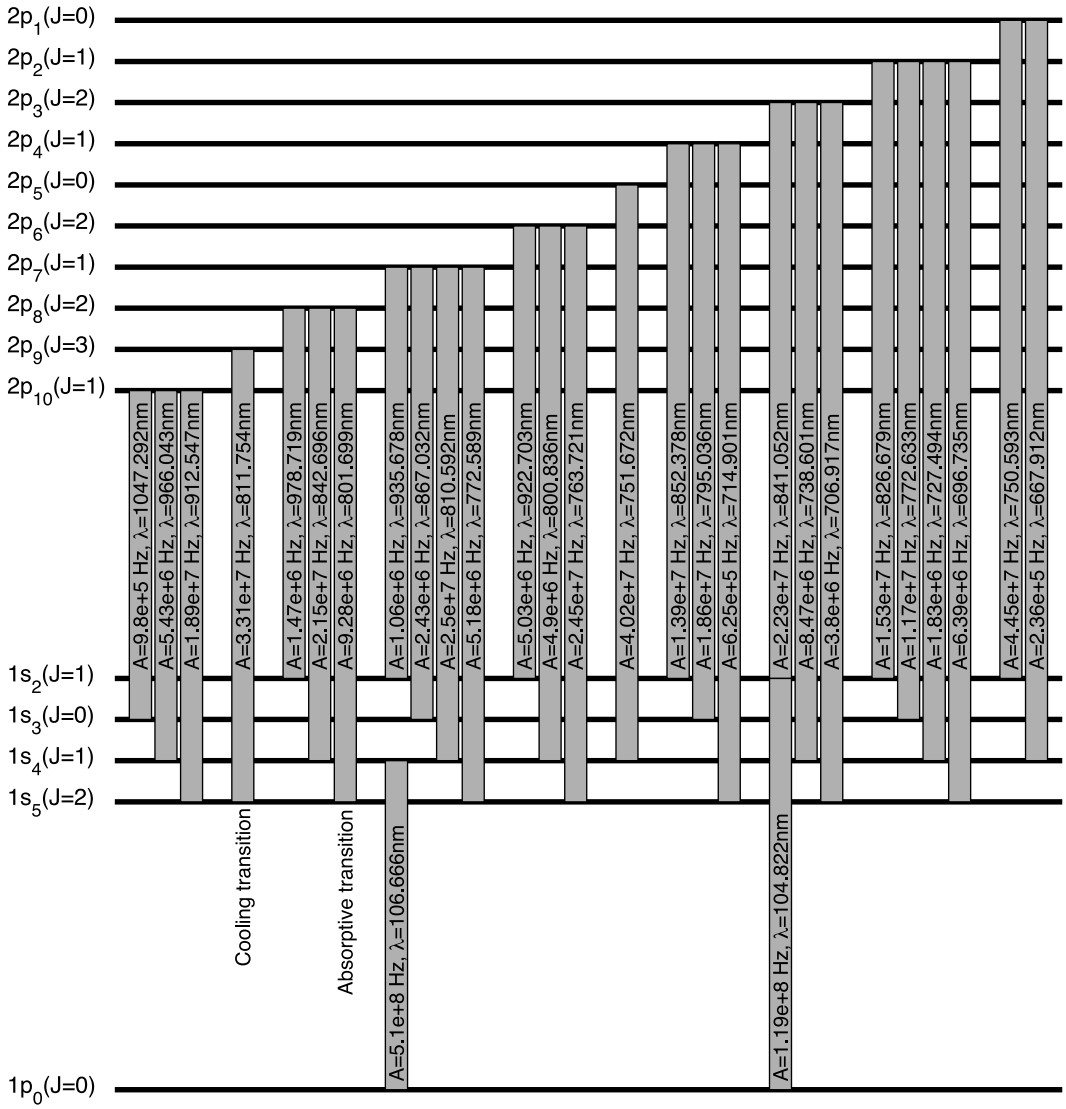

FIGURE 3.1: Fine structure of ^{40}Ar. The ground state, the four lowest s-states and the ten lowest p-states of the excited electron are shown and labelled in Paschen notation. The possible transitions due to the selection rules $\Delta J = \pm 1, 0$ are shown and yield a metastable state $1s_5$. This is chosen as the quasi ground state of the laser cooling cycle. The transition to $1p_9$ is closed since the selection rule forbids any dipole transitions except back to the metastable $1s_5$ state. Taken from Welte, 2011.

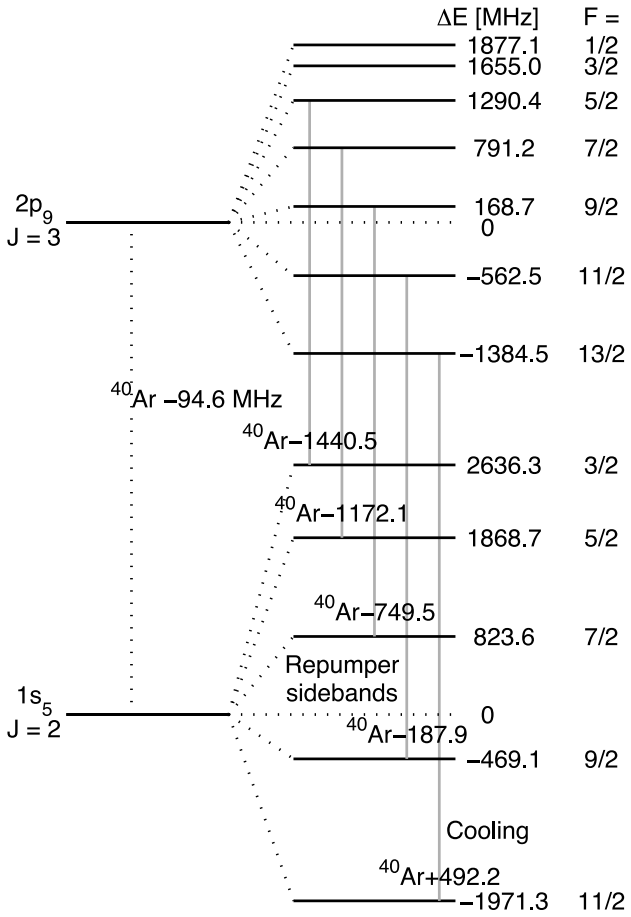

FIGURE 3.2: Hyperfine structure for ^{39}Ar. The hyperfine splitting of the cooling transition $1s_5 \rightarrow 2p_9$ is shown with the respective energy shifts. An approximation of an effective two level system is the transition from $F = \frac{11}{2} \rightarrow F = \frac{13}{2}$ where the loss channels have been closed by additional repumper frequencies. Taken from Welte, 2011.

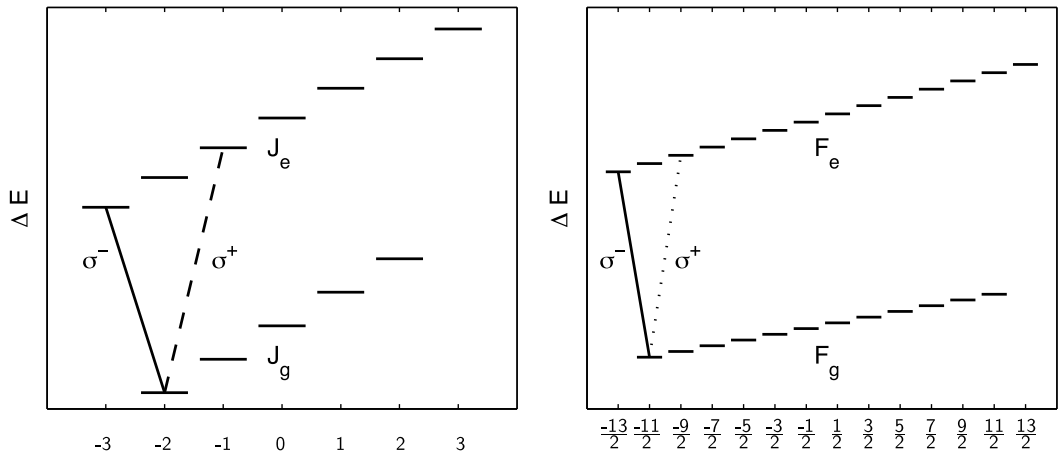

FIGURE 3.3: Zeeman splitting for ^{40}Ar and ^{39}Ar. In presence of external magnetic fields, the m_J or m_F sublevels are shifted according to their effective magnetic moment μ_{eff}. This changes the resonance frequency since the g-factors for ground and excited states are different. Circular light with σ^+ or σ^- polarization has to fulfill the selection rule $\Delta m_{J,F} = \pm 1$ and is used to restore the two-level system by using the outermost states as a closed transition. Taken from Welte, 2011.

3.3.1 Doppler-free Saturation Spectroscopy

The narrow-band laser light that is generated by external-cavity diode lasers has to be tuned to an exact reference frequency before further processing. A common method is to lock the laser to an atomic transition and in the case of noble gases, it is usually the chosen cooling transition of an abundant isotope in a plasma spectroscopy cell. A hindrance is the thermal velocity that is several orders of magnitude higher than the natural line width thus suppressing the latter.

To extract the natural transition line width a Doppler-free saturation spectroscopy setup (Hänsch, Schawlow, and Series, 1979) is deployed as shown in Figure 3.4. The incoming light is horizontally polarized and passes a polarizing beam splitter. It is scanned over the resonance and is absorbed by the metastable noble gas in a plasma spectroscopy cell. The retro-reflected light is vertically polarized as it has passed a quarter-wave plate twice and gets absorbed again. Light that is detuned from atomic resonance will address different velocity classes but resonant light will address the same atoms on both passes. If the optical intensity is chosen close to saturation for the first beam, the second will show reduced absorption and yields the natural line width as the so-called Lamb dip.

The signal can be detected on a photodiode using a lock-in amplifier as phase sensitive detector (Bjorklund, 1980). For this, the laser current is modulated at a frequency ω_{mod} in the range of kHz, the laser frequency is then

$$\omega = \omega_l + A \sin(\omega_{\text{mod}} t) \tag{3.43}$$

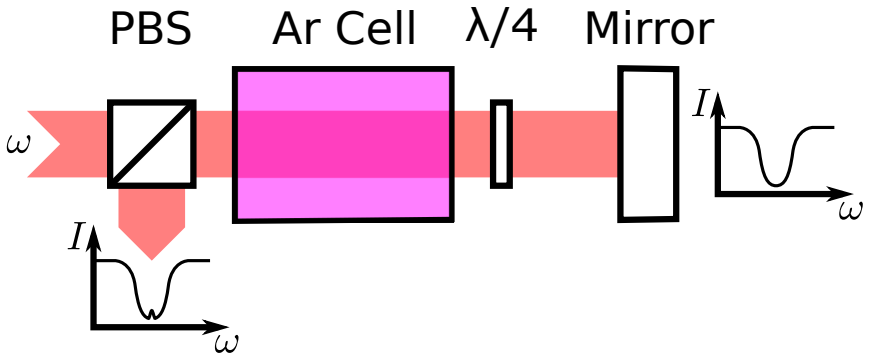

FIGURE 3.4: Schematic view of the Doppler-Free saturation spectroscopy. The laser light is scanned over the resonance, but the movement of the atoms yields Doppler broadening several orders of magnitude larger than the natural line width. The retro-reflected light addresses atoms of different velocity classes for all detunings except the atomic resonance. The transition is saturated by the reflected light and the natural line width is then visible as Lamp dip.

with modulation depth A small compared to ω_l. The intensity of the spectroscopy light follows the Beer-Lambert's law[5] and yields

$$I(\omega) = I_0 e^{-\alpha(\omega)} = I_o e^{-\alpha(\omega_l + A\sin(\omega_{\text{mod}} t))} \tag{3.44}$$

with the frequency dependent absorption coefficient $\alpha(\omega)$ holding the spectroscopic information, i.e. the Doppler broadening and the Lamb dip. The Taylor expansion around ω_l leads to

$$\begin{aligned} I(\omega) &= I(\omega_l) + A\sin(\omega_{\text{mod}} t)\left.\frac{\mathrm{d}I(\omega)}{\mathrm{d}\omega}\right|_{\omega=\omega_l} \\ &= I(\omega_l)\left(1 - A\sin(\omega_{\text{mod}} t)\right)\left.\frac{\mathrm{d}\alpha(\omega)}{\mathrm{d}\omega}\right|_{\omega=\omega_l}. \end{aligned} \tag{3.45}$$

A phase sensitive detector as the lock-in amplifier suppresses all but signals at ω_{mod} and yields an output proportional to $\frac{\mathrm{d}\alpha(\omega)}{\mathrm{d}\omega}$. The final signal is thus proportional to the derivative of the spectroscopy signal.

The resulting zero-crossing of the Lamb dip can be used as an error signal for a PID-loop to lock the laser exactly onto the atomic transition.

[5] This holds only in the case of non-saturated absorption. For simplicity, the absorption length L has been included into the absorption coefficient $\alpha(\omega)$.

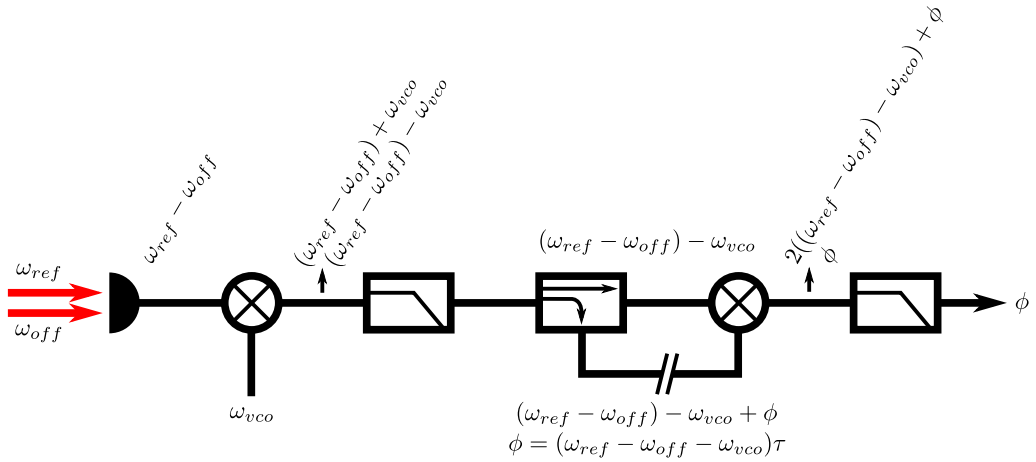

FIGURE 3.5: Schematic of the electric circuit for offset locking. The difference of the reference frequency ω_{ref} and the offset frequency ω_{off} yields a beating of the intensity. This is typically at several hundred MHz and is mixed subsequently by the signal of a voltage controlled oscillator with frequency ω_{vco}, yielding the sum and difference of both frequencies, where the former is suppressed by a low pass filter. The resulting frequency $\omega_{\text{ref}} - \omega_{\text{off}} - \omega_{\text{vco}}$ of few MHz is split to add a phase shift of $\phi = (\omega_{\text{ref}} - \omega_{\text{off}} - \omega_{\text{vco}})\tau$ to one path with propagation time τ. Recombining yields the sum and difference of both signals where the former is again suppressed by a low pass filter. The final signal is a DC signal proportional to the beating on the photodiode that can be used to lock the second laser to the reference laser.

3.3.2 Offset-Locking to a Reference

Once a reference laser is locked to a known frequency, i.e. an atomic transition, other lasers can be locked to the light with offsets up to GHz. An electronic circuit to process the signals is described in Schünemann et al., 1999.

Figure 3.5 shows the scheme of the deployed setup. The reference laser with the frequency ω_{ref} and the second laser with the frequency ω_{off} are overlapped on a photodiode. The detected intensity is modulated at the beating frequency of

$$\omega_{\text{beat}} = \omega_{\text{ref}} - \omega_{\text{off}}. \tag{3.46}$$

This is between a few MHz up to GHz and is mixed with the output of a voltage controlled oscillator at ω_{vco}. The oscillating signal is

$$I \propto \sin(\omega_{\text{beat}} t)\sin(\omega_{\text{vco}}) = \frac{1}{2}\left(\cos((\omega_{\text{beat}} - \omega_{\text{vco}})t) - \cos((\omega_{\text{beat}} + \omega_{\text{vco}})t)\right) \tag{3.47}$$

and includes the difference and sum frequencies of the input signals.

They are separated by a low pass filter and the latter at the frequency $\omega_{\text{beat}} - \omega_{\text{vco}}$ is split into two paths by a directional coupler. One path is delayed and yields a

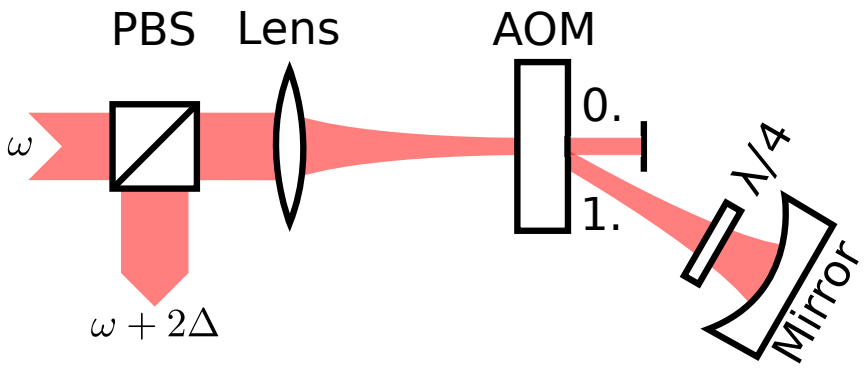

FIGURE 3.6: Schematic of a double-pass acousto-optical modulator setup. The incoming light at the frequency ω is diffracted into the first order by an acousto-optical modulator at the frequency Δ. This detuning is added to the light frequency twice by retro-reflection so that the outcoming light is at $\omega + 2\Delta$. The small aperture of the acousto-optical modulator requires focusing by a lens and retro-reflection by a curved mirror obtains the laser beam profile.

phase shift

$$\phi = (\omega_{\text{beat}} - \omega_{\text{vco}})\tau \tag{3.48}$$

where τ is the propagation time through the delay line.

Subsequent mixing yields the sum and difference frequency of both paths and a low pass filter is used to suppress the sum. The final signal is free of fast oscillations $\omega_{\text{beat}} - \omega_{\text{vco}}$ and is instead a DC signal proportional to $\sin(\phi)$. The phase itself is proportional to the beating of the two laser frequencies. The DC signal shows any changes of ω_{beat} and thus can be used in a PID-loop to lock the second laser to the reference laser.

The offset lock provides a convenient method to change the isotopic species as the laser can be set to the different cooling transitions. The further detunings to compensate Doppler shifts at the different atomic optical devices can be added relative to the cooling transition by acousto-optical modulators.

3.3.3 Frequency Shifting

The light provided by the laser has to be processed further for several atomic optical devices to compensate mainly for Doppler-shifts and add optical repumper light at the exact transition frequencies. A common method is to use an acousto-optical modulator in double-pass configuration.

Figure 3.6 shows the schematic of the deployed setup. The light has to be focused into the small aperture region. The distance from the lens and the acousto-optical

modulator is chosen as the focal length so that plane wavefronts enter the modulator. The modulator is driven by an acoustic wave at frequency Δ that will diffract the light due to density modulations inside the crystal. The first order diffraction has the detuning Δ added to its optical frequency and retro-reflection adds another detuning Δ which leads to a frequency $\omega + 2\Delta$ that leaves the setup.

A spherical mirror is used to reflect the beam, so that the beam shape of the outcoming light remains unchanged. The incoming polarization is aligned horizontally and passes the polarization beam splitter whereas the retro-reflected light has passed a quarter wave plate twice yielding vertical polarization that is reflected by the same beam splitter.

Chapter 4

A New Apparatus in a Self-sufficient Laboratory Container

The unique dating range of ^{39}Ar has been acknowledged and praised for decades (Loosli, 1983) but the possibility of a broad application has been demonstrated only through recent successful environmental studies with Argon Trap Trace Analysis (Ritterbusch et al., 2014; Ebser et al., 2018). These experiments have reignited a huge demand on radio-argon dating with samples as small as 0.5 mL STP argon corresponding to liter-sized water samples or ice blocks of a few kilograms. More capacity, i.e. another apparatus, is required to meet the resulting need for higher sample throughput while enabling a further development of the method. The new setup in a self-sufficient laboratory container that has been built in the scope of this work is described in this chapter.

4.1 Overview of the ArTTA Modules

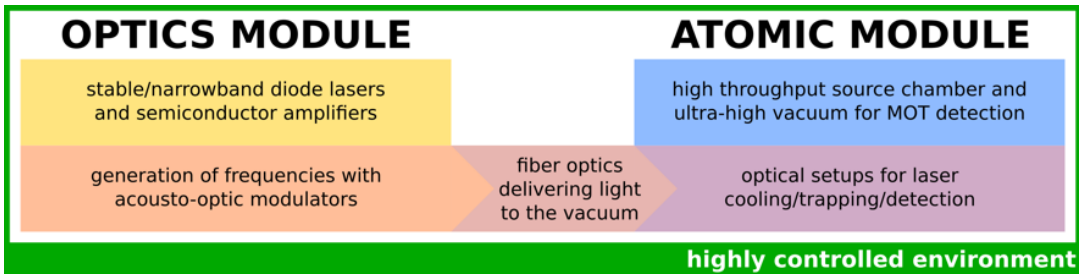

FIGURE 4.1: The modules of ArTTA. The optics module consists of a laser setup and the frequency shifting. The produced optical light is delivered by fibers to the atomic module. This module consists of atom optical components and a vacuum setup. The apparatus is in a highly-controlled environment to minimize influences from outside.

Figure 4.1 shows an abstract view of the project by dividing necessary components into several modules and sub-modules. The following sections describe the

planning and setup of these individual modules. The functionality and interaction of all modules together is demonstrated in the last section by the first magneto-optical traps of argon (^{40}Ar) and krypton (^{84}Kr) in the new laboratory container.

4.2 Highly Controlled Environment

The experiences gathered over years by the prototype apparatus show that minimizing the disturbances in the laboratory is a key prerequisite for a successful operation and thus reliable radio-argon dating. The existing laboratory is actively temperature stabilized (Ebser, 2018) and dehumidified, aiming to keep the same conditions over months of operation. A self-contained laboratory has been designed to continue and further improve this approach by adding 15 cm of insulation and 5 cm of sound-proofing material to the outer wall.

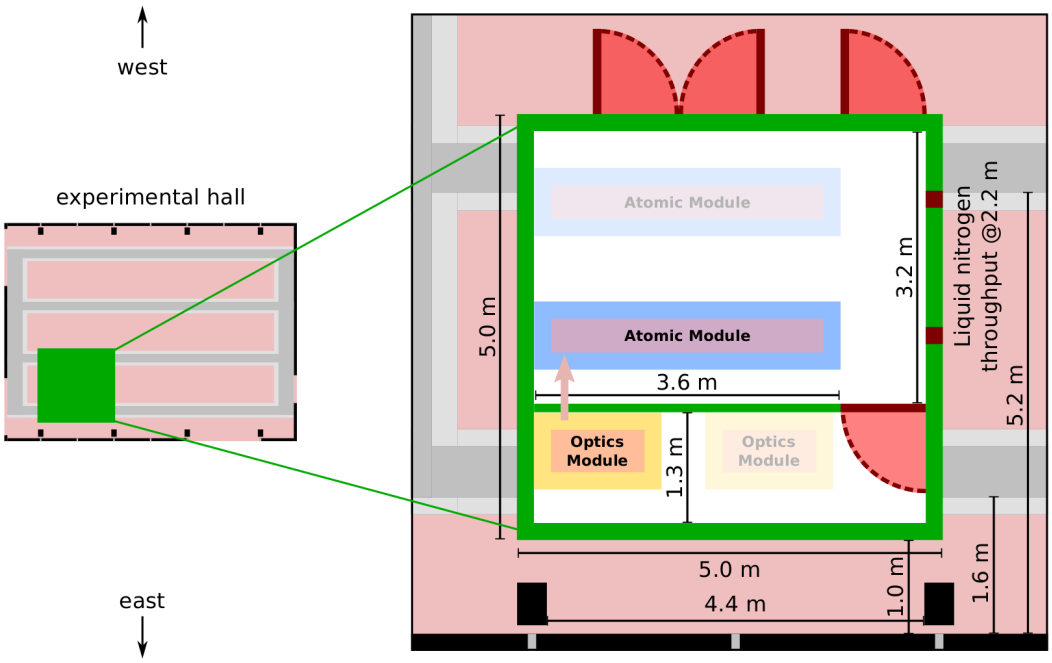

FIGURE 4.2: Ground plan of the laboratory container. The location inside the experimental hall has been chosen such as to minimize the exposure by the sun through the east and west window fronts. Electrical power, cooling water and compressed air are provided through cable ducts in the hall and openings in the floor of the container. Liquid nitrogen can be stored outside and fed through the wall. The more sensitive laser system is in an extra room with additional air conditioning to reduce disturbances by routine maintenance in the future.

The location inside the experimental hall next to the Kirchhoff-Institute for Physics is shown in Figure 4.2. The position of the container has been chosen to minimize the sun exposure through the west and east window fronts, the latter is mostly covered by surrounding buildings. The experimental hall supplies access to electric power, cooling water, and compressed air through cable ducts below ground and openings in the container floor. Up to 55 kW of electrical power can be provided. Liquid nitrogen is stored outside and inserted by pumping it to feedthroughs that are placed at height of 2.2 m.

The laboratory container is divided into two air conditioned rooms. The first room provides enough space for two apparatuses consisting of a vacuum chamber, several turbo-molecular pumps and the necessary atom optical devices. A double-leaf door has been used for the installation of the larger objects while a smaller door provides access once the apparatus is running. The air and evaporated nitrogen is extracted through a pipe that is connected to the ventilation system of the experimental hall. The second room is designed for the laser setup and is separated so that routine operations such as sample change can be performed without an unnecessary disturbance of the more sensible parts. Optical glass fibers are used to transport the cooling and trapping light from the laser room to the atom optical devices.

The container was manufactured by Algeco and it was split into two containers for their delivery on trucks. A construction team and our mechanical workshop installed the container in December 2016 using the crane of the experimental hall.

Figure 4.3 shows the delivery and installation of the container. The two parts were assembled by connecting the electrical wires and by a proper insulation of the separation surface. An anti-static floor was laid and openings over the cable ducts were cut out. The final inspection and approval were done after the two days of setup and Figure 4.4 shows the finished interior of the laboratory container.

4.3 Optics Module

A very reliable optical system is necessary for the successful operation of ArTTA, where a single measurement runs for at least a day. A high level of long-term stability is required for environmental studies since they typically consist of several samples that are measured in a time span of weeks or even months.

The cooling and trapping of argon isotopes in ArTTA uses the cycling transition $1s_5 \rightarrow 2p_9$ yielding four frequencies for the even isotopes, i.e. ^{40}Ar and ^{38}Ar. The detunings in the following are given relative to the resonance of the desired isotope. The two near-resonant transverse laser cooling stages are a collimator with

FIGURE 4.3: Photos of the delivery and setup of the laboratory container. The manufacturer Algeco delivered the two parts of the container on trucks. The crane inside the experimental hall, operated by our mechanical workshop, moved the pieces to the designated location. A construction team from the company assembled both parts mechanically, connected the electrical wires and laid the floor with the cut-outs over the cable ducts. After two days, the container was ready for a final product inspection and approval.

tilted mirrors and a two-dimensional magneto-optical trap. The former is provided with -4.2 MHz and the latter with -8.2 MHz, the same frequency as the three-dimensional magneto-optical trap. Longitudinal cooling is also done in two steps. A Zeeman slower uses far off-resonant light at -748.2 MHz to decelerate the atoms

FIGURE 4.4: Photos of the finished interior of the laboratory container. Each of the two rooms has a separate air conditioning and a door prevents air circulation from the main room to the more sensitive laser components. An anti-static floor was laid and baseboards were applied. The walls consist of a 15 cm thick insulation layer and a 5 cm soundproofing layer. Additionally, a hole pattern was applied to the otherwise plain inner walls. The soundproofing reduces the noise by other works in the experimental hall to an inaudible level.

with initial thermal velocity down to tens of meters per second. A second longitudinal cooling stage, called Booster, uses light at -28.2 MHz to slow them further below the capture velocity of the magneto-optical trap. The Doppler shift is compensated by magnetic fields, a dedicated coil with increasing field in the case of the Zeeman slower and the quadrupole field of the magneto-optical trap in the case of the Booster.

The hyper-fine splitting of ^{39}Ar due to the nuclear spin $I = \frac{7}{2}$ requires up to four additional frequencies to close the transition by optical pumping. These repumper frequencies are at -187.9 MHz, -749.5 MHz, -1172.1 MHz and -1440.5 MHz from the ^{40}Ar resonance (Welte, 2011; Welte et al., 2009).

All required frequencies are sketched in 4.5. The master laser is directly locked to the $1s_5 \rightarrow 2p_9$ transition of ^{40}Ar by a Doppler-free saturation spectroscopy. A part of

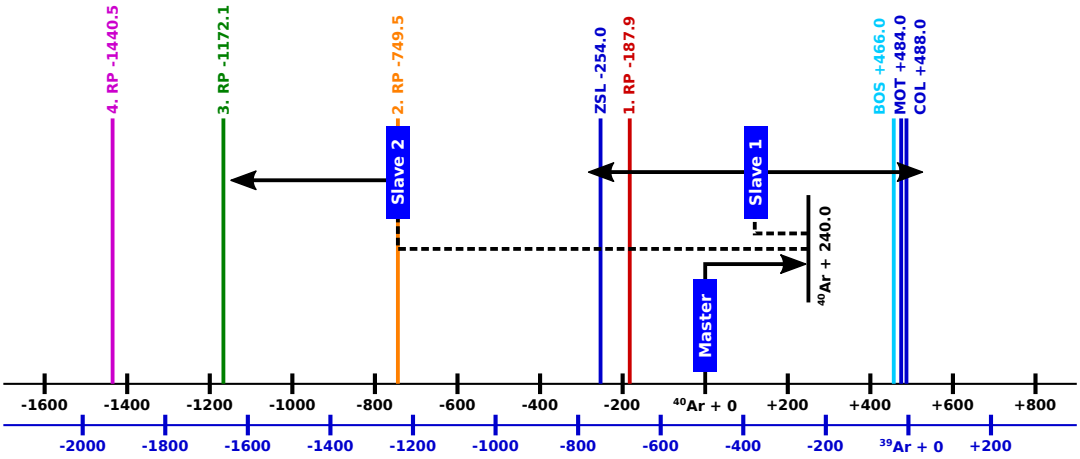

FIGURE 4.5: Required frequencies for the trapping of metastable argon. All numbers are given as MHz detuning from the ^{40}Ar resonance. The frequencies generated by acousto-optical modulators are depicted as solid arrows and offset-locked frequencies are dashed lines. The cooling frequencies (COL, ZSL, BOS, MOT) are used for all argon isotopes. The hyper-fine splitting of ^{39}Ar demands for up to four additional optical pumping frequencies to close the cooling transition properly. The master laser is directly locked to the $1s_5 \rightarrow 2p_9$ transition of ^{40}Ar and two slave lasers are offset-locked to the master. The exact frequencies are generated by acousto-optical modulators.

TABLE 4.1: Offset lock settings for different isotopes

isotope	offset slave 1 to ^{40}Ar	offset slave 2 to ^{40}Ar
^{40}Ar	−375.2 MHz	not required
^{39}Ar	117 MHz	−749.5 MHz
^{38}Ar	−583.2 MHz	not required

the light is used to generate the first repumper and the rest is shifted to +240.0 MHz for convenient offset-locking (Schünemann et al., 1999). The first slave laser is dedicated to generating the cooling and trapping frequencies and is offset-locked to the isotope of interest with specific frequency settings as shown in Table 4.1.

The second slave laser can be offset locked directly to the frequency of the second or third repumper. For this setup, it has been chosen to lock it to the second repumper since not all repumpers are necessary and the second is used more often in atom optical devices than the third.

A schematic view of the laser setup and the frequency shifting is shown in Figure 4.6. The basis consists of four external-cavity diode lasers (Toptica DL Pro) providing narrow-band light with a line width in the order of few hundred kHz (Ricci et al., 1995). The master laser is locked to the $1s_5 \rightarrow 2p_9$ cycling transition of ^{40}Ar and the quench is locked to the $1s_5 \rightarrow 2p_8$ depumping transition. Two slave lasers are

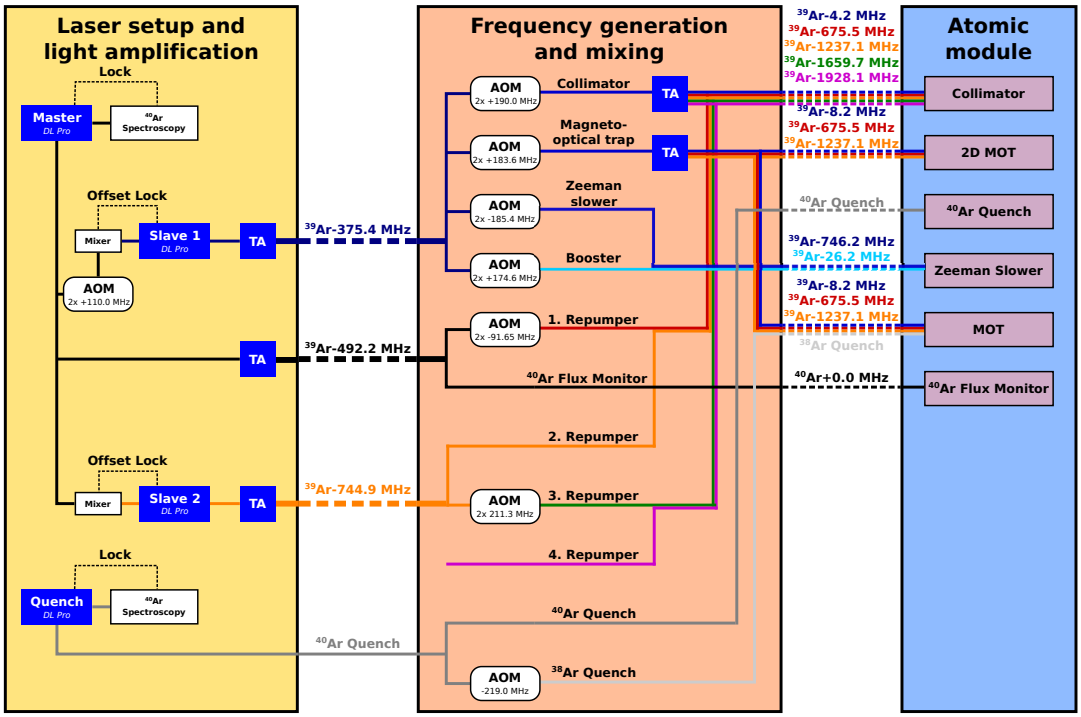

FIGURE 4.6: Scheme of the frequency shifting. Four external-cavity diode lasers (Toptica DL Pro) are used to generate the basic light. The master is directly locked to the $1s_5 \rightarrow 2p_9$ transition of ^{40}Ar by a Doppler-free saturation spectroscopy and is then divided to three paths. The first repumper is directly generated by an acousto-optical modulator. Two slave lasers are offset-locked to the master and generate the necessary cooling and the remaining repumper frequencies for ^{39}Ar. Tapered amplifiers are used to provide sufficient laser power. The exact frequencies for the atom optical devices are shifted with acousto-optical modulators and are mixed afterwards. The light is coupled into optical fibers and delivered to the components. An additional diode laser is locked to the $1s_5 \rightarrow 2p_8$ transition and optically pumps the undesired ^{40}Ar to the ground state.

offset-locked to the master light and provide further frequencies. The required optical power is achieved through the use of tapered amplifiers. The exact frequencies necessary for the atom optical devices are fine-tuned with several acousto-optical modulators. The cooling frequencies are mixed with the required repumper frequencies and are coupled into optical fibers so that the light is delivered to the atom optical components.

The components of the optics module are built on a specifically designed two-layer optical table. This setup minimizes the required space in the small laser room of the container and is shown in Figure 4.7. The top layer contains the laser setup and the light amplification while the bottom layer is for the frequency shifting and mixing into the fibers to the several atom optical devices. An intermediate layer was added to store the fiber-coupled spectroscopy cells. Cable ducts for the fibers are mounted on the wall and connect both rooms of the container.

FIGURE 4.7: Photo of the two layer optical table. The laser setup and light amplification is built on the top layer while the bottom layer houses the frequency shifting. An intermediate layer was added to store the fiber-coupled closed spectroscopy cells and optics for offset-locking.

4.3.1 Laser Setup and Light Amplification

The purpose of the laser setup and light amplification module is to generate the required light for the $1s_5 \rightarrow 2p_9$ and $1s_5 \rightarrow 2p_8$[1] optical transitions of ^{40}Ar. The transitions are analyzed in a closed fiber-coupled argon plasma cell and the master and quench are locked to them by Doppler-free saturation spectroscopy. Additional frequencies are provided by offset-locking of the two slave lasers. The light obtained this way is amplified up to several hundreds of milliwatt by tapered amplifiers. These four frequencies are the basis for the frequency and mixing module that is described in the next subsection.

The construction plan of this module is shown in Figure 4.8. The individual components are external-cavity diode lasers (Toptica DL Pro), home-built tapered amplifiers and locking devices, namely spectroscopy lock and offset lock. The components are connected by an optical pathway from where the light is divided, mixed and distributed. An acousto-optical modulator shifts the frequency by 240 MHz away from the ^{40}Ar resonance to enable proper offset locking to this isotope.

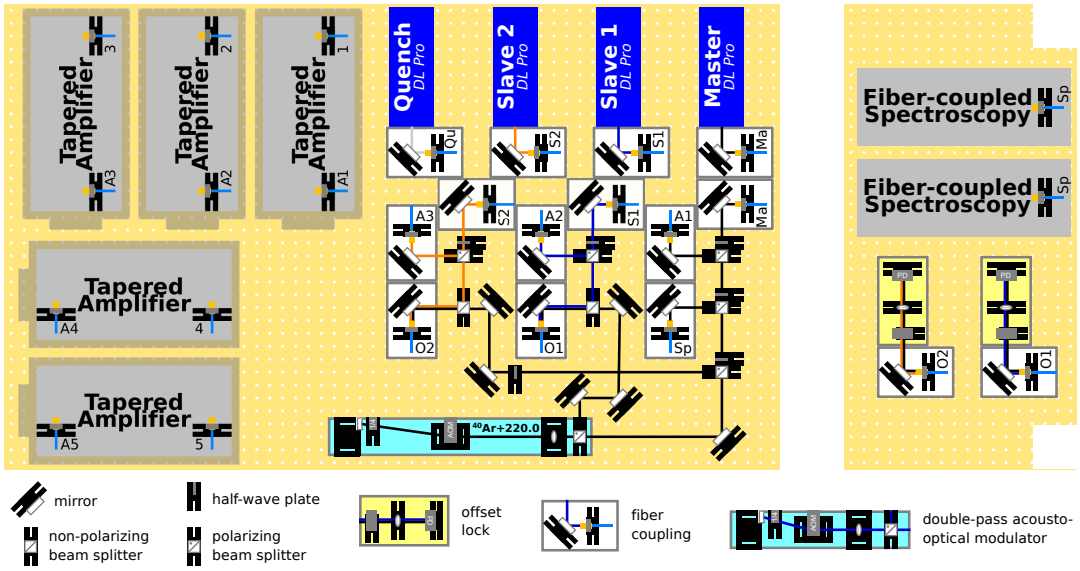

FIGURE 4.8: Construction plan for the laser setup and light amplification. The modular construction uses fibers to decouple each of the components, namely diode lasers, frequency locking and tapered amplifiers. The remaining optical devices are used to divide and mix the generated light and connect the individual components. An intermediate layer has been inserted to provide additional space and holds the locking devices.

[1] This transition is used to optically pump the abundant ^{40}Ar to the ground state.

Fiber-coupled Closed Spectroscopy

The instability and the limited lifetime of the plasma spectroscopy cell for metastable argon have been issues that have been addressed and solved in the scope of this work. The former design required a constant pumping of the cell to keep the plasma inside ignited. The hose for pumping and the set up on the optical table strongly hindered flexibility.

A closed plasma cell makes pumping obsolete but their lifetime has been limited to a few days only due to sputtering on the inside. A cleaning procedure has been tested and successfully applied in the scope of this work and makes a modular spectroscopy cell feasible.

The borosilicate glass tube has been produced by the glass blowing workshop in the Zentralbereich of the Neuenheimer Feld. It is 150 mm long with a diameter of 26 mm. A small glass pipe is attached for pumping purposes and a glass valve is used to close the cell during cleaning cycles.

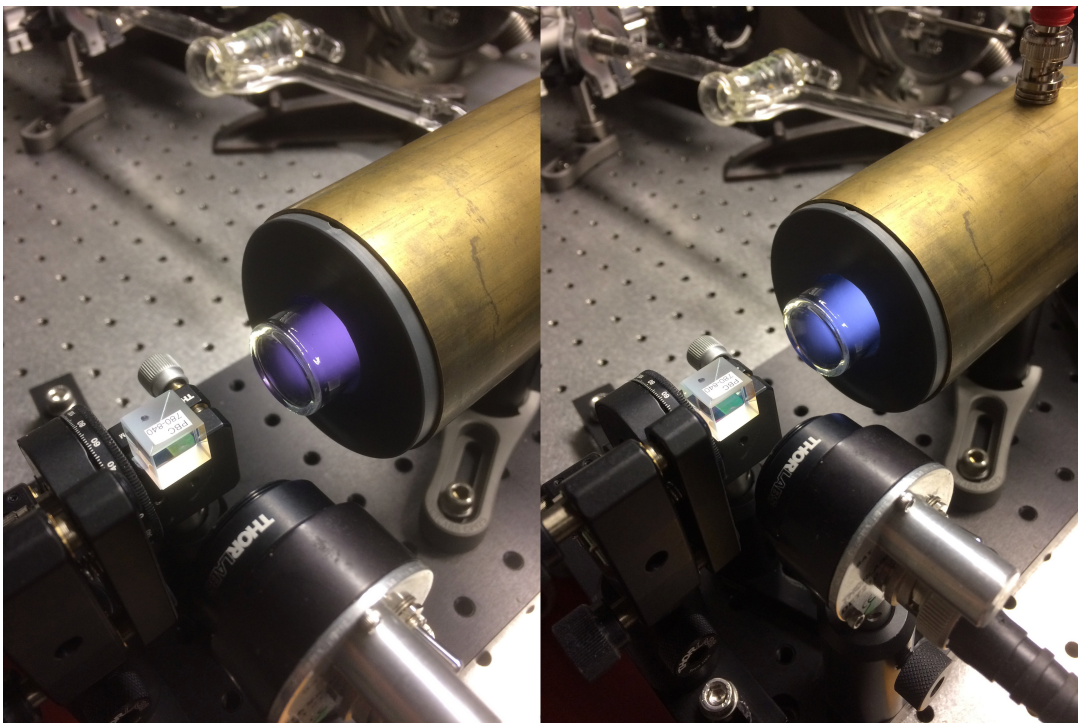

FIGURE 4.9: Preparation of the closed spectroscopy cells. The images show the plasma inside the spectroscopy cell (left) after filling with argon and (right) after $\sim$ 1 hour. For the preparation, the glass cell is evacuated by a pumping stage consisting of a turbo-molecular pump and a roughing pump. It is filled with the desired amount of argon or krypton gas, a valve is closed and the plasma is then ignited. After a certain time, the cell is evacuated and refilled. This process is repeated several times to clean the inner surface of the glass, extending the lifetime of the spectroscopy cell.

The cleaning procedure starts by filling the cell with 100 mbar of argon or krypton gas and closing the glass valve. The cell is put in the center of a helical resonator to ignite the plasma inside. After a certain time, the color of the discharge changes visibly as shown in Figure 4.9. The absorption of a spectroscopy laser becomes smaller over time, indicating that the density of metastable atoms is reduced. The gas in the cell is replaced and this cycle is repeated several times. The glass tube is melted after the last cycle to finally close the cell.

This has increased the lifetime of the cells so that the same cell has been used since the beginning of the laboratory container project. Replacement cells have been produced though and can be inserted easily if necessary at some point.

The Doppler-free saturation spectroscopy setup has been designed based on the dimensions of the plasma cell and the required space for a helical resonator as antenna. Figure 4.10 shows an image of the realized spectroscopy setup. A custom made aluminum block has been designed for this purpose and holds the required optics and electrical components such as a voltage-controlled oscillator and 1 W amplifier. The spectroscopy light is induced by an optical fiber, passes the cell twice and is detected by a photodiode. More details of the setup can be found in Gierlich, 2017.

Figure 4.11 shows the spectroscopy of a cell filled with bottled krypton gas. Compared to argon, where ^{40}Ar (99.7%) is the most abundant isotope by a few orders of magnitude, krypton has several abundant isotopes. The spectroscopy signal clearly shows the resonance peaks of ^{82}Kr (12%),^{83}Kr (12%),^{84}Kr (57%) and ^{86}Kr (17%) (Beer, McCracken, and Steiger, 2012). A laser lock on all of the shown peaks is possible and allows for more options compared to argon, where the laser can only be locked on the ^{40}Ar peak.

The fiber-coupled closed spectroscopy cell is ideal for a setup that aims for high sample throughput routine measurements. The breakdown time of the apparatus due to broken spectroscopy cells can be reduced by having a spare setup, which only requires replugging of the fibers. The plasma cell itself can be refilled by melting it onto the glass tube again.

Home-built Tapered Amplifier Setup

The required laser power for the different atomic optical devices is provided by tapered amplifiers. The core element is a tapered semi-conductor diode which amplifies the inserted light by stimulated emission. The modular approach of the new setup demands a plug-and-play solution, i.e. a fiber-coupled input and output, which has been addressed in the scope of this work.

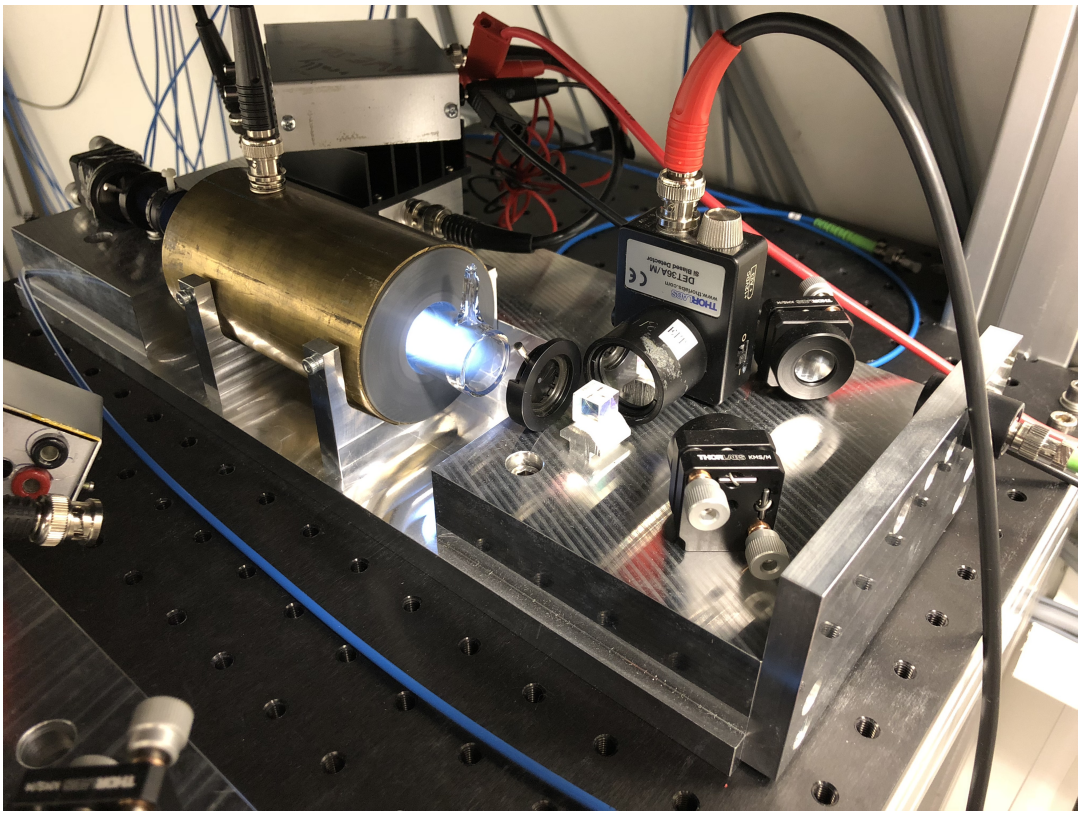

FIGURE 4.10: The realized fiber-coupled closed spectroscopy cell. The light is introduced by a polarization-maintaining fiber and two mirrors acting as a periscope. The pump beam is attenuated after passing the cell and retro-reflected for a Doppler-free saturation spectroscopy.

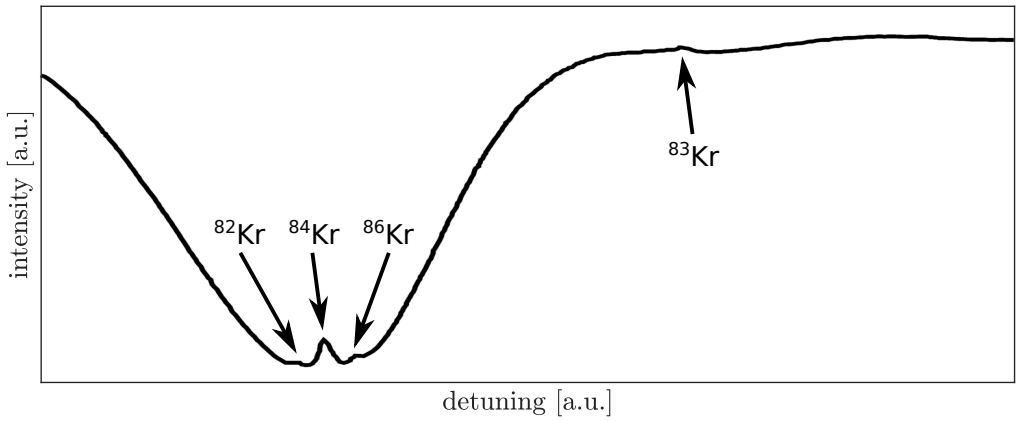

FIGURE 4.11: Spectroscopy signal of krypton. One closed spectroscopy cell has been filled with bottled krypton and shows the most abundant isotopes ^{82}Kr (12%),^{83}Kr (12%),^{84}Kr (57%) and ^{86}Kr (17%). The even number isotopes are shifted due to the mass difference of the nucleus whereas the odd number isotopes possess nuclear spin and therefore hyperfine structure, shifting them further away. The master laser can be locked easily to any of the shown transitions.

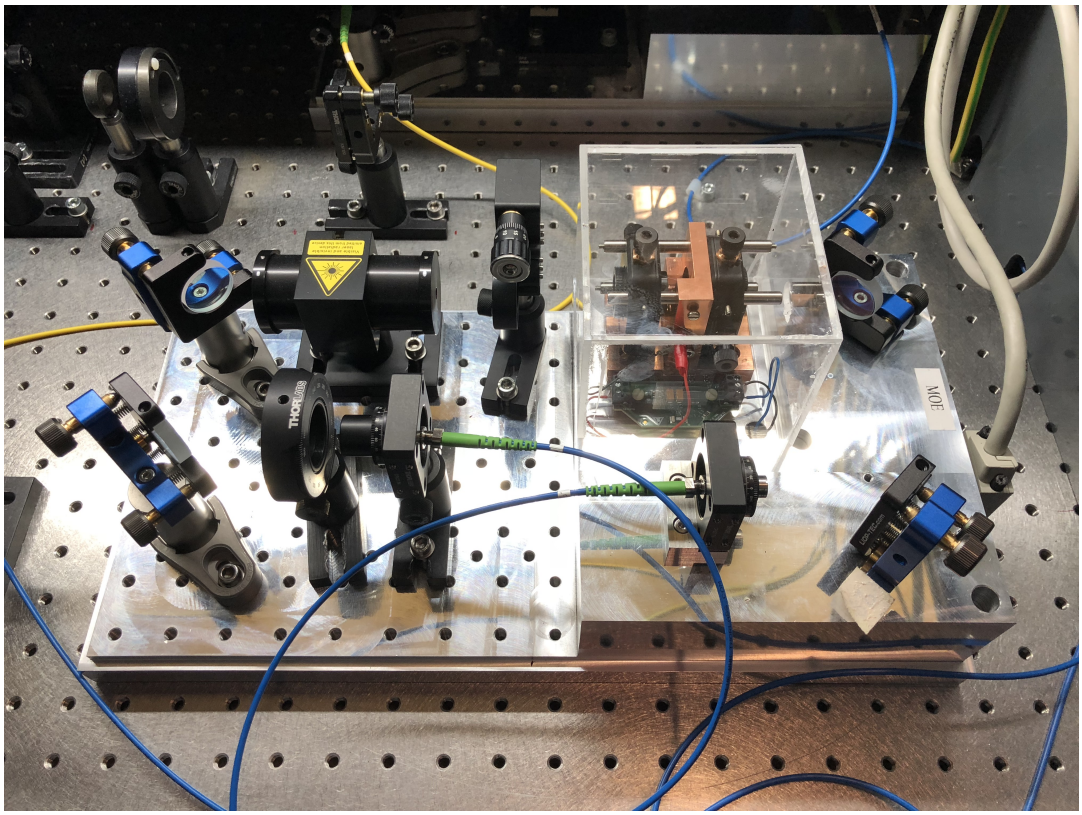

FIGURE 4.12: The realized tapered amplifier. The setup is decoupled from the optics module by optical fibers. The core component is a copper holder for the tapered amplifier diode with a 30 mm cage system to hold the aspheric lenses mounted in x-y-z-translation stages. The light passes a 60 dB optical isolator to prevent back-reflections into the diode.

The realized design of the home-built fiber-coupled tapered amplifier setup is shown in Figure 4.12 and more details can be found in Nicolai, 2017. The crucial part is the holder for the tapered amplifier diode and the alignment of the two aspheric lenses on both sides. A custom made copper block is deployed here and a 30 mm cage system is used to mount x-y-z-translation stages which hold the aspheric lenses (Thorlabs). The input light that comes out of a fiber is incoupled by two mirrors to provide enough degrees of freedom for a proper alignment of the laser beam with respect to the input facet of the tapered amplifier diode. The astigmatism of the output of the diode is corrected with a cylindrical lens. Great care has to be taken to prevent any back-reflected light which can destroy the chip by passing it opposite to the taper, thus a 60 dB optical Faraday isolator has been installed. The amplified laser beam is aligned by two additional mirrors and coupled into the fiber.

The state-of-the-art tapered amplifier diodes at 812 nm can amplify up to a maximum output around 2 Watt of optical power. The large output facet yields additional spatial modes that have to be compensated by the optics to improve coupling into single-mode fibers. A typical coupling efficiency is around $50 - 60$ % and yields

overall gains of $\sim$ 20 dB. These values are dependent on the individual tapered amplifier chip since strong deviations from diode to diode have been observed.

4.3.2 Frequency Shifting and Mixing

The purpose of the frequency shifting and mixing module is to transform the four basic frequencies of the laser setup and light amplification module, that is described in the previous subsection, into the required frequencies for the atom optical components. A construction plan of this module is shown in Figure 4.13.

The incoming light of the first slave laser is divided into independent paths where double passed acousto-optical modulators provide the necessary shift to reach the exact cooling frequencies needed for each atom optical device, namely the collimator, the two-stage Zeeman slower and the magneto-optical trap. The 2D and 3D magneto-optical traps share the same frequencies in this setup. The frequencies for the first and third repumping transitions are generated likewise from master and second slave laser respectively.

These seven frequencies are coupled into short intermediate fibers to deliver the light to the mixing module. The first and second repumper light is mixed as they are required for every device except for the Zeeman slower. A part is mixed with the frequency for magneto-optical trapping and the other part is mixed with the third repumper and ultimately with the collimator cooling frequency. The light mixtures are then coupled into optical fibers for delivery to the atom optical devices.

4.4 Atomic Module

The atomic module includes all atom optical devices such as a metastable argon source, two transverse cooling stages, Zeeman slower, magneto-optical trap and flux monitoring. The required light for the optical transitions is delivered through fiber optics from the optics module to the components. The atoms enter the apparatus at nearly room temperature thermal velocities, cooled to liquid nitrogen temperatures and then slowed down to nearly zero velocity in the magneto-optical trap. A tilted mirror design is used as first transverse laser cooling stage and collimates the atoms from the effusive source into a beam. The remaining optical Doppler shifts that arise from the longitudinal velocities are compensated mainly by the linear Zeeman shift due to magnetic fields and the deceleration is performed in the Zeeman slower. In the magneto-optical trap, the Zeeman shift is used to balance the relative strength of the counter-propagating beams and sets a preferred spatial trapping region, i.e. the zero point of the magnetic field. Further atom optical devices use the abundant ^{40}Ar

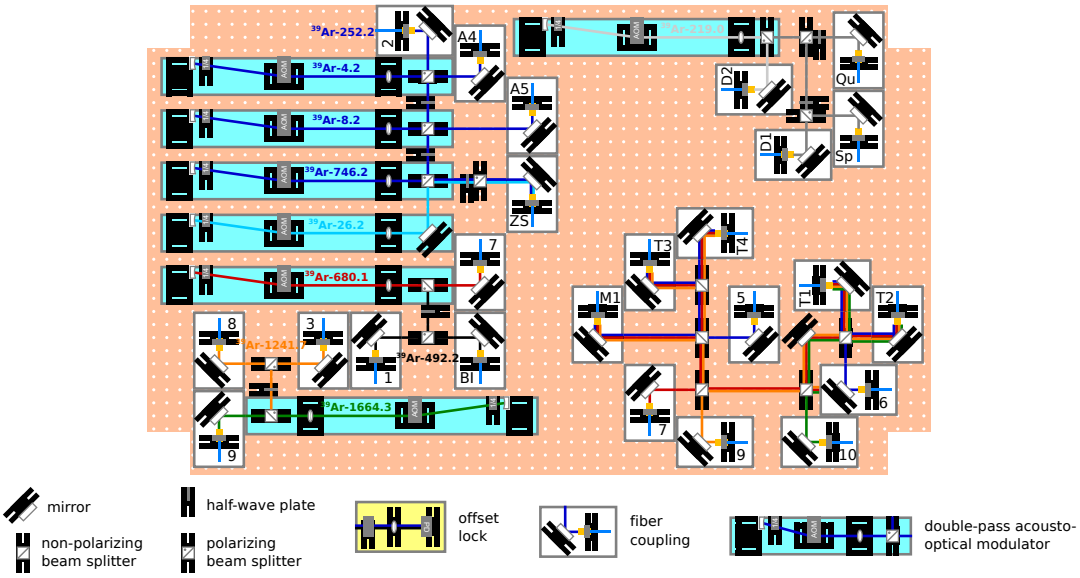

FIGURE 4.13: Construction plan for the frequency shifting and mixing. The setup transforms the four basic frequencies of the laser and amplification part into the required frequencies for the atom optical devices. First, the exact frequencies are generated by double pass acousto-optical modulators and coupled into intermediate fibers. These are then mixed in the lower right part of the table and coupled into the final fibers to provide light for the atom optical components.

as flux and beam monitoring.

A vacuum setup is required for Trap Trace Analysis of argon and krypton and is designed for high sample throughput in an (ultra-)high vacuum environment. Several turbo-molecular pumps and three differential pumping stages are deployed to generate the required pressure gradient from the high pressure source to the low pressure detection region. A getter-pump cleans the recycled sample of any non-noble content. A further turbo-molecular pump compresses the sample into a buffer volume before inserting it into the high pressure source again.

4.4.1 Vacuum System

A scheme of the vacuum setup is shown in Figure 4.14. The (ultra-)high vacuum system is required for Trap Trace Analysis of argon and krypton due to the following reasons:

- The sample needs to be isolated from the environment due to noble gases in the air. A closed system further enables sample recycling thus reducing the required sample size by three orders of magnitude compared to throughput.

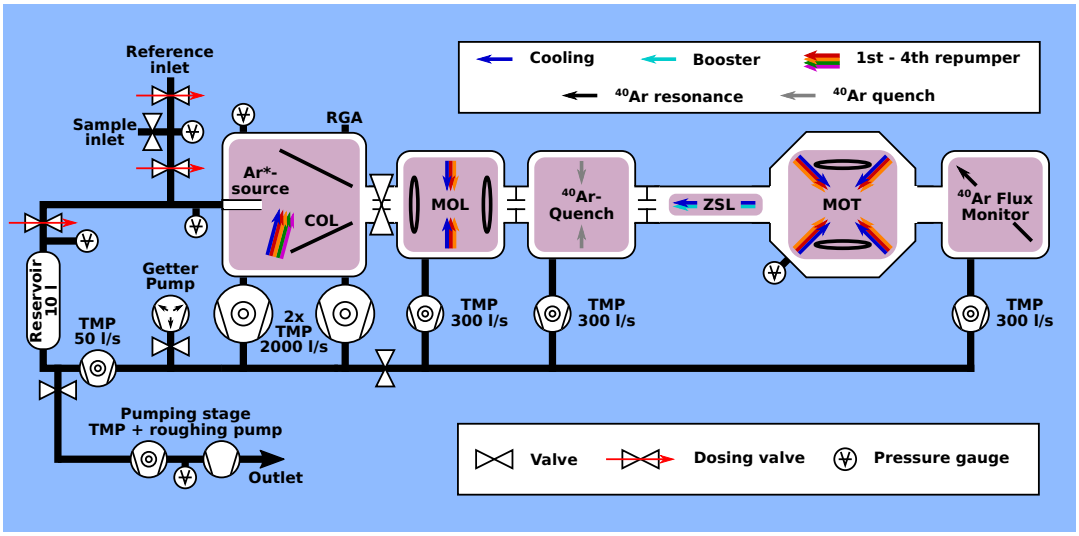

FIGURE 4.14: Scheme of the vacuum setup. The sample enters the apparatus through a pipette to determine the sample volume. It is then pumped into a reservoir serving as a buffer volume. The compressed gas enters the high pressure source and is manipulated by the atom optical components. Several turbo-molecular pumps collect the sample again and a getter-pump cleans it from any non-noble content. A further turbo-molecular pump compresses the gas into the reservoir again thus closing the cycle. A pumping stage is deployed for removing the sample from the apparatus. The atom optical components are sketched with the required optical frequencies.

- The magneto-optical trap is designed for atoms close to zero velocity. Each collision with the non-cooled thermal background gas will release the trapped atoms thus reducing lifetime and impede detection.
- The noble gases have to be prepared into a metastable state with no direct dipole decay channel to the ground state. Still, deexcitations to the ground state occur due to collisions both among metastables and between metastables and background gas.

The atomic beam travels through a main line connected by DN 40 CF flanges. Differential pumping is deployed by three tubes of 18 to 20 mm inner diameter, inserted between two adjacent vacuum chambers. The custom made vacuum chambers were manufactured by Vacom.

The stainless frame of the apparatus has been custom-made by the workshop and a computer-aided design is shown in Figure 4.15. It is designed following the modular approach so that the parts holding the source chamber, intermediate chambers and magneto-optical trap are self-supporting and can be adjusted separately in the future.

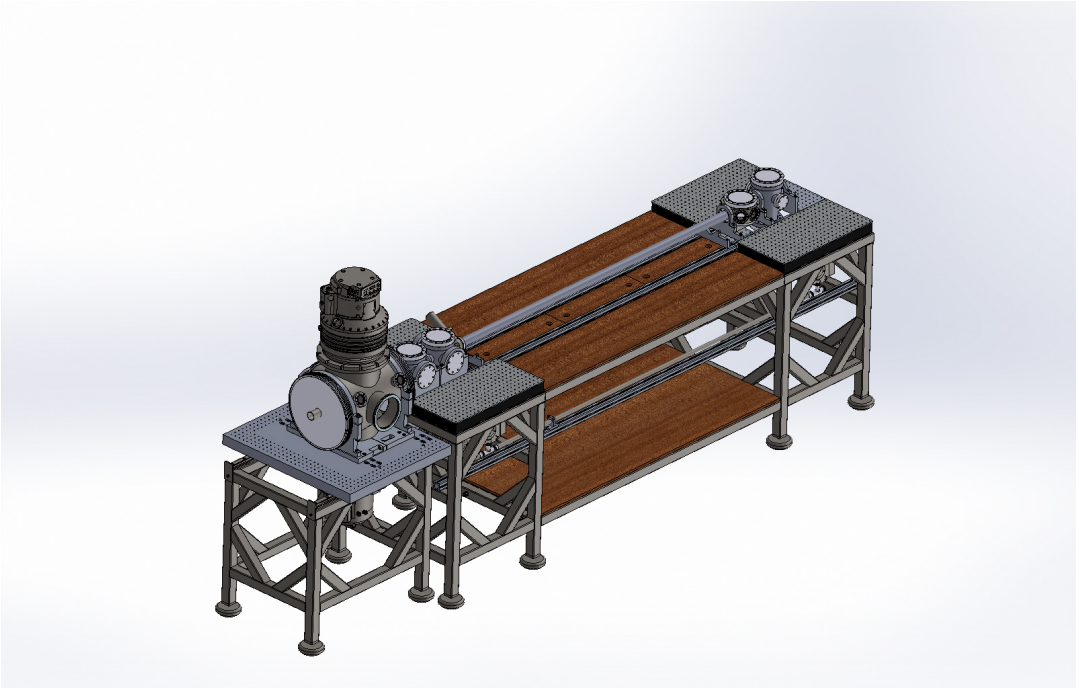

FIGURE 4.15: Computer-aided design (CAD) of the vacuum setup. The source chamber holds two 2000 $\frac{l}{s}$ turbo-molecular pumps (Pfeiffer HiPace2300) and is mounted on a translation table to give access to the collimator. The remaining vacuum chambers are mounted on an aluminum construction profile (Item Profile 10 50x50) to enable easy alignment. Three 300 $\frac{l}{s}$ pumps (Pfeiffer HiPace300) are mounted on a three-way cross below the chambers and the outlets are connected to collect the sample from the main apparatus. The stainless steel frame consists of mainly three tables. The middle part can be replaced for a future design of the Zeeman slower with a different length.

The source chamber is basically a large six-way cross. The first axis is aligned to the atomic beam direction and has two DN 320 ISO-K flanges for connecting the collimator and source. The dimensions have been chosen to increase the radial distance of the collimator mirrors to the plasma in the source, prolonging the lifetime of the mirror coatings. The second, vertical axis has suitable DN 250 ISO-F flanges for the two 2000 $\frac{l}{s}$ turbo-molecular pumps (Pfeiffer HiPace2300). The third, horizontal axis has DN 160 ISO-K flanges for viewports, which can be used to observe the ignition of the plasma and the quality of the collimator mirrors. Additionally, four DN 40 CF provide further access to the chamber. The residual gas analyzer is connected to one of these ports for mass spectrometry and leak testing. The chamber is mounted on a translation table whereas the flange holding the collimator is connected to the rest of the apparatus. This provides access to the collimator by moving the source chamber along the atom beam axis.

The rest of the apparatus is separated by a valve to close the remaining vacuum during adjustments in the source chamber. Three 300 $\frac{l}{s}$ turbo-molecular pumps (Pfeiffer HiPace 300) are mounted on a DN 100 CF three-way cross below custom

made six-way crosses. The axes aligned to the atomic beam have DN 40 CF flanges, the vertical axes holding the three-way cross have DN 100 CF flanges and the horizontal axes have DN 63 CF flanges in the case of the first two chambers. The chamber behind the magneto-optical trap has DN 40 CF flanges to provide more optical access to the atom trap that is in close proximity. The outlets of the turbo-molecular pumps are connected together and a tube with DN 16 CF flanges is used to transport the sample back to the reservoir. The vertical and horizontal axes are closed by viewports thus enabling optical access for laser beams for cooling, trapping and analyzing.

A $\sim$ 1.80 m tube with inner diameter of 40 mm is used inside the Zeeman slower. A tube with 20 mm inner diameter for differential pumping is inserted in the first 0.5 m of the Zeeman slower. This reduces the background gas pressure for the magneto-optical trap while allowing the collimated atomic beam to pass through. The frame below is non-carrying and only used as working surface thus can be replaced if future designs of the Zeeman slower have different lengths.

The core part is a ten-way cross (Kimball MCF600-SphOct-F2C8) for the magneto-optical trap with eight DN 40 CF flanges and two DN 100 CF flanges. Two DN 40 CF flanges are aligned to the atomic beam direction. The two vertical and the four 45° -tilted horizontal flanges are used for the six cooling and trapping beams. The remaining two viewports are used for single-atom detection by an avalanche-photodiode (APD) and a charged-coupled device (CCD) camera.

The vacuum chambers are mounted on an aluminum construction profile (Item Profile 10 50x50) to enable easy alignment of the chambers. The stainless steel frame holds the aluminum profile and the translation table of the source chamber. It further holds four breadboards (M-PG-12-2-ML) and some custom made aluminum plates to mount the necessary optics for the atom optical devices.

4.4.2 Metastable Atom Source

The transition from the ground state $1s_1$[2] to the excited state $1s_4$ lies in the ultraviolet and is $\sim$ 107 nm for argon and $\sim$ 124 nm for krypton. To address these optical transitions is not feasible since the light at these wavelengths is scattered by air and laser systems have to be set up in vacuum. Approaches on optical excitation using incoherent light have been tried for krypton (Kohler et al., 2014) but are not yet at sufficient stability and efficiency for this purpose.

[2]It is sometimes referred to as $1p_0$ to reflect the selection rule $\Delta L = \pm 1$.

The laser cooling and trapping uses a higher transition at 812 nm from the metastable state $1s_5$ with total angular momentum quantum number $J = 2$ to the state $2p_9$ with $J = 3$.

A common approach to generate metastable noble gases is a radio-frequency induced plasma. These noble gas plasmas have two main features (Lieberman and Lichtenberg, 1994):

- The plasma is weakly-ionized ($\sim 10^{-3}$) due to the closed shells of noble gases yielding strongly bound valence electrons.
- The electrons and ions are not in thermal equilibrium due to the typical low operating pressures of $< 10^{-1}$ mbar yielding low densities.

The higher mobility yields electron velocities typically $\sim$ 100 times faster than the velocities of the ions (Lieberman and Lichtenberg, 1994) and ground-state atoms. The collisions between electrons and ground-state atoms result in inelastic electron-impact excitations

$$e^- + Ar \rightarrow Ar^* + e^- \rightarrow Ar + e^- + \hbar\omega. \tag{4.1}$$

The same holds for krypton. The emittance of the photon with energy $E = \hbar\omega$ in the second step only occurs with high probability if a dipole transition to the ground state exists. If Ar^* is a metastable state, the atom will remain in this state for a long time compared to the average collision time. This is because other radiative transitions such as electric quadrupole and magnetic dipole radiation are comparably weak (Lieberman and Lichtenberg, 1994).

The ground state atoms, metastables and ions are typically in thermal equilibrium with the environment and liquid nitrogen is deployed for precooling of the atoms through a thermal contact with a tube in the source.

Figure 4.16 shows an image of the metastable atom source with the ignited plasma. The inset shows a photo taken through an infra-red viewer and the laser beam of the Zeeman slower is scattered by the atoms.

4.4.3 Transverse Cooling Stages

The effusion of metastable atoms from the source leads to transverse and longitudinal velocity distributions. The most probable velocity is 514 $\frac{\mathrm{m}}{\mathrm{s}}$ without cooling and 243 $\frac{\mathrm{m}}{\mathrm{s}}$ (Feng, 2012) with liquid nitrogen cooling. Only a fraction of atoms will reach the magneto-optical trap due to the small solid angle, thus two transverse laser cooling stages are deployed to increase the atom beam flux into the trappable region.

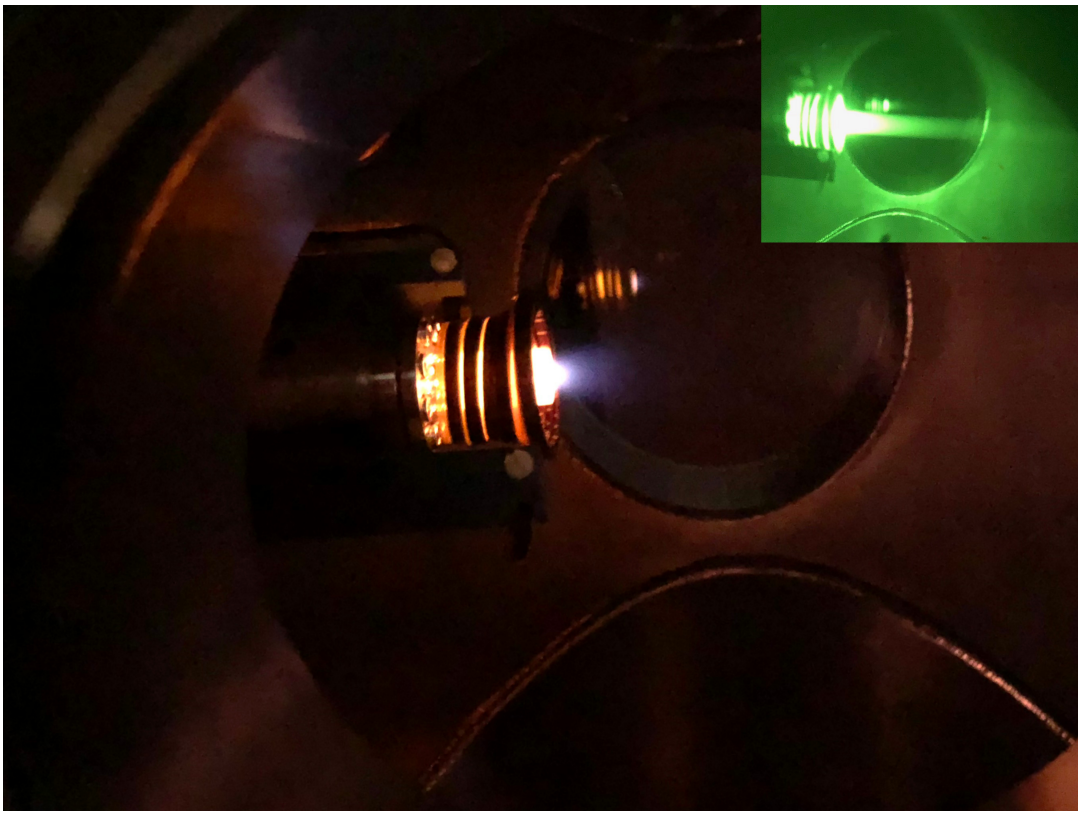

FIGURE 4.16: Image of the metastable atom source. The plasma is ignited by applying a radio-frequency at $\sim$ 60 MHz enhanced by a 35 Watt amplifier. The inset is a photo taken through an infra-red viewer and shows the scattered light from the Zeeman slower beam.

Collimator

The first transverse laser cooling device is called collimator and increases the flux of metastable atoms to the detection region by a factor of $\sim$ 100 (Ebser, 2018). The collimator is installed directly after the metastable source and compensates the Doppler shift due to the transverse velocities through a tilted mirror design. The change of angle of incidence after every reflection of the laser beams retains the resonance with the atoms over a distance of $\sim$ 20 cm.

The light produced by the optics module includes the frequencies for cooling and the first three repumpers. It is induced by a vacuum fiber throughput and optics for shaping the laser beam are mounted on a 30 mm cage system (Thorlabs). The incoming angle to the mirrors is fixed and aligned once. Each axis has one fixed mirror and one where the two rotational degrees of freedom can be adjusted by stepper motors. Additionally, the collimator itself is installed on a large custom-made kinematics mount and can be tilted as a whole.

Figure 4.17 shows the computer-aided design (CAD) construction model of the realized collimator. It mainly follows the design described in Ebser, 2018 but with

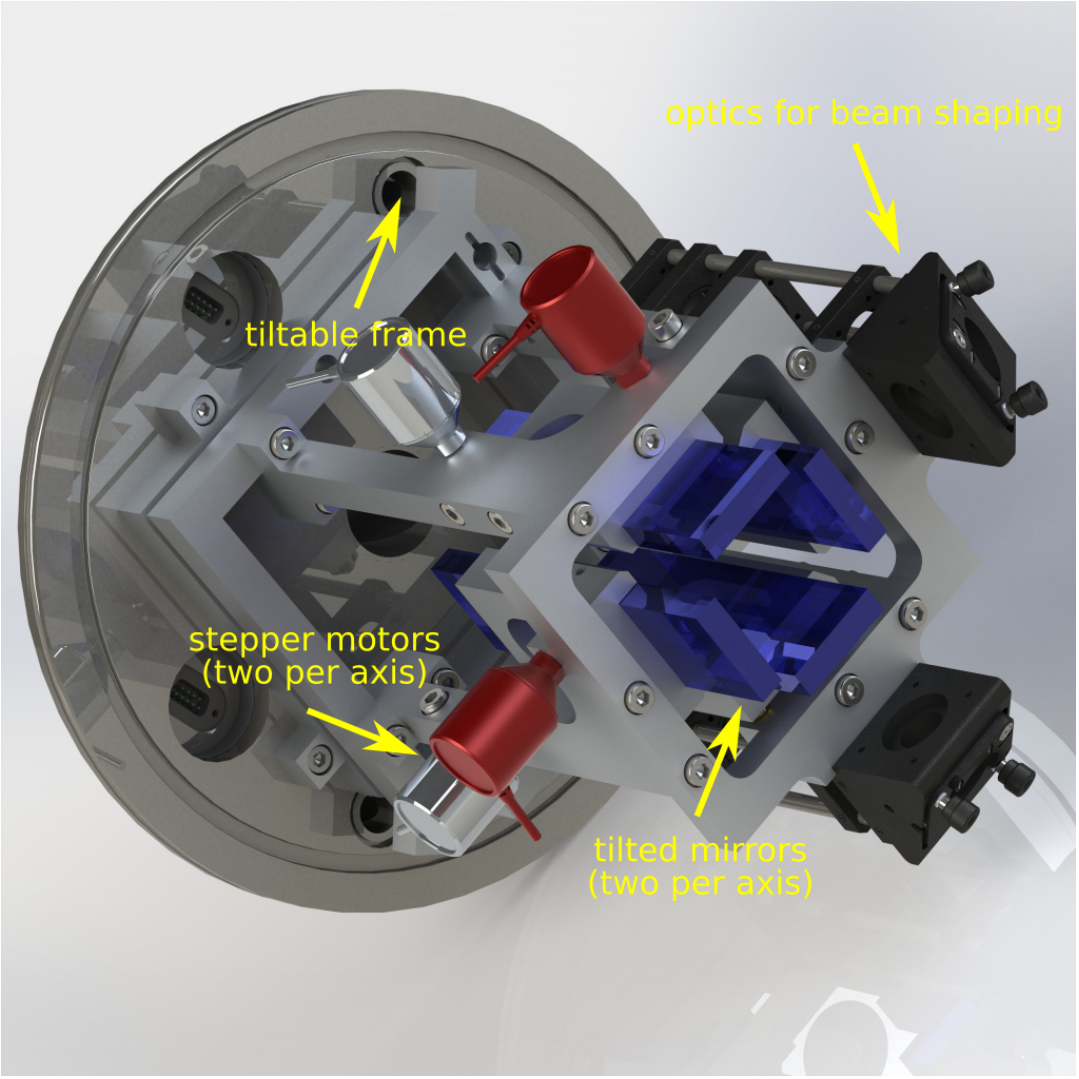

FIGURE 4.17: Computer-aided design (CAD) of the collimator. One of the tilted mirrors per axis can be adjusted by two stepper motors thus can be optimized with the atom flux signal. The optics for laser beam shaping are mounted inside a 30 mm cage system (Thorlabs) and are adjusted once outside the vacuum. The whole frame can be tilted since it is mounted on an adjustable holder. Taken from Ebser, 2018.

small modifications in the radial dimension. A degradation of the mirrors over time has been observed on the prototype apparatus and is attributed to the plasma and its sputtering properties. The larger source chamber allows to move the mirrors further away in the radial direction thus reducing this degradation effect for the new apparatus.

2D Magneto-Optical Trap

The atom beam flux that exits the collimator has close to zero transverse velocity, but the beam has still a large diameter compared to the detection region. A second

transverse cooling stage is deployed using a two-dimensional magneto-optical trap, often called magneto-optical lens due to the function of focusing the atomic beam. To ensure the same gradient for both axes, the quadrupole field has been orientated such that the axial direction is in atomic beam direction thus using the symmetric radial field as gradient.

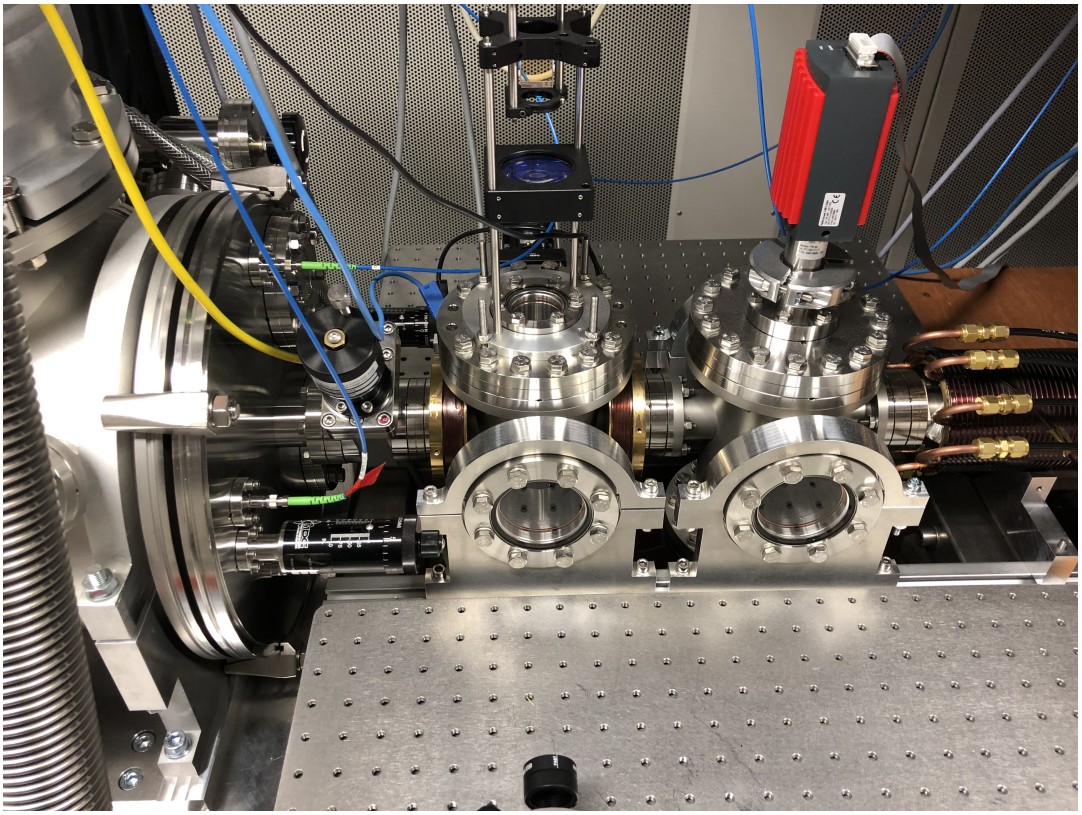

FIGURE 4.18: Realization of the 2D magneto-optical trap. The brass holders are designed to be mountable on the DN 40 CF flanges and have a groove to hold the 15×15 windings of each coil.

Figure 4.18 shows the realized two-dimensional magneto-optical trap. The 15×15 windings for each coil are placed in a groove on a brass holder which can be mounted on the DN 40 CF flanges connecting adjacent vacuum chambers. Water-cooling is not necessary for the ~ 2 A flowing in series through the coils with wires of 1 mm diameter.

4.4.4 Calculation of the Magnetic Fields

The Biot-Savart law describes the magnetic field B at position $\mathbf{r}$ generated by a current I at position $\mathbf{l}$ and is given by

$$\mathbf{B}(\mathbf{r}) = \frac{\mu_0 I}{4\pi} \int d\mathbf{l} \times \frac{\mathbf{r} - \mathbf{l}}{|\mathbf{r} - \mathbf{l}|^3} \tag{4.2}$$

with vacuum permeability μ_0.

Although analytically solutions exist for special coil configurations as the Maxwell coil, numerical calculations of the magnetic field yield far more insight and are not limited by the given geometry.

The magnetic field $\mathbf{B}(\mathbf{r})$ in Cartesian coordinates $\mathbf{r} = \begin{pmatrix} x \\ y \\ z \end{pmatrix}$ with resolution $d\mathbf{r} = \begin{pmatrix} dx \\ dy \\ dz \end{pmatrix}$ can be calculated using the differential form

$$d\mathbf{B}(\mathbf{r}) = \frac{\mu_0 I}{4\pi} \frac{\mathbf{r} - \mathbf{l}}{|\mathbf{r} - \mathbf{l}|^3} d\mathbf{l} \tag{4.3}$$

of the Biot-Savart law. In the case of circular coils that share the same axial direction, the situation can be parameterized in cylindrical coordinates with ϕ and resolution $d\phi$. The coils are then described by segments at $\mathbf{l} = \begin{pmatrix} R\cos\phi \\ R\sin\phi \\ z \end{pmatrix}$ and length $d\mathbf{l} = \begin{pmatrix} -R\sin\phi \\ R\cos\phi \\ 0 \end{pmatrix} d\phi$. By choosing the axis of the coils in z-direction, only the x-values need to be calculated for the radial position.

The magnetic fields presented in the scope of this work have all been calculated numerically with this method. The fields of the atom optical components can be added due to the linearity of Maxwell's equations and Figure 4.19 shows the total magnetic field in atomic beam direction of the Zeeman slower, compensation coil and magneto-optical trap.

4.4.5 Longitudinal Cooling by Zeeman Slowing

A crucial part for capturing atoms in the trap is to slow the majority of them below the capture velocity of the magneto-optical trap. The deceleration from thermal velocities yields a varying optical Doppler shift that has to be compensated. A common method has been presented in Phillips and Metcalf, 1982 by using the linear Zeeman effect induced by a magnetic field to shift the energy levels of the cycling transition to match the changing Doppler shift. The here installed Zeeman slower pursues a constant deceleration of the atoms and therefore constrains the magnetic field gradient, but other approaches are also possible (Ohayon and Ron, 2015).

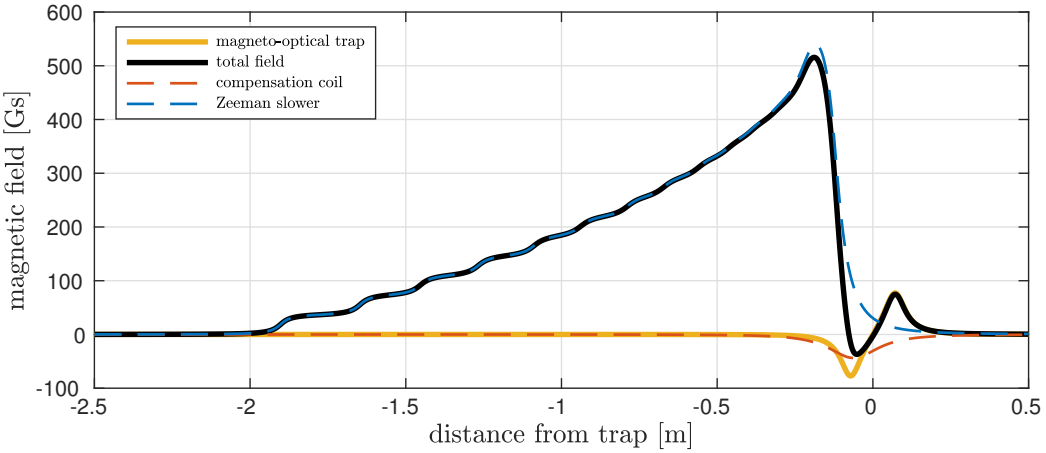

FIGURE 4.19: The total magnetic field along the beam line. The Zeeman slower, compensation coil and the quadrupole field of the magneto-optical trap are added yielding the total field strength. The compensation coil is required to reduce the high field at the exit of the Zeeman slower and yields the desired zero-crossing at the center of the magneto-optical trap.

Equation of Motion

The equation of motion for a constant deceleration $-a$ from initial velocity v_i to final velocity $v_\mathrm{f} < v_\mathrm{i}$ is given by

$$x(t) = \int_0^t v(t')dt' = v_i t - \frac{a}{2}t^2. \tag{4.4}$$

The solution for time $t(x) = \frac{v_i}{a} \pm \sqrt{\frac{v_i^2}{a^2} - \frac{2x}{a}}$ and neglecting $t < 0$ leads to the position-dependent velocity

$$v(x) = v(t(x)) = v_i - at(x) = \sqrt{v_i^2 - 2ax}. \tag{4.5}$$

The length l is dependent on $v(l) = v_f$ and yields

$$l = \frac{v_i^2 - v_f^2}{2a}. \tag{4.6}$$

Atom-light Interaction in a Magnetic Field

The resonance frequency ω of an atom with velocity $\vec{v}$ in a static magnetic field $\vec{B} = B(x)\vec{e}_x$ is given by

$$\omega(\vec{r},\vec{v}) = \omega_A + \vec{k}_L\vec{v}(r) + \frac{\mu'}{\hbar}\vec{B}(\vec{r}) = \omega_A - k_L v(x) + \frac{\mu'}{\hbar}B(x) \tag{4.7}$$

with wave vector $k_L = \frac{2\pi}{\lambda}$ and effective magnetic moment

$$\mu' = (m_e g_e - m_g g_g)\mu_B, \tag{4.8}$$

where μ_B denotes the Bohr magneton, $m_{e,g}$ is the respective magnetic quantum number and $g_{e,g}$ the corresponding Landé g-factor of the state.

Fortunately concerning different isotope species, $\mu' = \mu_B$ for the cooling transition in both ^{40}Ar ($J = 2 \rightarrow J' = 3$) and ^{39}Ar ($F = \frac{13}{2} \rightarrow F' = \frac{11}{2}$).

The resonance frequency has to be equal to the laser frequency $\omega_L = \omega_A + \Delta_L$ and yields the condition

$$B(x) = \frac{\hbar}{\mu'}(\Delta_L + k_L v(x)) = \frac{\hbar}{\mu'}(\Delta_L + k_L\sqrt{v_i^2 - 2ax}). \tag{4.9}$$

The maximum deceleration is given by $a_{textmax} = \frac{F_{textmax}}{m} = \frac{\hbar k_L \gamma}{2m}$ with atom mass m and natural line width γ. A deceleration $a = \frac{dv}{dt} = \frac{dv}{dx}\frac{dx}{dt} = \frac{dv}{dx}v(x) \leq a_{textmax}$ is chosen to compensate for magnetic field inhomogeneities.

This sets an upper limit for the maximum magnetic field gradient

$$-\frac{\mu'}{\hbar k_L}\frac{dB}{dx}v(x) = a \leq a_{textmax}. \tag{4.10}$$

Magnetic Field of an Increasing Field Slower

The quantization axis is defined by the magnetic field and the sign of the effective magnetic moment μ' is given by the choice of the laser light polarization. Together with the detuning Δ_L, different types of slowing configurations can be realized. For σ^--light and $\Delta_L = -k_L v_i$, the magnetic field

$$B(x) = \frac{\hbar k_L}{\mu'}(-v_i + \sqrt{v_i^2 - 2ax}) \tag{4.11}$$

is increasing from $B(0) = 0$. The chosen initial and final velocities are $700\frac{\mathrm{m}}{\mathrm{s}}$ and $20\frac{\mathrm{m}}{\mathrm{s}}$ respectively. The resulting magnetic field $B_{texttheo}$ is shown in Figure 4.22.

Construction of the Zeeman Slower

The chosen Zeeman slower design is the same as the one described in Welte, 2011. The magnetic field is generated by a current flowing through a single wire of $\sim 1,000$ m with increasing number of windings. The number of layers at a given position is shown in Figure 4.20.

The construction of the Zeeman slower has to be optimized under certain considerations. The homogeneity of the magnetic field in radial direction can be increased by the use of larger coils but this yields higher current flow thus higher heat production to obtain the same field strength. The realized magnetic field coil is mounted

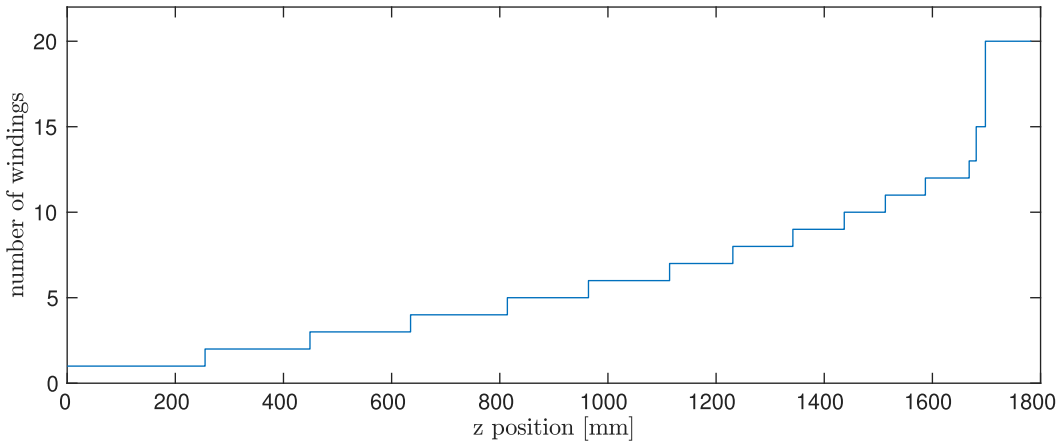

FIGURE 4.20: Schematic of the winding number. The increasing field towards the magneto-optical trap is generated by an increasing number of windings. The Zeeman slower coils have been built up layer by layer. The first of twenty layers covers the whole length of 1780 mm whereas the last layer starts 100 mm from the end.

on a brass tube with outer diameter of 100 mm. The power consumption for the required magnetic field is $\sim$ 570 Watts and water cooling is applied by copper pipes in grooves of the brass holder. The layers of copper wire for the coil are glued to the brass tube using a thermally conductive epoxy (Stycast). Figure 4.21 shows the construction of the Zeeman slower coil with the help of a slowly turning lathe.

The magnetic field of the finished coil has been measured by a Hall probe and Figure 4.22 shows the measured field compared to an ideal field and the result of numerical calculations of the coil setup. The unavoidable inhomogeneities in the field have to be taken into account and the Zeeman slower has been designed for a deceleration $a = 0.6a_{textmax}$ thus compensating by using magnetic field gradients below the theoretically possible gradient.

A further important characteristic of the magnetic field is its homogeneity across the finite atomic beam. Figure 4.23 shows the field parallel and perpendicular to the direction of the atomic flux in dependence on the radial position. The resulting transverse inhomogeneities of the deployed setup are below 1 % in the region of interest and are therefore negligible.

4.5 Magneto-Optical Trap

The atomic beam which leaves the Zeeman slower is further laser cooled and finally trapped in a spatially confined region by the magneto-optical trap, i.e. reducing the phase space volume occupied by the atoms. A force dependent on both position and

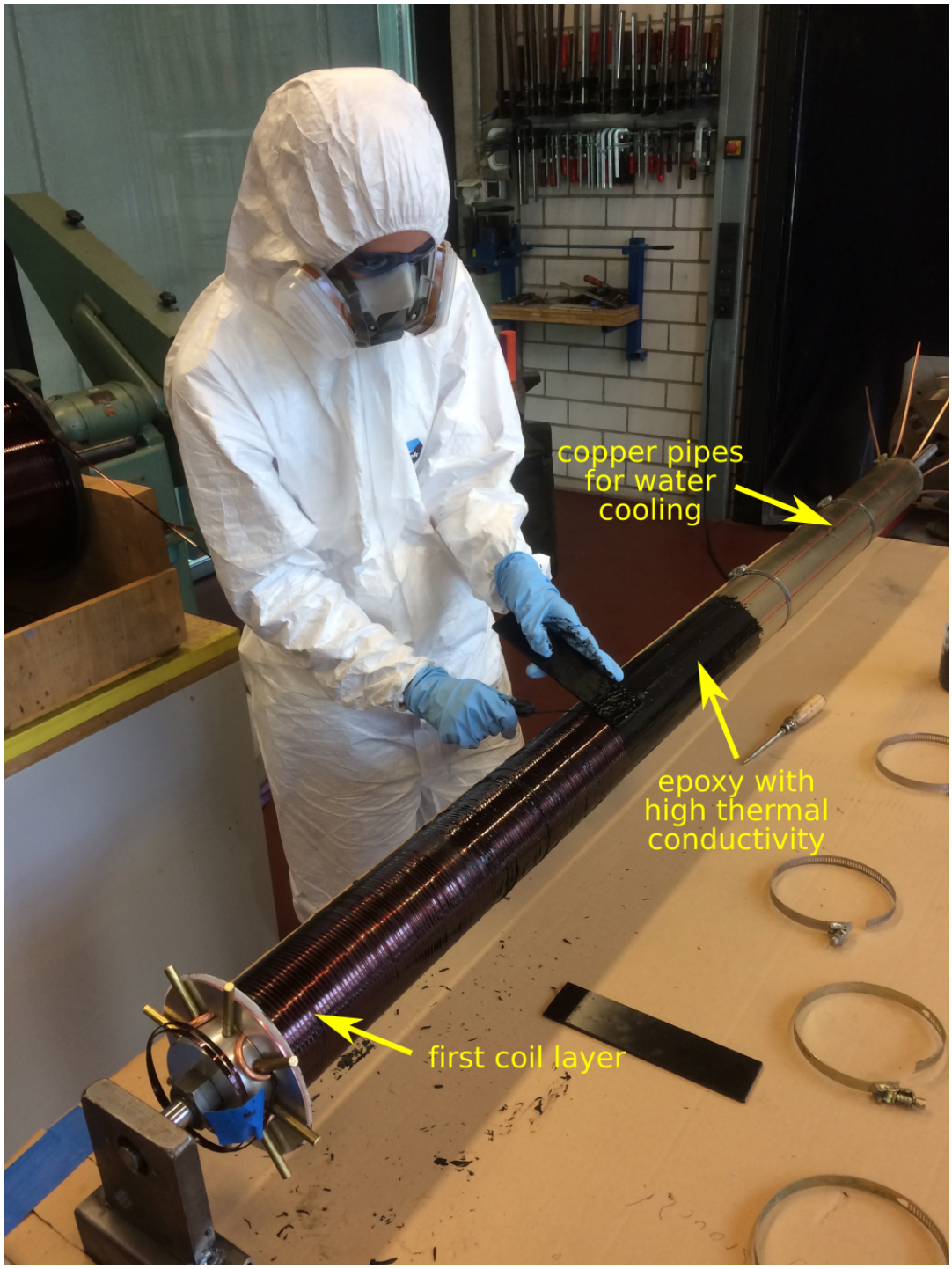

FIGURE 4.21: Construction of the Zeeman slower coil. The $\sim 1,000$ m of copper wire are mounted on a brass tube. The increasing number of layers yields the desired increasing magnetic field and the wire is glued using a thermal conductive epoxy (Stycast). To obtain the required field strength, ~ 570 W of electric power are consumed by the coil and water cooling is applied by copper pipes in grooves of the brass tube. A slowly turning lathe is used to wind the coil.

velocity is required for this process and is described in the following.

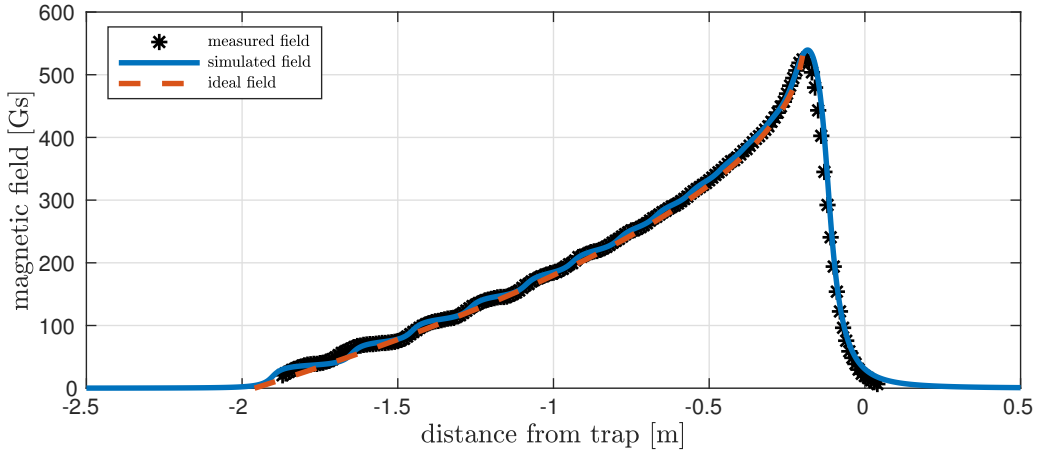

FIGURE 4.22: The magnetic field of the Zeeman slower. The ideal field shown as dashed line in beam direction has been approached by adding the magnetic field of 2544 single coils in a numerical calculation shown as solid line. The asterisk are the field strength at the given position measured by a Hall probe. The inhomogeneities of the actual field are compensated by choosing a fudge factor of ~ 0.6 for the maximum deceleration of the atoms thus the maximum field gradient.

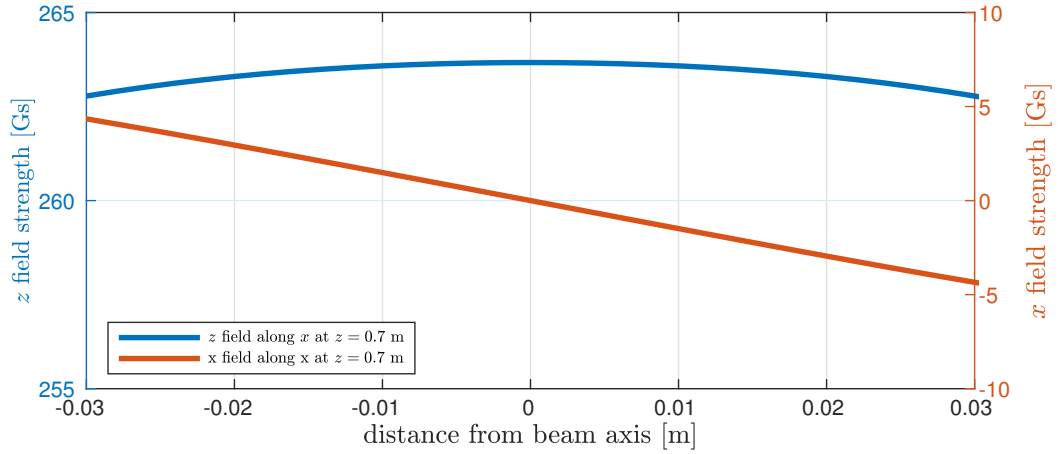

FIGURE 4.23: Transverse magnetic field inside the Zeeman slower. The homogeneity of the field in transverse direction is of importance since the atomic beam has a certain size of $10 - 20$ mm. The z field in beam direction is shown as well as the field perpendicular to the beam axis. In the region of interest around the center of the beam, the inhomogeneities are below 1 % of the absolute field strength and are therefore negligible.

4.5.1 Theoretical Description

The velocity dependent light force arises due to the sum of optical Doppler shift $-\mathbf{k} \cdot \mathbf{v}$ and the laser detuning δ. Two counter-propagating laser beams with wave vectors $\mathbf{k}_1 = \mathbf{k}$ and $\mathbf{k}_2 = -\mathbf{k}$ yield the total force

$$\mathbf{F}(\mathbf{v}) = \hbar\mathbf{k}\gamma_{textsp}\left(\frac{s_0}{1+s_0+\left(\frac{\delta-\mathbf{kv}}{\gamma_{textsp}}\right)^2} - \frac{s_0}{1+s_0+\left(\frac{\delta+\mathbf{kv}}{\gamma_{textsp}}\right)^2}\right) \tag{4.12}$$

with atom velocity $\mathbf{v}$, scattering rate γ_{textsp}, and the saturation parameter s_0. For small atom velocities in laser beam direction, i.e. $\mathbf{vk} = vk$, this can be expanded to

$$F(v) = 4\frac{\hbar k^2\delta}{\gamma_{textsp}}\frac{s_0}{\left(1+s_0+\left(\frac{\delta}{\gamma_{textsp}}\right)^2\right)^2}v = -\beta v. \tag{4.13}$$

If the detuning δ is negative, i.e. for red-detuned laser beams, this expression represents a damping force with damping coefficient β. The so captured and cooled atoms are called optical molasses and the temperature in these can be even lower than the Doppler temperature (Lett et al., 1988; Dalibard and Cohen-Tannoudji, 1989; Ungar et al., 1989).

Although the atoms can be cooled and hold by a pure optical molasses, a position dependent force is required to control the final position in the trap, enabling spatial confined detection thus reducing background by neglecting regions of unwanted stray light. A magnetic field adds a spatial component to the force by modifying the overall detuning to $\delta - \mathbf{kv} + \frac{\mu'}{\hbar}\mathbf{B}(\mathbf{r})$. This leads to a total velocity and position dependent force

$$\mathbf{F}(\mathbf{r},\mathbf{v}) = \hbar\mathbf{k}\gamma_{textsp}\left(\frac{s_0}{1+s_0+\left(\frac{\delta-\mathbf{kv}+\frac{\mu'}{\hbar}\mathbf{B}(\mathbf{r})}{\gamma_{textsp}}\right)^2} - \frac{s_0}{1+s_0+\left(\frac{\delta+\mathbf{kv}+\frac{\mu'}{\hbar}\mathbf{B}(\mathbf{r})}{\gamma_{textsp}}\right)^2}\right). \tag{4.14}$$

The magnetic field in the center of the magneto-optical trap is a good example, where the field can be calculated analytically. It deploys a pair of coils with radius R and distance $d = \sqrt{3}R$ with counter-propagating current I. This configuration is called Maxwell coil and is used to produce a homogeneous field gradient.

For $|\mathbf{r}-\mathbf{l}| \approx |\mathbf{l}|$, i.e. the region of interest is far smaller than the coil dimensions, the Biot-Savart law in equation 4.2 can be expanded by

$$\mathbf{B}(\mathbf{r}) = \frac{\mu_0 I}{4\pi}\int d\mathbf{l}\times(\mathbf{r}-\mathbf{l})\left(\frac{1}{|\mathbf{l}|^3} + \frac{3\mathbf{r}\cdot\mathbf{l}}{|\mathbf{l}|^5} + \ldots\right). \tag{4.15}$$

The magnetic field in the center of the coils can be calculated in cylindrical coordinates with $\mathbf{l} = R\cos(\phi)\hat{\mathbf{x}} + R\sin(\phi)\hat{\mathbf{y}} \pm \frac{d}{2}\hat{\mathbf{z}}$ and $d\mathbf{l} = R\phi d\phi$ and yields

$$\mathbf{B}_{\pm}(\mathbf{r}) = \pm\frac{\mu_0 I R^2}{2\left(R^2+\frac{d^2}{4}\right)^{3/2}}z + \frac{\frac{3d}{2}\mu_0 I R^2}{2\left(R^2+\frac{d^2}{4}\right)^{5/2}}\left(-\frac{x}{2},-\frac{y}{2},z\right) \tag{4.16}$$

for each coil. The total field of both coils is then

$$\mathbf{B}(\mathbf{r}) = \mathbf{B}_{+}(\mathbf{r}) + \mathbf{B}_{-}(\mathbf{r}) = B_0\left(\frac{x}{2},\frac{y}{2},-z\right) \tag{4.17}$$

with $B_0 = \frac{3d\mu_0 I R^2}{4\left(R^2+\frac{d}{4}\right)^{5/2}}$. As expected due to $\nabla\cdot\mathbf{B} = 0$ and symmetry considerations, the gradient in axial direction is twice the gradient in radial direction.

The deployed Maxwell coils produce a magnetic field with a homogeneous field gradient in their center. For simplicity, the axes of the three counter-propagating laser beams are aligned to the x, y, and z axes. The force in z-direction for small Doppler shifts $-kv_z$ and small Zeeman shifts $-\frac{\mu'}{\hbar}B_0 z$ can be expanded as

$$F_z = \hbar k\gamma_{textsp}\left(\frac{s_0}{1+s_0+\left(\frac{\delta-kv_z-\frac{\mu'}{\hbar}B_0 z}{\gamma_{textsp}}\right)^2} - \frac{s_0}{1+s_0+\left(\frac{\delta+kv_z+\frac{\mu'}{\hbar}B_0 z}{\gamma_{textsp}}\right)^2}\right) = -\beta v_z - \kappa z. \tag{4.18}$$

This is the equation of motion of a damped harmonic oscillator with spring constant $\frac{\kappa}{m}$ and damping $\frac{\beta}{m}$.

4.5.2 Design and Realization

The magneto-optical trap has been realized inside a ten-way cross (Kimball MCF600-SphOct-F2C8). This vacuum chamber provides two ports for the atomic beam and optical access for the six laser beams and two detection methods, i.e. avalanche-photodiode (APD) and imaging on a charged-coupled device (CCD) camera. The axis of the coils for the magnetic field are aligned to the vertical direction perpendicular to the incoming atomic beam.

Figure 4.24 shows a computer-aided design (CAD) of the magneto-optical trap. The special flat geometry of the ten-way cross is convenient for mounting the coils as close as possible to the trap, minimizing the distance d and radius $R = \frac{d}{\sqrt{3}}$ thus reducing required current and therefore heat output. The 15×15 windings of each coil are mounted in a groove on a brass holder. This holder is designed with a duct inside to provide water-cooling of the coils. The required cooling and trapping light, including the necessary repumper transitions, is delivered via a fiber per axis. In case of the vertical axis, the cage system holding the beam-shaping optics is mounted on the vacuum flange. The two horizontal axes are mounted on optical breadboard on

both sides of the magneto-optical trap.

The high magnetic field at the end of the Zeeman slower is compensated by an additional coil with current flowing in opposite direction. This compensation coil allows the reduction of the distance from the end of the Zeeman slower to the magneto-optical trap.

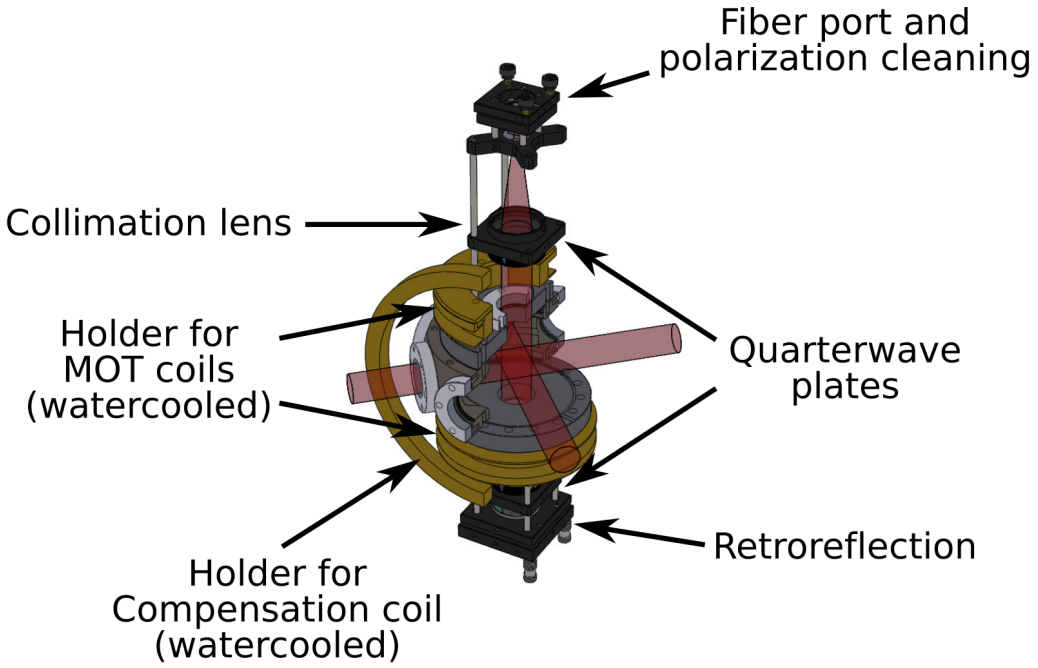

FIGURE 4.24: Computer-aided design (CAD) of the magneto-optical trap. The coils of the trap and Zeeman slower compensation have been optimized under the constraints of (i) homogeneity of the field, (ii) power consumption, (iii) and optical access. Water-cooling carries the produced heat outside the container. The core component is a ten-way cross (Kimball MCF600-SphOct-F2C8) aligned to the radial axis of the magneto-optical trap. The optical ports are DN 40 CF windows with anti-reflective coating to reduce power loss of the retro-reflected beams. The 60 mm cage system (Thorlabs) in radial direction is directly mounted on the modified DN 100 CF flanges and the light is inserted via optical fibers. The setup for the axial directions is similar, but they are mounted on the optical breadboards on both sides of the magneto-optical trap. The remaining ports are used for the atomic beam and the detection optics for the avalanche photodiode (APD) and charged-coupled device (CCD) camera.

Figure 4.25 shows the inside of the ten-way cross of the magneto-optical trap. Several considerations regarding single-atom detection have been addressed.

The stray light due to reflections on the blank stainless steel is reduced by a coating inside the vacuum. A special varnish (AZ Technology MLS-85-SB-C) usually used in space technology, i.e. in the Low Earth Orbit space environments, is applied

here and provides a low-outgassing layer of black paint which is required to maintain the ultra-high vacuum inside the magneto-optical trap.

The low signal of scattered light from single atoms is captured by a one-to-one telescope with maximum numerical aperture. This system is used for the avalanche-photodiode (APD) as well as for the imaging onto a charged-coupled device (CCD) camera. An aluminum tube coated with the black paint is mounted on grooves inside the ten-way cross and the lenses are chosen as such that the DN 40 CF windows are optimally used, i.e. maximizing the beam diameter. Two lenses per side are deployed to reduce aberrations and the corresponding second half of the telescope is mounted on the breadboard outside the vacuum.

FIGURE 4.25: Coating of the magneto-optical trap and detection optics. The blank stainless-steel surfaces on the inside of the vacuum chamber have been coated with a black paint (AZ Technology MLS-85-SB-C) to reduce stray light. The coating was developed for the use in the Low Earth Orbit space environments and has a low out-gassing rate, therefore suitable for the ultra-high vacuum environment in the magneto-optical trap. The aluminum lens holder tubes have been coated on the outer and inner side. The anti-reflective coated lenses are chosen as large as possible to maximize the numerical aperture and therefore the signal of single atoms.

The finished setup of the magneto-optical trap is shown in Figure 4.26. The

magneto-optical trap is mounted on the same aluminum profile as the other components to simplify the alignment of the beamline. The chamber is connected further downstream to a custom-made six-way cross, where a turbo-molecular pump is mounted. This setup allows for background pressures in the order of 10^{-8} mbar and pressures in the order of 10^{-7} during sample analysis. Additionally, this chamber provides optical access and is used for flux monitoring of abundant ^{40}Ar.

The magnetic field vectors and the absolute field strength inside the magneto-optical trap is shown in Figure 4.27. The high field strength at the exit of the Zeeman slower is compensated mostly by the compensation coil, but a small but negligible effect can be seen in the field lines compared to the pure magnetic field of the trap.

Figures 4.28 and 4.29 show the field and gradient in the direction of the moving atoms. The z-direction corresponds to the atomic beam direction whereas the x-direction is the vertical direction along the axis of the magneto-optical trap coils. The respective fields in z- and x-direction show the required zero-crossing and gradient for laser cooling and trapping. The gradient has been chosen as 20 $\frac{\mathrm{G}}{\mathrm{cm}}$ and ~ 10 $\frac{\mathrm{G}}{\mathrm{cm}}$ for axial and radial direction respectively. The magnetic field gradient and the red detuning of the laser beam are the main parameters for size and capture range of the magneto-optical trap and have been optimized using enriched ^{39}Ar in Welte, 2011.

4.6 Trapping of Argon and Krypton

A year after the delivery of the self-sufficient laboratory container, the first atoms have been trapped inside the magneto-optical trap. The work on the new apparatus in the scope of this thesis concludes with this huge milestone.

The progress is shown in Figure 4.30. The laser setup, vacuum system and atomic optical components have been designed and built up to the state, that capturing ^{40}Ar and ^{84}Kr has been possible. Beyond the crucial steps on the physical side required for the atom trapping, the infrastructure in the once empty container has been set up. This includes fresh air ventilation, IT connections and dispatcher for cooling water, compressed air and electricity.

Figure 4.31 shows the first image of trapped ^{84}Kr atoms projected on a charged-coupled device (CCD) camera. The optics module has been slightly modified for the trapping of krypton. The master laser has been replaced by another laser tuned to the wavelength at 811.290 nm for the same $1s_5 \rightarrow 2p_9$ transition in krypton. The fiber-coupled krypton spectroscopy cell has been used to lock the laser onto the exact transition of ^{84}Kr as shown in Figure 4.11. The modular setup has been beneficial

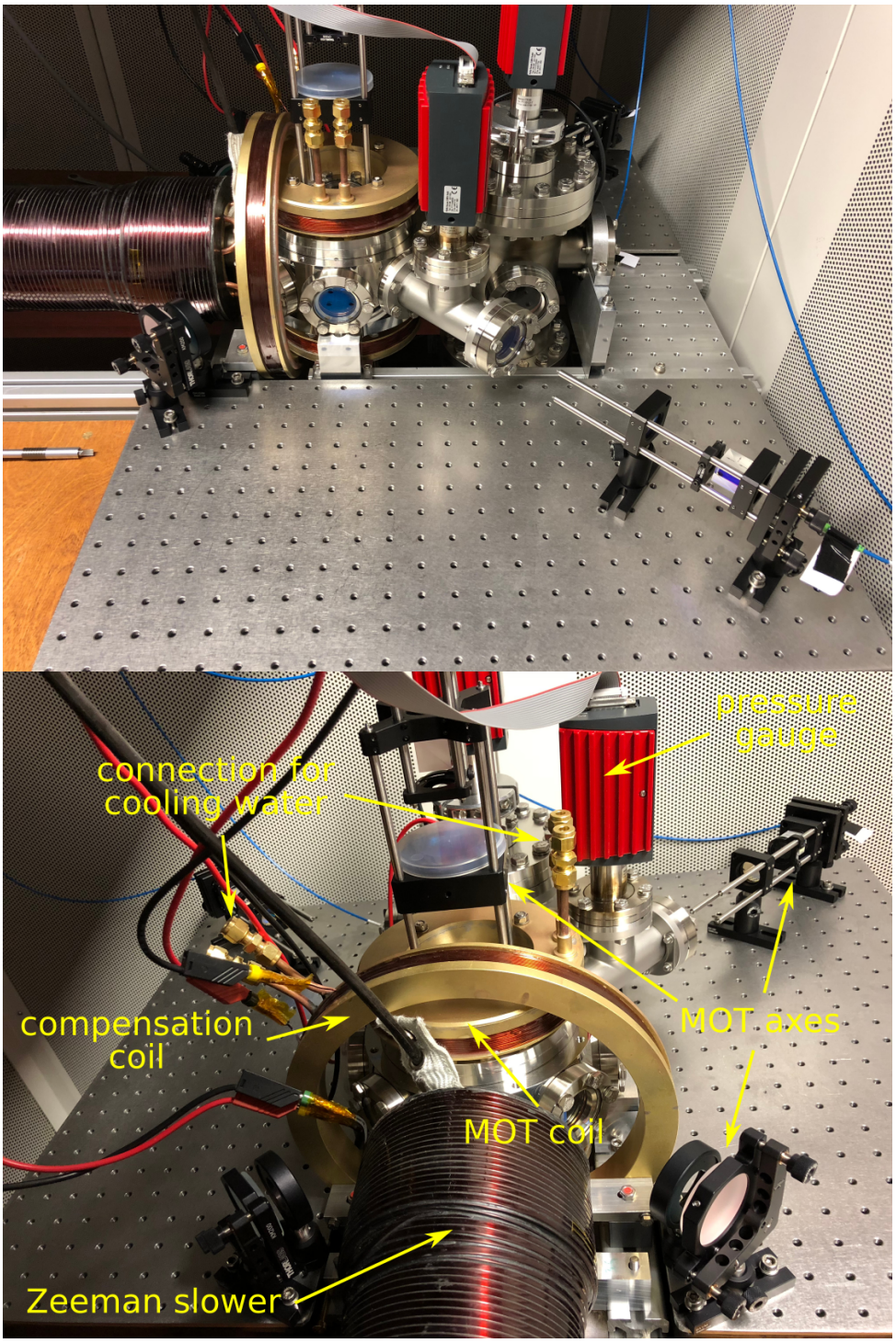

FIGURE 4.26: Setup of the magneto-optical trap. (Top) Side view of the Zeeman slower outlet, the compensation coil and the magneto-optical trap. The vacuum chambers are mounted on an aluminum construction profile (Item Profile 10 50x50) to ensure alignment and enable easy moving along the main axis. (Bottom) Detailed view of the components. The breadboards provide space for the necessary optics. Retro-reflection of the beams simplify the setup and save optical power. A pressure gauge (Pfeiffer ITR 90) is used for monitoring.

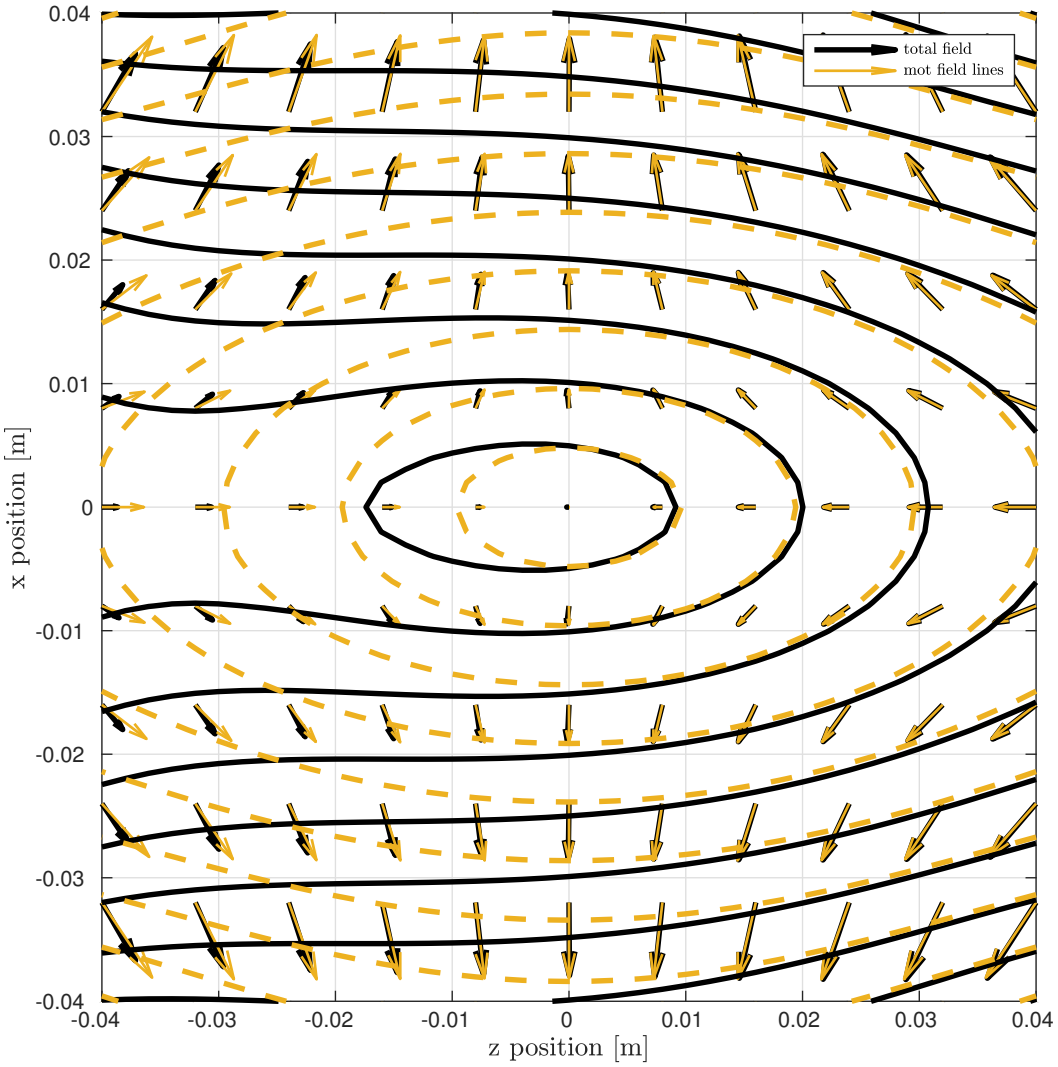

FIGURE 4.27: Field lines in the magneto-optical trap. The z-direction is along the atom beam and the x-direction is the vertical direction along the axis of the magneto-optical trap coils. The ideal field of the trap coils is shown as dashed lines and the total field is shifted slightly due to the high field at the exit of the Zeeman slower which is not compensated completely by the compensation coil. A zero-crossing still occurs at the center of the trap. The direction of the magnetic field is shown as vectors and the symmetry yields a gradient twice as large in axial direction compared to radial direction.

for this because it only requires replugging of a few fibers to change from argon to krypton.

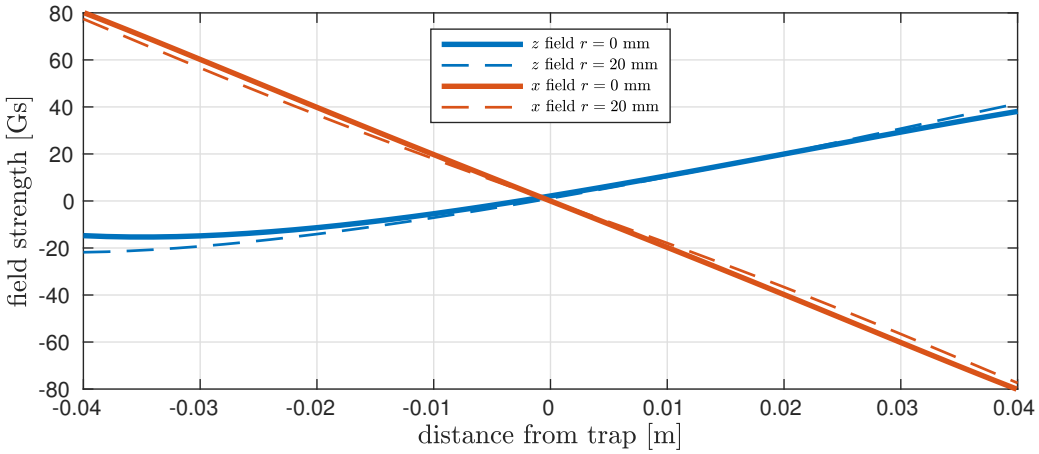

FIGURE 4.28: Magnetic field in the magneto-optical trap. The Maxwell coil configuration yields a magnetic field twice as strong in axial direction than in radial direction. The field is slightly shifted from an ideal magneto-optical trap field due to the high magnetic field at the exit of the Zeeman slower.

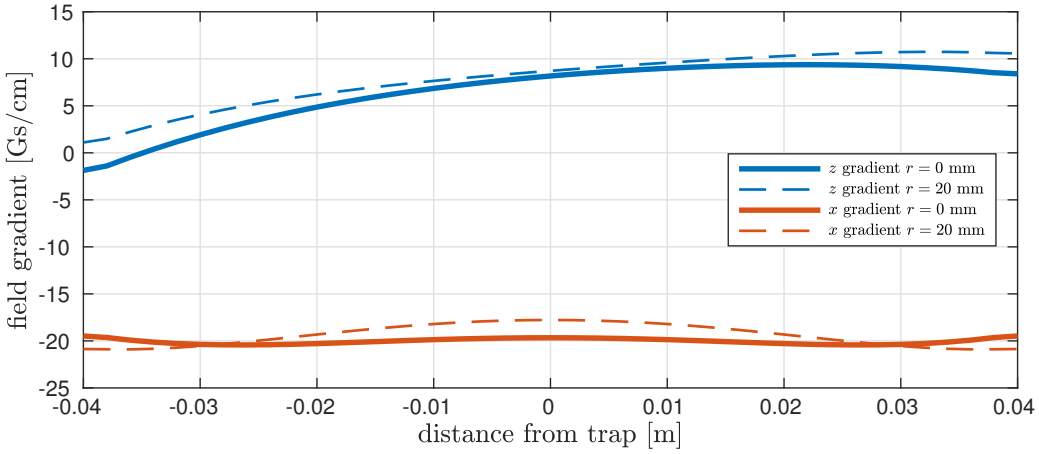

FIGURE 4.29: Field gradient in the magneto-optical trap. The field gradient and red detuning of the laser light are the parameters to control the size and trapping velocities of the magneto-optical trap. Gradients of 20 $\frac{\mathrm{G}}{\mathrm{cm}}$ and $\sim$ 10 $\frac{\mathrm{G}}{\mathrm{cm}}$ are chosen for the axial and radial direction respectively.

FIGURE 4.30: Photo of the progress in the laboratory container. Within a year, the laser system, vacuum setup and atomic optical components have been set up to the state that it was possible to capture ^{40}Ar and ^{84}Kr isotopes.

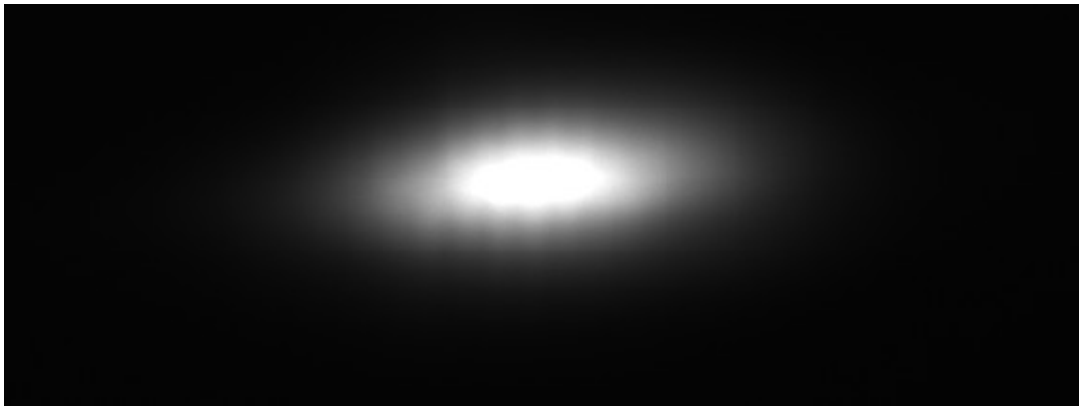

FIGURE 4.31: Captured atoms in the magneto-optical trap. The atoms scatter the light of the laser beams and this can be used for fluorescence imaging. The 1 : 1 telescope projects the magneto-optical trap to a charged-coupled device (CCD) camera. The new apparatus in the laboratory container has been operated with argon (^{40}Ar) and krypton (^{84}Kr). The image shows the first magneto-optical trap with ^{84}Kr in the container.

Part III

Possible Improvements on the Counting Efficiency

Chapter 5

Setup for the Optimization of the Metastable Source

The current status of Argon Trap Trace Analysis has opened the door to different environmental physics research fields. Pilot studies have been performed on groundwater (Ritterbusch et al., 2014), ocean ventilation (Ebser et al., 2018) and most recently glacier ice (Feng et al., 2018). Although the efficiency of the setup has been sufficient for these projects, a higher atom counting rate in the magneto-optical trap would lead to an overall improvement by reducing the required measurement time or decreasing statistical uncertainties. The inefficiency in the excitation of the noble gas inside the metastable source and the low efficiency to collect and cool the excited metastable atoms are the main reasons for the low counting rate. Less than 10^{-4} atoms are excited to the desired state (Welte, 2011) and only about a factor of 10^{-1} of these can be collected by the transverse cooling (Ritterbusch, 2014). A better understanding of the plasma source is the basis for an improvement of these issues and demands for a dedicated test apparatus.

This test setup has been built in the scope of this work and is described in the following. Additionally, a precollimation scheme is presented to increase the number of atoms in the capture range of the first transverse cooling, i.e. the collimator with the tilted mirror design.

5.1 Setup of the Apparatus

The test apparatus mainly uses vacuum components from a previous experiment that have become available for this purpose. It has been modified to fit the requirements of a dedicated source test apparatus. This includes a certain mobility of the whole setup and automatization to efficiently pump the vacuum after a source change. Figure 5.1 shows the setup that has been built on a movable frame with the electric control box and optical system attached to it.

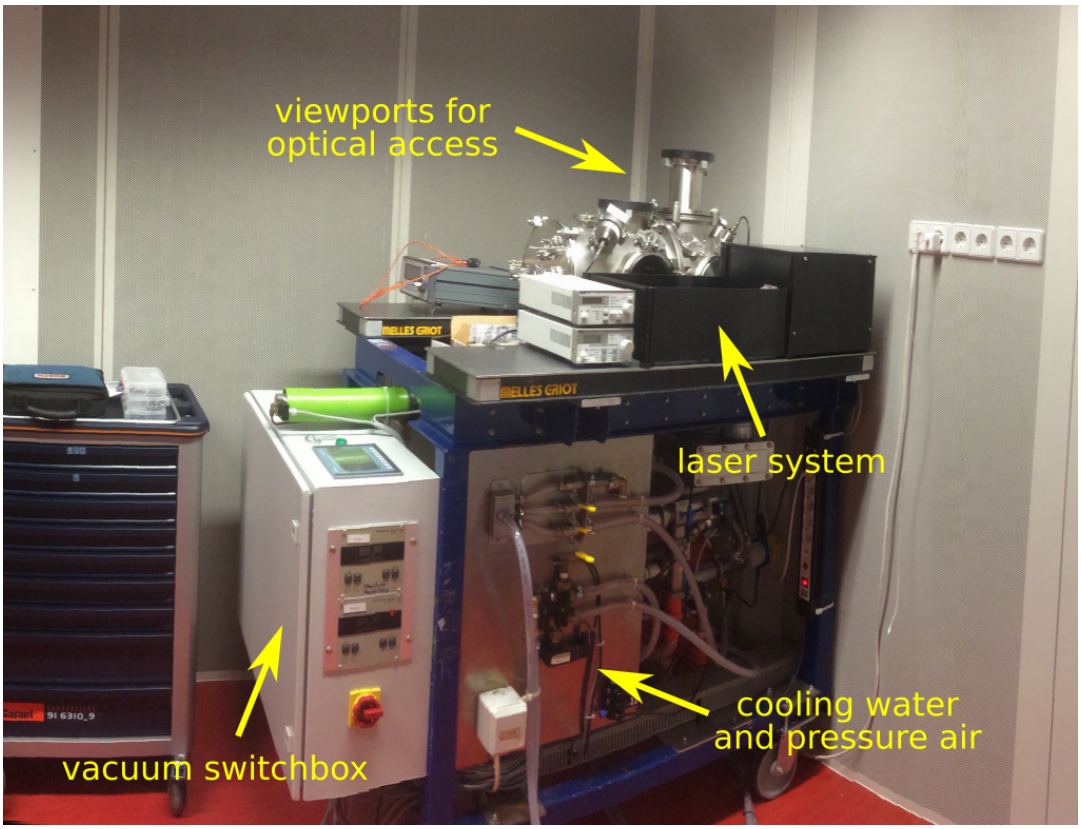

FIGURE 5.1: Picture of the apparatus for the source optimization. The vacuum components are mounted on a movable steel frame and the pumps and vacuum valves are controlled by a switching box. The optical setup is mounted on breadboards attached to both sides of the apparatus. It includes an external-cavity diode laser providing the required light for spectroscopic measurements, a spectroscopy cell and a Fabry-Pérot-Interferometer (FPI) for absolute and relative frequency referencing, respectively. The required power, cooling water and compressed air are provided externally and are distributed to the several components.

5.1.1 Vacuum System

The vacuum system of the test setup has been reduced to the first two chambers in a DN 250 KF tube. They are connected by an aperture of 20 mm diameter and provide optical access via window ports at the side and at the top. The source flange has the same size as the prototype apparatus (Welte, 2011) and the current source design has been installed without any modifications.

Figure 5.2 shows the schematic of the vacuum system. The apparatus is evacuated by oil diffusion pumps mounted below each of the two chamber. They have a large pumping power and provide high vacuum in a short time span compared to turbo-molecular pumps. Although the huge drawback of oil in the vacuum excluded this type of pumps in most applications and had them replaced by oil-free turbo-molecular pumps of appropriate size, they are suited for the purpose of the source test apparatus. The fore vacuum is generated by a rotary vane pump and

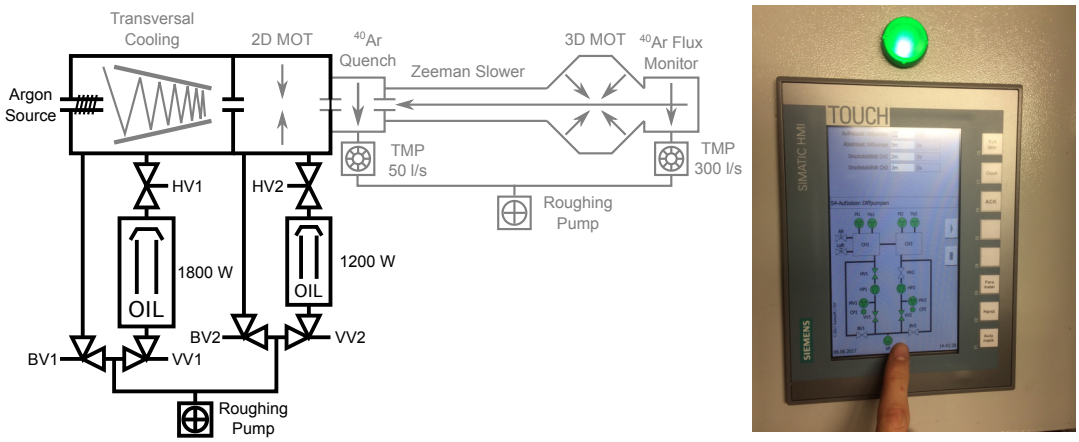

FIGURE 5.2: (left) Schematic of the vacuum system. The components with solid lines represent the current status and the transparent components are possible future upgrades, such that a full atom counting apparatus can be built around the existing setup. The oil diffusion pump and vacuum valves HV, BV and VV for both chambers 1 and 2 can be controlled by the switching box. The pressure is monitored by gauges which indicate if the respective pumps and valves are usable. (right) Touch panel for user input and output. A Siemens Simatic SPS is deployed for controlling the vacuum pumps and valves. The diagram shows the current state of the apparatus and an automatic start up program has been implemented.

switching valves are deployed to evacuate either the chambers directly or the output of the oil diffusion pumps.

Great care has to be taken considering safety and proper handling of oil diffusion pumps. The high temperature requires operating pressures below $\sim 10^{-2}$ mbar and a safety valve has been installed to close the pumps in case of vacuum breakdown or leaking components. The control system, i.e. switching box, has been built by our electrical workshop and deploys a Siemens Simatic SPS with a touch panel for user input and output. The system has been programmed to prevent any faulty operation by the user.

Additionally, an autonomous starting procedure for the vacuum is included and follows the start up and control steps listed below:

1. turn on rotary vane pump
2. alternate the switching valves between chambers and fore vacuum
3. check pressure
4. check cooling water
5. turn on oil diffusion pump if pressures are low enough

6. wait for 30 minutes until the oil diffusion pumps are warmed up
7. open valves of oil diffusion pump

The control system checks the pressure gauges and cooling water flow monitors at any time during operation and jumps back to the respective point if they are not within the accepted range. The current status of operation is shown on the touch panel.

5.1.2 Optical Setup

A convenient way to characterize the metastable atoms is by laser spectroscopy of the $1s_5 \rightarrow 2p_9$ transition. This gives not only the density of metastable atoms but also their velocity distribution. A home-built external-cavity diode laser provides the required 812 nm light for the transition. A Doppler-free saturation spectroscopy in a reference cell and a Fabry-Pérot Interferometer are deployed as absolute and relative frequency scale respectively. A detailed scheme can be found in Appendix C and more information is available in Hahne, 2017.

The direction transverse to the atomic flow can be analyzed via absorption spectroscopy with a photodiode on the opposite site of the chamber. This yields a distribution in velocity space but no spatial information of the atoms.

The direction longitudinal to the atomic flow can be analyzed by detection of the fluorescence of the scattering atoms. The low signal is resolved by a lock-in amplifier thus modulating the light with a frequency far higher than the scanning frequency of the laser.

The whole optical setup is built on breadboards connected to the frame holding the vacuum chamber and enables mobility of the test apparatus.

5.2 Source Characterization

The metastable atom source can be characterized by laser spectroscopy and the velocity dependent atom flux emerging from the source has been analyzed.

5.2.1 Strong Saturation Spectroscopy

The change of the intensity of light through a medium with atomic density n is described by

$$\frac{dI}{dz} = -\hbar\omega\gamma_P n \tag{5.1}$$

with scattering rate $\gamma_P = \frac{\gamma}{2}\frac{s_0}{1+s_0+4\frac{\delta^2}{\gamma^2}}$, light detuning from atomic resonance δ, saturation parameter $s_0 = \frac{I}{I_S}$ and scattering cross section $\sigma_0 = \frac{\hbar\omega}{2I_S}$. It can be interpreted as the number of scattered photons with energy $\hbar\omega$ per area, per time and for a distance z thus the loss of intensity per distance.

Inserting and rearranging terms leads to

$$dI = -n \cdot \frac{\hbar\omega\gamma}{2I_S} \cdot \frac{I}{1+\frac{I}{I_S}+4\frac{\delta^2}{\gamma^2}}dz = -n\sigma_0 \cdot \frac{I}{1+\frac{I}{I_S}+4\frac{\delta^2}{\gamma^2}}dz \tag{5.2}$$

and by the integration of this expression over the length L and using the initial and final intensities I_i and I_f, it leads to the optical depth

$$n\sigma_0 L = \int_0^L n\sigma_0 dz = \int_{I_i}^{I_f} \frac{1+\frac{I}{I_S}+4\frac{\delta^2}{\gamma^2}}{I}dI = \frac{I_\mathrm{i}-I_\mathrm{f}}{I_S} - (4\frac{\delta^2}{\gamma^2}+1)\ln\frac{I_\mathrm{f}}{I_\mathrm{i}}. \tag{5.3}$$

For the case of resonant light with $\delta = 0$, this yields

$$n\sigma_0 L = \frac{I_\mathrm{i}}{I_S}(1-\frac{I_\mathrm{f}}{I_\mathrm{i}}) - \ln\frac{I_\mathrm{f}}{I_\mathrm{i}}. \tag{5.4}$$

The result is only dependent on the optical intensity I_i and the relative absorption $\frac{I_\mathrm{f}}{I_\mathrm{i}}$ that can be measured by saturation spectroscopy.

5.2.2 Flux of Metastable Atoms

Figure 5.3 shows a schematic view of the metastable source and the transverse and longitudinal spectroscopy laser. The atom flux that emerges from the metastable source can be calculated by

$$j = \frac{N}{tA} = \frac{Nw}{tAw} = \frac{N}{V}\cdot\frac{w}{t} = n\cdot v_\mathrm{long}. \tag{5.5}$$

It is only dependent on the density n that can be calculated using the optical depth inferred from transverse saturation spectroscopy.

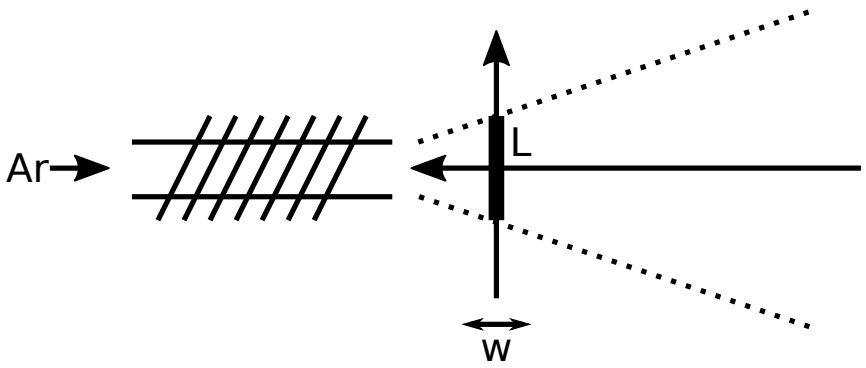

FIGURE 5.3: Schematic view of the source spectroscopy. The transverse laser beam passes the atom through a distance L and has width w. The longitudinal laser beam scatters light and can be detected. A lock-in amplifier is deployed to increase the signal-to-noise ratio.

The longitudinal velocity distribution v_{long} can be measured by a fluorescence spectroscopy of a beam anti-parallel to the atomic beam. The signal-to-noise ratio is increased by deploying a lock-in amplifier.

Reference Spectroscopy

A reference spectroscopy is necessary for gauging the relative and absolute value, i.e. the atomic resonance, of the scan. The absolute value is given by a Doppler-free saturation spectroscopy which is performed in a plasma cell. The relative detuning can be measured by a resonator with known free spectral range of $\Delta\nu_{\text{FSR}} \approx 130\,\text{MHz}$ (Feng, 2012). Figure 5.4 shows the acquired signal of the spectroscopy.

The required peaks can be detected by the evaluation routine. More details on the spectroscopy setup can be found in Hahne, 2017.

Velocity Distributions after the Source

A simple model for the velocity distribution after the source is given by three independent Gaussian distributions

$$p_i(v_i) = \frac{1}{\sigma\sqrt{2\pi}} \cdot e^{-\frac{1}{2}\frac{(x-\mu)^2}{\sigma^2}} \tag{5.6}$$

where $\mu = 0$ is the mean velocity and $\sigma = \sqrt{\frac{k_B T}{m}}$ is the standard deviation. This is the case for the transverse spectroscopy and the acquired signal shows the Doppler broadening of the atoms.

Figure 5.5 shows the raw signal of the transverse spectroscopy of the source. The effect of liquid nitrogen cooling reduces the transverse velocities and thus the full

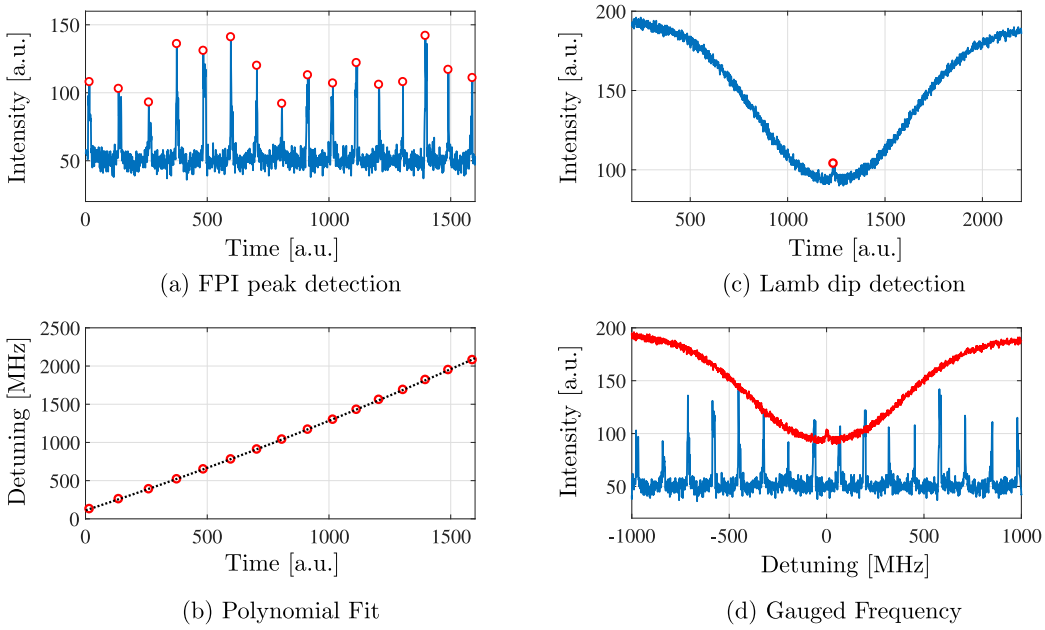

(a) FPI peak detection (c) Lamb dip detection

(b) Polynomial Fit (d) Gauged Frequency

FIGURE 5.4: Signal processing of the reference spectroscopy. (a) A Fabry-Pérot Interferometer (FPI) resonator with a known free spectral range of $\Delta\nu_{\mathrm{FSR}} \approx 130$ MHz is deployed as a relative frequency scale. (b) The peaks of the interferometer with fixed distances in frequency space are mapped to the time domain. The scan of the laser is not necessarily translated into a linear frequency sweep so that a polynomial is fitted to the signal. (c) The absolute value of the frequency can be inferred from the Lamb dip of a Doppler-free saturation spectroscopy. (d) The finished frequency gauge of the laser light. Taken from Hahne, 2017.

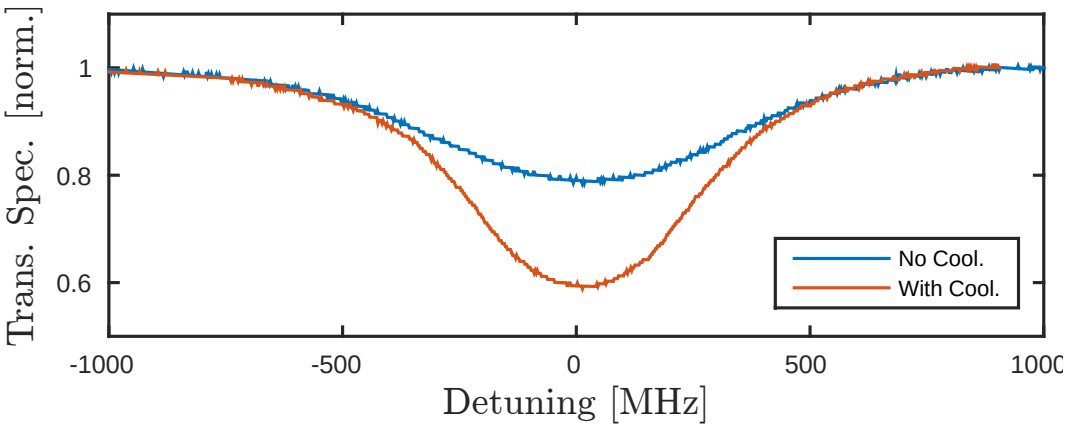

FIGURE 5.5: Raw signal of the transverse spectroscopy. The signal has the expected Gaussian shape due to the motion of the atoms. Liquid nitrogen cooling leads to a reduction of the velocities thus the full width half maximum decreases from 455 MHz to 375 MHz. The high absorption can be explained by the reduction of the longitudinal velocity which leads to longer interaction times with the transverse spectroscopy laser.

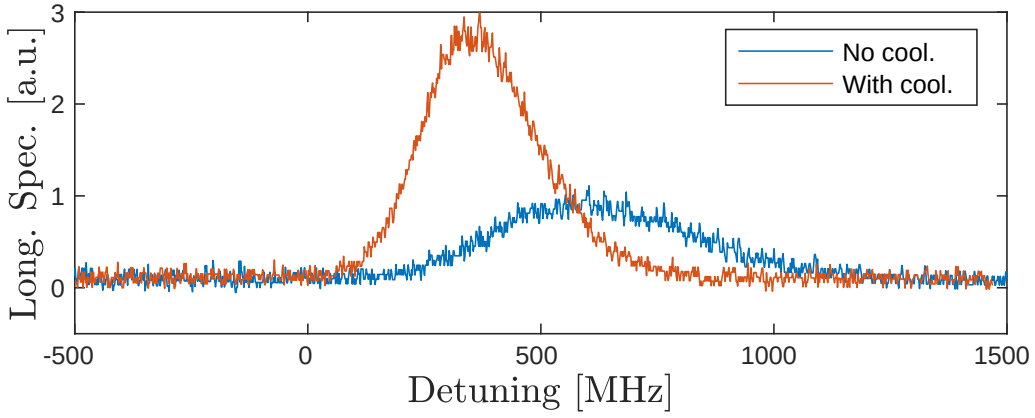

FIGURE 5.6: Raw signal of the longitudinal spectroscopy. The setup probes the absolute velocities of the atoms and the signal thus follows a Maxwell-Boltzmann distribution. The liquid nitrogen cooling reduces the most probable resonance from $\sim$ 530 MHz to $\sim$ 355 MHz. The higher signal intensity is due to the longer interaction times with the spectroscopy laser in the fluorescence detection region.

width half maximum of the signal from 455 MHz to 375 MHz. The higher absorption is due to simultaneous reduction of the longitudinal velocities which leads to a longer interaction time with the spectroscopy laser.

The absolute value v of the velocity in three dimensions can then be calculated by integration in spherical coordinates. This leads to

$$\int_V p(v_x)p(v_y)p(v_z)dxdydz = (\frac{m}{2\pi k_B T})^{\frac{3}{2}} \cdot \int_0^v \int_0^\pi \int_0^{2\pi} e^{-\frac{m}{2k_B T}v^2} v^2 \sin\theta dv d\theta d\phi \quad (5.7)$$

where the square of the absolute velocity $v^2 = v_x^2 + v_y^2 + v_z^2$ is used. The probability to find an atom with a velocity in an interval $[v, v+dv]$ is then

$$p(v)dv = (\frac{m}{2\pi k_B T})^{\frac{3}{2}} \cdot 4\pi \int_v^{v+dv} e^{-\frac{m}{2k_B T}v^2} v^2 dv = \sqrt{16\pi}\frac{v^2}{\hat{v}^2} e^{-\frac{v^2}{\hat{v}^2}} dv. \quad (5.8)$$

This is a Maxwell-Boltzmann distribution with the most probable velocity $\hat{v} = \sqrt{\frac{m}{2k_B T}}$ which applies to the longitudinal spectroscopy.

Figure 5.6 shows the raw signal of the longitudinal fluorescence spectroscopy. The effect of liquid nitrogen cooling reduces the most probable velocities and the highest signals have been measured at detunings of $\sim$ 530 MHz and $\sim$ 355 MHz. The lower velocities in the cooled case lead to a longer interaction time and higher fluorescence signals.

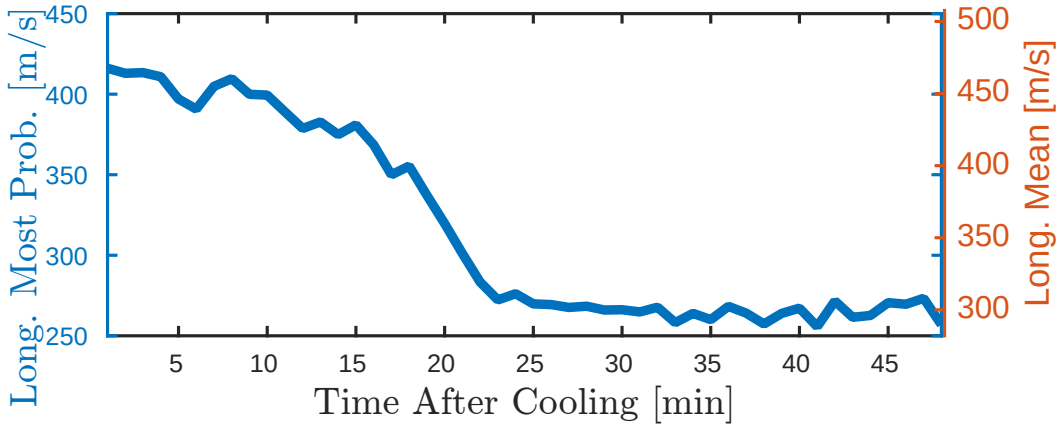

FIGURE 5.7: Longitudinal velocity with liquid nitrogen cooling. The Maxwell-Boltzmann fit of the raw data yields the most probable velocity as a parameter. The liquid nitrogen cooling of the effusive source reduces the most probable velocity from 420 $\frac{m}{s}$ to 260 $\frac{m}{s}$. It scales linearly by a factor of 1.128 with the mean velocity.

5.2.3 Evaluation of the Data

The signals have been taken every two minutes after turning on the liquid nitrogen cooling. Both spectroscopy signals have been fitted with their respective models. The change of height in the longitudinal fluorescence signal is due to a longer scattering time. This is irrelevant for the velocity distribution and the fitted curves can be normalized.

One of the fit parameters gives the most probable velocity in case of the longitudinal spectroscopy and is shown in Figure 5.7. The most probable velocity is around 420 $\frac{m}{s}$ without cooling and reduces to 260 $\frac{m}{s}$ with liquid nitrogen cooling. The mean velocity can be calculated by integrating over all velocities and is 1.128 times higher.

Figure 5.8 shows the column densities of the atoms inferred with the longitudinal velocity according to equation 5.4 and equation 5.5. The width of the distribution is reduced by liquid nitrogen cooling and the absorption signal more narrow around zero velocity.

The overall flux can be calculated by

$$j = \frac{1}{\sigma_0 L} \cdot \int_{-\infty}^{+\infty} \int_{0}^{+\infty} n(v_{\text{trans}}) dv_{\text{trans}} dv_{\text{long}} = \frac{1}{\sigma_0 L} \bar{v}_{\text{long}} \cdot \int_{-\infty}^{+\infty} n(v_{\text{trans}}) dv_{\text{trans}} \quad (5.9)$$

using the transverse velocities v_{trans} and the longitudinal velocities v_{long}. The measured column densities times the longitudinal mean velocity gives the flux for a certain velocity class. The effect of liquid nitrogen cooling is to compress the density distribution towards smaller transverse velocities.

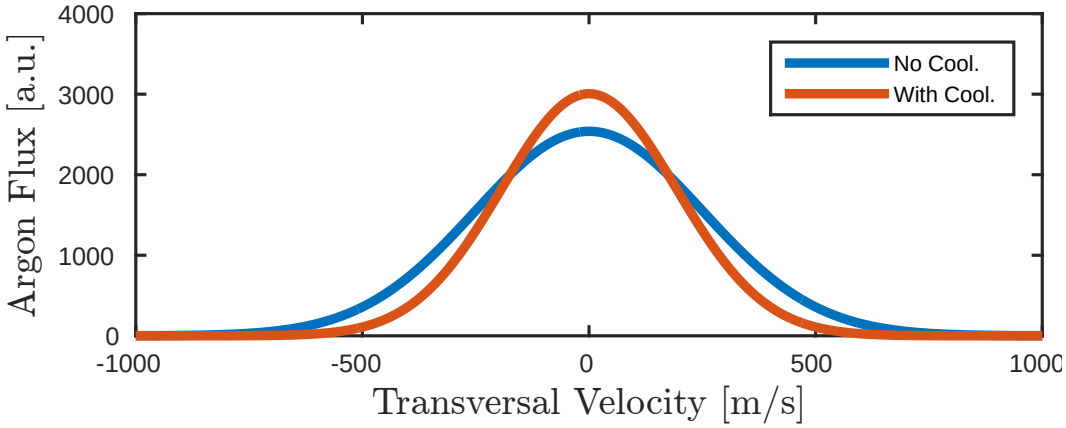

FIGURE 5.8: Velocity dependent column densities after the source. The longitudinal velocities can be used to infer the transverse column density of the atoms after the effusive source. Liquid nitrogen cooling reduces the width of the distribution so that more atoms are within a narrow range around zero velocity.

Figure 5.9 shows the effect of liquid nitrogen cooling on the overall flux and the flux on resonance, i.e. $v_{\text{trans}} = 0$. Although the overall flux, which is given by the second integral in equation 5.9, remains constant, the flux in forward direction with $v_{\text{trans}} = 0\frac{\text{m}}{\text{s}}$ is increasing with liquid nitrogen cooling.

Since not all transverse velocity classes can be captured by the subsequent atomic physics devices, the liquid nitrogen cooling increases the overall efficiency of Argon Trap Trace Analysis. The thermal equilibrium of the current setup is reached far above the temperatures of liquid nitrogen and a better thermal contact of the source can lead to further improvements.

5.3 Precollimation of the Source

The atoms leaving the effusive metastable source have to be collimated to increase the flux into the detection region two and a half meters downstream. The transverse cooling is performed in the collimator using a tilted mirror design to compensate the changing Doppler shift during transverse deceleration of the atoms. The upper transverse capture velocity for atoms with a mean longitudinal velocity of 300 $\frac{\text{m}}{\text{s}}$ is only 30 $\frac{\text{m}}{\text{s}}$ and only $\sim 10^{-1}$ of the metastable atoms can be collimated (Ritterbusch, 2014).

A precollimation of the atoms is thus desirable but hindered by the finite small distance from exit of the source to the entry of the collimator. The commonly used scattering force is saturated at $F_{textsp} = \hbar k \frac{\gamma}{2}$. This sets an upper limit to the atoms

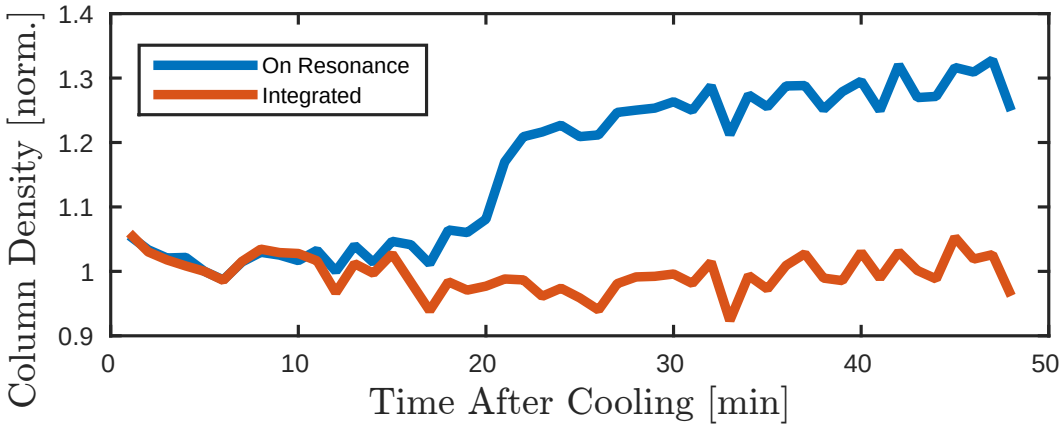

FIGURE 5.9: Atomic flux after the source. The atomic flux over all transverse velocity classes remains constant. The atoms in forward direction, i.e. on resonance are enhanced by the liquid nitrogen cooling. This increases the efficiency of Argon Trap Trace Analysis since the atoms are compressed into the limited capture range of subsequent atom optical devices.

that can be decelerated in the short time before they enter the collimator and the upper part of Figure 5.10 shows trajectories of the atoms in phase space. In a distance of 50 mm, precollimation using the scattering force increases the capture range to $\sim 47\ \frac{\mathrm{m}}{\mathrm{s}}$.

A stronger force is required to increase the flux further and a possible candidate for this purpose is the bichromatic force (Grimm et al., 1990; Ovchinnikov et al., 1993; Söding et al., 1997). Instead of being limited by the scattering rate $\gamma_{textsp} = \frac{\gamma}{2}$, an incoherent process, the bichromatic force deploys rapid coherent excitation and stimulated emission at a Rabi frequency Ω. A detailed theoretical description using a doubly-dressed atom model is given in Appendix B.

The bichromatic force has been demonstrated for ^{40}Ar (Feng et al., 2017) and Figure 5.11 shows the expected dependency on the Rabi frequency, i.e. the optical intensity. A numerical calculation using the optical Bloch equations yields similar results. Compared to the scattering force, the bichromatic force is not saturated and is in principle only limited by the available laser power.

The lower part of Figure 5.10 shows the equation of motion for precollimation by the bichromatic force. In an interaction region of 50 mm, atoms up to transverse velocities of $\sim 70\ \frac{\mathrm{m}}{\mathrm{s}}$ can be decelerated into the capture range of the collimator.

A simulation of the expected flux increase using the achievable bichromatic force and the results of the previous section, i.e. velocities and atom densities emerging from the source, is shown in Figure 5.12. The left part shows a proposed setup for precollimation. Every direction of the bichromatic force has to be pushed separately

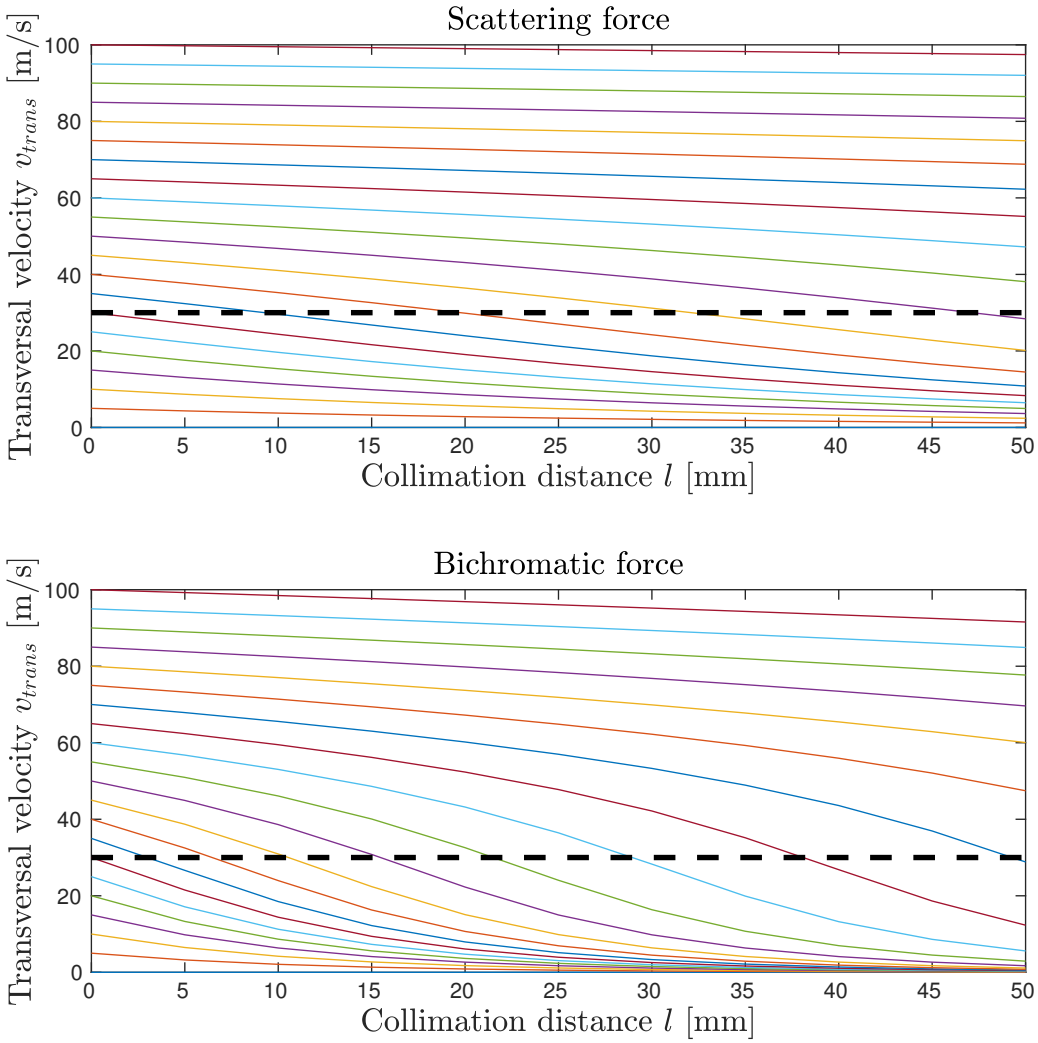

FIGURE 5.10: Equation of motion for precollimation. A detuning of $\delta = -\vec{k} \cdot \vec{v} = 25$ MHz has been used and the capture range of the collimator for mean longitudinal velocities 300 $\frac{\text{m}}{\text{s}}$ is shown as a dashed line at 30 $\frac{\text{m}}{\text{s}}$. (top) The scattering force is capable of capturing atoms with transverse velocities of up to $\sim$ 47 $\frac{\text{m}}{\text{s}}$ into the capture range of the collimator. (bottom) The bichromatic force can bring atoms up to $\sim$ 70 $\frac{\text{m}}{\text{s}}$ into the capture range.

thus doubling the required distance. The stronger force is still superior to the scattering force as can be seen in the right part of Figure 5.12. A flux gain of $\sim$ 1.7 can be achieved by the bichromatic precollimation in one axis yielding an almost threefold gain for both axes.

In general, the optimal parameters have to be optimized for both, precollimation and collimator. This includes the detuning of both devices and the tilting angle of the collimator mirrors. A good prealignement can be achieved using the abundant ^{40}Ar flux signal, but in general, fine adjustments have to be done with ^{39}Ar, preferably using highly enriched samples. The test setup is the optimal platform for such

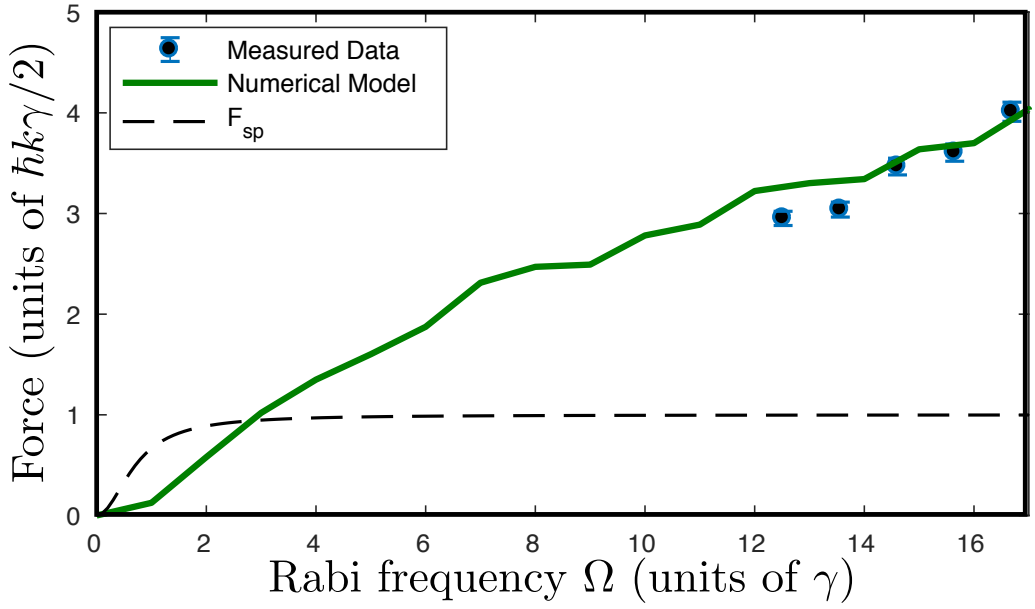

FIGURE 5.11: Dependency of the bichromatic force on the Rabi frequency. The force shows the expected dependency on the Rabi frequency which is proportional to the square-root of the optical intensity. A maximum force of four times the commonly used scattering force has been achieved. The dashed line shows the scattering force which depends on incoherent spontaneous emission processes and which is saturated at higher intensities. The results of numerical calculations using the optical Bloch equations are shown as a solid line and are comparable with the measured data points. Taken from Feng et al., 2017.

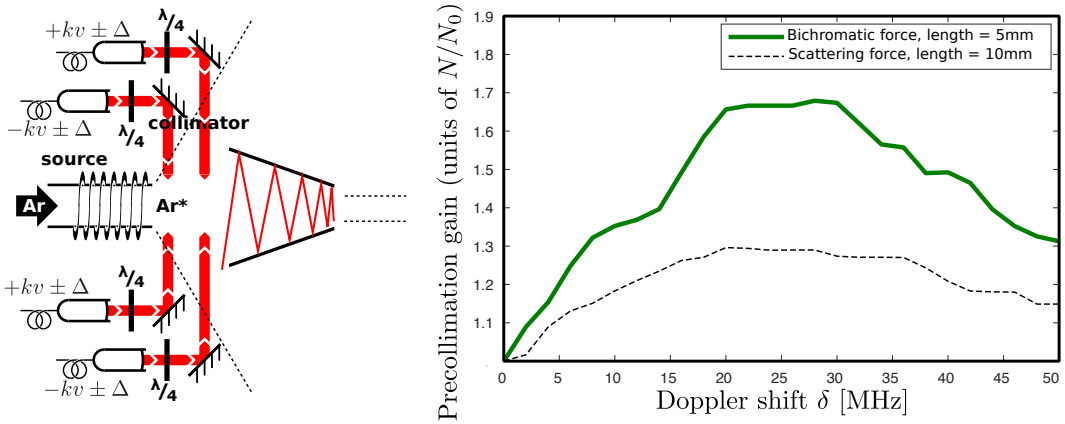

FIGURE 5.12: Proposed setup for a bichromatic precollimation. (left) The bichromatic force is decelerating each direction separately thus doubling the required interaction region. (right) The gain of the atomic flux with a bichromatic precollimator compared to a precollimator deploying the scattering force. For one axis, a gain of ~ 1.7 can be achieved by a bichromatic precollimation. Taken from Feng et al., 2017.

tests since contamination of the vacuum components does not matter.

Chapter 6

Conclusion and Outlook

The work presented in this doctoral thesis has addressed three main topics concerning the research and development of Argon Trap Trace Analysis. The topics are the application to new areas, i.e. glacier ice, the building of a new apparatus in a self-sufficient laboratory container for increasing the sample capacities in the near-future and the set up of a dedicated test apparatus suited for better understanding of the metastable source.

6.1 Application to New Areas: Dating of Glacier Ice

The first topic has been the demonstration of the radio-argon method to a new environmental research field and the dating results of the ice samples is the door-opener for a broader application in glaciology. The samples have demonstrated the feasibility of ^{39}Ar for younger ice with ages of $\sim$ 200 years before present and ice as old as $\sim$ 1000 years before present. The results have provided valuable information on the required degree of decontamination efforts during sampling of the ice blocks in the field. There has been no evidence that the sampling method by chainsaw has led to contamination of the ice by modern air thus atmospheric ^{39}Ar concentration. Therefore, sampling for future campaigns can be as simple as presented here and allows to obtain convenient block sizes of $\sim$ 5 kg.

Furthermore, more insight has been given concerning the processing of the samples in the laboratory. The conservative approach uses the carefully prepared core of each block whereas the optimistic approach combined the removed outer layers of the ice block to another sample. The mutually consistent age of the samples prepared by the two different approaches strongly shows that a minimal effort for out-casting ice even of poorer quality is sufficient for the radio-argon dating thus leading to a larger available sample size.

The successful ice dating using Argon Trap Trace Analysis is the door-opener for so far untapped archives and records, i.e. the valuable information stored in glacier ice of the last millennium. The results encourage further projects and studies on the paleoclimate with the assistance of ^{39}Ar dating. The interpretation of ice layers

or even the dynamics of the ice since around thousand years before present can be inferred using the new method (Feng et al., 2018). The impact of Argon Trap Trace Analysis on glaciology arrived just in time regarding the current warming conditions that will result in losing these ice archives thus the knowledge that can be acquired from them.

6.2 Increasing Sample Capacities: A New Apparatus

The second topic is the setup of a completely new apparatus in a self-sufficient laboratory container thus doubling the sample throughput capacities. The huge demand on radio-argon dating arose by the pilot studies for groundwater, ocean and ice (Ritterbusch et al., 2014; Ebser et al., 2018; Feng et al., 2018). The results of these studies have demonstrated that Argon Trap Trace Analysis is feasible for these environmental reservoirs and the method is on the verge of becoming the state-of-the-art technique for ^{39}Ar measurements. This is especially of importance for oceanography and glaciology, where sample size is limited due to logistic reasons or required spatial resolution.

The project of a second beamline started long before the first device entered the laboratory container. It is funded by the German Research Foundation in a program for new devices for science and careful cost calculation and planning have been done for the proposal. After the delivery of the customized container, the empty space inside has been filled with the realized devices that have been only on sketch at that point. Basic infrastructure and equipment, optical components, vacuum chamber and atom optical devices have been set up within a year.

The key to success has been proper project management since several different parties have been involved in the setup of the container. This includes mostly the mechanical workshop, the electrical workshop, companies delivering necessary components and devices, the scientific staff and also the building authority. All time scales and delivery times have been considered and the sub-projects have been scheduled accordingly.

The result of the careful preparations was the first successful trapping of argon and krypton atoms with the new setup. This was a huge milestone and has demonstrated that the components, i.e. laser, vacuum and magnetic fields, are working properly, at least for the purpose of trapping atoms.

The next step is the change of the isotopic species from the abundant ^{40}Ar to the rare ^{39}Ar. On the apparatus side, the preparation of the required single atom detection has been already done as the imaging system inside the magneto-optical trap

has been optimized for maximum numerical aperture thus high photon signals. The first transverse cooling stage is already prepared and will increase the flux into the detection region. A tool for flux and beam monitoring has to be included for proper alignment and adjustment. On the optical side, the required three sideband frequencies for optical repumping have to be added to the cooling and trapping light. This is done by offset-locking and further frequency shifting of the existing light.

Further developments aim for including krypton or even a hybrid argon-krypton apparatus. The latter can become feasible by the relative high abundance of the krypton isotopes compared to argon thus the devices can operate on a suboptimal setting for krypton.

6.3 Improving the Counting Efficiency: A Test Setup

The third topic is the further improvement of the atomic physics methods that ultimately aim for a higher count rate for ^{39}Ar. In contrast to the krypton isotopes, where the relative abundance thus count rate is three orders of magnitude higher, the low counting efficiency is the limiting factor for argon. The two largest losses happen at the excitation to the metastable state with efficiency of $\sim 10^{-4}$ (Welte, 2011) and the subsequent collimation of the fast atoms that leave the source with efficiency of $\sim 10^{-1}$ (Ritterbusch et al., 2014). Both points yield huge potential for improvements and can be investigated further by the setup of a dedicated source test apparatus.

The test apparatus, Optimizing Trap Trace Analysis, is designed for frequent vacuum breaking to change the components. The two oil diffusion pumps can maintain pressures of $\sim 10^{-6}$ mbar. The required vacuum can ramp up from atmospheric pressure automatically by the controlling system. The detection system is capable of measuring the metastable flux by longitudinal and transverse spectroscopy of the emerging atoms from the source.

The fact that Argon Trap Trace Analysis is already capable of analyzing environmental samples up to a certain precision has shifted the focus of recent activities to conquer new environmental reservoirs. Following up the performed pilot studies, it is the perfect time for further improvements of the technique and the source test apparatus offers a convenient platform to characterize and improve the source as well as test new and stronger laser cooling mechanisms (Feng et al., 2017) for the precollimation of the atoms.

The most obvious effect of a higher counting rate is the reduction of measurement time for the same statistical errors. This directly leads to a higher sample

throughput or better resolution of the measurements. Besides a pure reduction of required measurement time, the effect of cross-sample contamination can be reduced as this increases quadratically with time whereas a higher count rate yields a linear improvement.

6.4 Future Developments of Argon Trap Trace Analysis

The future of dating with Atom Trap Trace Analysis can be best predicted by recognizing the remarkable similarities of the developments so far with the history of radio-carbon dating with ^{14}C. The latter had been first introduced as age tracer by using low-level decay counting on samples of known ages (Arnold and Libby, 1949; Libby, Anderson, and Arnold, 1949). This method has been the state-of-the art for the following three decades although the low radio-activity required sample sizes in the range of grams (Anderson and Libby, 1957). The revolution of radio-carbon dating had started by the introduction of Accelerated Mass Spectrometry to ^{14}C which reduced sample size requirements by nearly three orders of magnitude down to milligrams of carbon (Woelfli et al., 1983; Bonani et al., 1986). This opened new study sites and environmental systems such as ocean water that had been excluded due to sample size requirements (Schlosser et al., 1987). The final innovation has begun by the availability of more and more scientific but also commercial Accelerated Mass Spectrometry facilities dedicated to radio-carbon dating (Kromer et al., 2013) and development of routine equipment and devices (Wacker et al., 2010). The state-of-the-art today are more than a hundred facilities world-wide (Buchholz, 2009; http://www.radiocarbon.org, 2018) offering a commercial and standardized dating service for 350 $ (http://www.leibniz.uni-kiel.de, 2018).

Compared to the successful story of radio-carbon dating, the application of Atom Trap Trace Analysis for dating with the argon and krypton radionuclides can have the same impact as the introduction of Accelerated Mass Spectrometry for ^{14}C. The general feasibility has been demonstrated by pilot studies of groundwater (Sturchio et al., 2004; Ritterbusch et al., 2014), ocean water (Ebser et al., 2018) and glacier ice (Buizert et al., 2014; Feng et al., 2018). Scientific research on further improvements of precision and efficiency will extend the user community, but the current state of the method is already capable of addressing certain geological and environmental physics questions. There is already a high scientific demand on radio-argon dating in hydrology, oceanography and glaciology that yield hundreds of world-wide samples every year.

Beyond that, non-scientific communities such as waterworks and mineral water companies are interested in the age of their water to guarantee quality and purity. Radio-krypton dating especially with ^{85}Kr for groundwater in the young regime

has a high regional interest as it uncovers pollution due to agriculture and chemical companies (LUBW, 1992). The existing three scientific laboratories that are capable of sample preparation and subsequent Atom Trap Trace Analysis are not enough to provide capacities for the upcoming demand. Thus more facilities are feasible in the near future to provide general access to this unique dating method at affordable cost.

Appendix A

Supplementary Data for the Ice Project

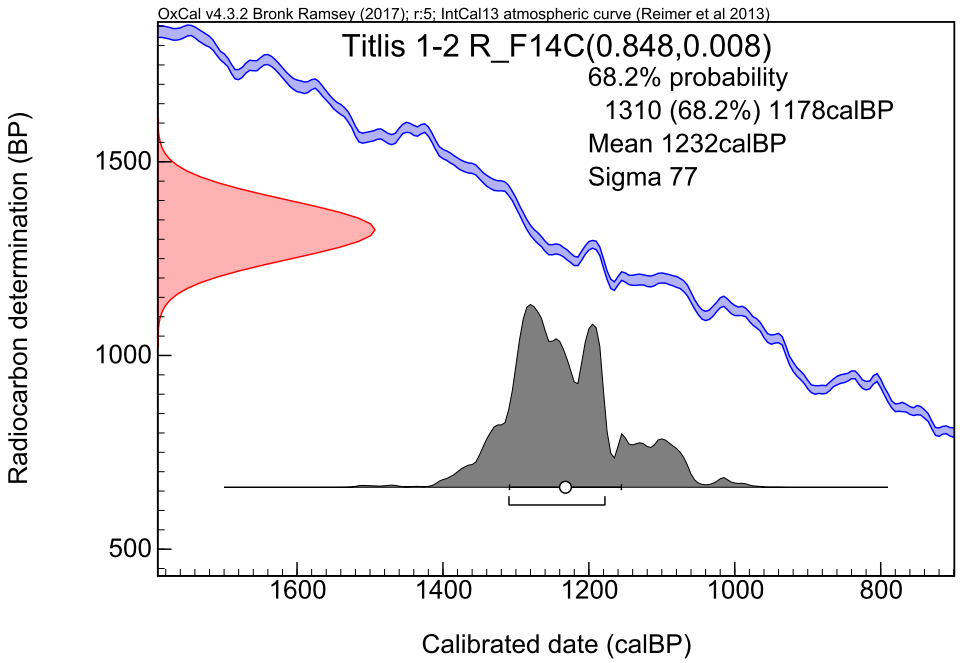

FIGURE A.1: ^{14}C calibration curve of block 1-2 from Titlis glacier cave. The analysis has been performed on microscopic particulate organic carbon. The most probable age range is 1246 – 1378 years before 2018 CE (Hoffmann, 2016).

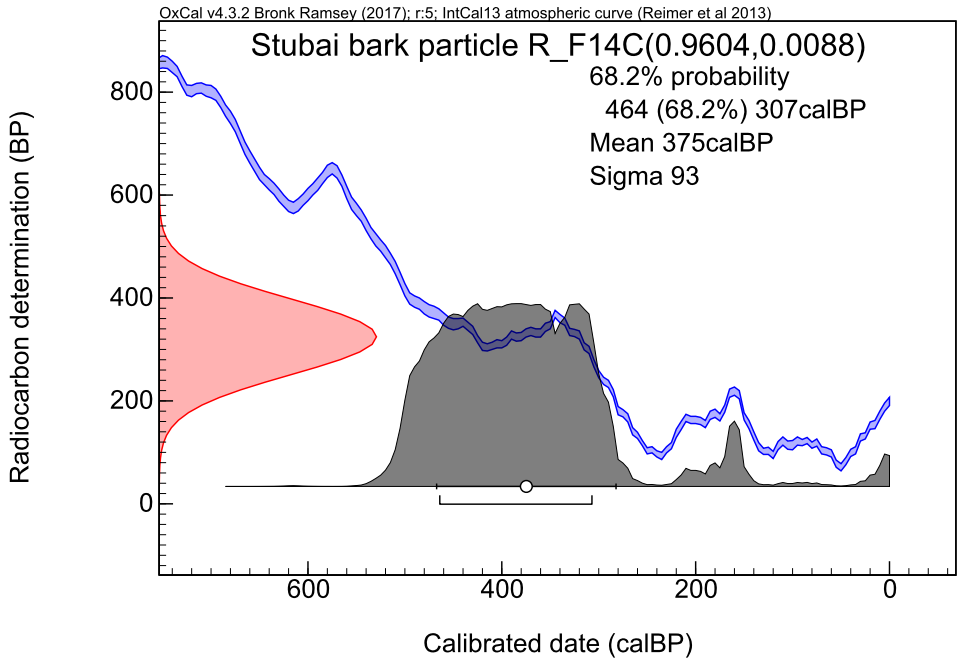

FIGURE A.2: ^{14}C calibration curve of the bark findings in Schaufelferner glacier cave. The most probable age range is $375 - 532$ years before 2018 CE with 68% probability. (Hoffmann, 2016)

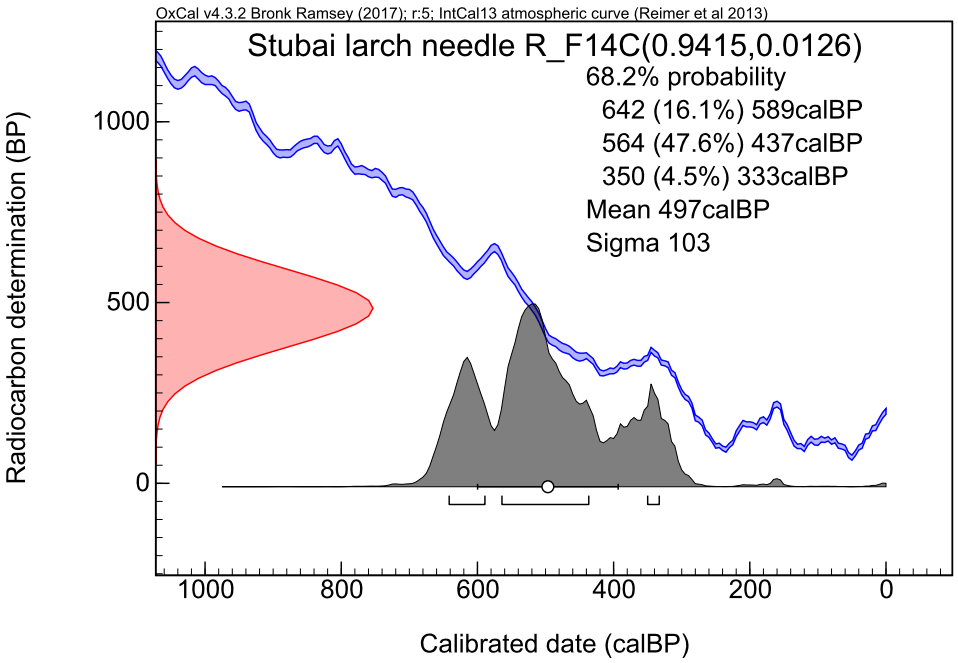

FIGURE A.3: ^{14}C calibration curve of the needle findings in Schaufelferner glacier cave. The most probable age range is $505 - 632$ years before 2018 CE with 48% probability. (Hoffmann, 2016)

TABLE A.1: Overview of ArTTA measurements during ice project. The reported concentrations are the most probable values and the 1σ confidence interval is given. Several measurements are grouped together and use the mean of the included references. The highly enriched references and samples measured in throughput configuration do not suffer from significant background contribution. Before each sample analysis, the apparatus was flushed for 2 hours with krypton. Independent measurements have confirmed that with that procedure the cross sample contamination is minimized.

date	sample	concentration	atoms	bg	T [h]	V [mL STP]
04/17/18	10x enriched	–	94	-	1.83	1.9
04/17/18	10x enriched	–	181	-	3.16	2.1
04/17/18	bottle argon	$108.7^{+14.1}_{-12.8}$	83	-	13.16	throughput
04/18/18	10x enriched	–	109	-	2.00	2.0
04/18/18	Schaufelferner A	$60.8^{+8.9}_{-8.0}$	92	13	22.30	1.7
04/19/18	10x enriched	–	125	-	2.16	1.4
04/24/18	10x enriched	–	94	-	2.16	1.6
04/24/18	dead	–	11	-	15.65	1.2
04/25/18	10x enriched	–	85	-	2.00	2.1
04/25/18	10x enriched	–	118	-	2.50	1.5
04/25/18	dead	–	16	-	19.99	1.5
04/26/18	10x enriched	–	107	-	2.00	1.5
04/26/18	Schaufelferner B	$60.0^{+10.1}_{-9.1}$	66	10	19.50	1.4
04/27/18	10x enriched	–	87	-	2.00	1.5
04/30/18	10x enriched	–	109	-	2.00	1.4
05/01/18	10x enriched	–	121	-	2.00	1.4
05/01/18	bottle argon	$122.0^{+14.4}_{-13.2}$	102	-	14.66	throughput
05/02/18	10x enriched	–	132	-	2.00	1.4
05/02/18	dead	–	10	-	20.00	1.1
05/03/18	10x enriched	–	101	-	2.00	1.5
05/03/18	Entensee	$17.0^{+5.8}_{-5.2}$	33	14	20.00	1.3
05/04/18	10x enriched	–	101	-	2.33	1.3
05/06/18	10x enriched	–	98	-	2.16	0.5
05/06/18	Titlis 1-1	$25.7^{+9.2}_{-8.5}$	50	26	20.00	0.5
05/07/18	10x enriched	–	96	-	2.00	0.5
05/07/18	dead	–	21	-	20.00	0.5
05/08/18	10x enriched	–	91	-	2.00	0.5
05/08/18	Titlis 1-2	$5.5^{+5.6}_{-5.3}$	31	25	20.00	0.6
05/06/18	10x enriched	–	85	-	2.00	0.5

Appendix B

Theoretical Description of the Bichromatic Force

The bichromatic force appear in two overlapping standing waves of laser beams with frequencies red- and blue detuned by $\pm\Delta$ from the resonance ω_0 of the atom. The relative phase ϕ and Rabi frequency Ω of the two light fields can be used to control the intensity and direction of the force (Metcalf and Straten, 1999).

The quantum mechanical description includes the two fields by the states $|b,r\rangle$, where b and r are the number photons in the respective blue and red detuned fields. The total product state with the bare atom states $|g\rangle$ and $|e\rangle$ is then

$$|g,b,r\rangle = |g\rangle \otimes |b,r\rangle \text{ and } |e,b,r\rangle = |e\rangle \otimes |b,r\rangle \tag{B.1}$$

and by conservation of the total photon number $n = b + r$, this forms an ladder of states with eigenenergies

$$E_{e,b,r} = b \cdot \hbar(\omega_0 + \Delta) + r \cdot \hbar(\omega_0 - \Delta) + \hbar\omega_0 = E_{g,b,r} + \hbar\omega_0 \tag{B.2}$$

with level spacing of $\mathrm{d}E = 2\hbar\Delta$.

The system can be described by the Hamiltonian

$$\hat{H}_{NC} = \hbar\omega_A|e\rangle\langle e| + \hbar(\omega_A + \Delta)\hat{a}_b^\dagger\hat{a}_b + \hbar(\omega_A - \Delta)\hat{a}_r^\dagger\hat{a}_r \tag{B.3}$$

with the photon creation and annihilation operators $\hat{a}_{b,r}^\dagger$ and $\hat{a}_{b,r}$ acting on $|b,r\rangle$.

The interaction of the bare system with the field of the two standing waves can be described by

$$\begin{aligned}\hat{H}_{int} = &\frac{\hbar\Omega_b}{2}\left(\hat{a}_b^\dagger|g\rangle\langle e| + \hat{a}_b|e\rangle\langle g|\right) \\ &+ \frac{\hbar\Omega_r}{2}\left(\hat{a}_r^\dagger|g\rangle\langle e| + \hat{a}_r|e\rangle\langle g|\right)\end{aligned} \tag{B.4}$$

using the coupling Ω_b to the blue and Ω_r to the red detuned light field.

The photons of the light fields are coherently redistributed by the interaction with the atom. The energy difference $\mathrm{d}E = 2\hbar\Delta$ is compensated by the change of kinetic energy of by the atom.

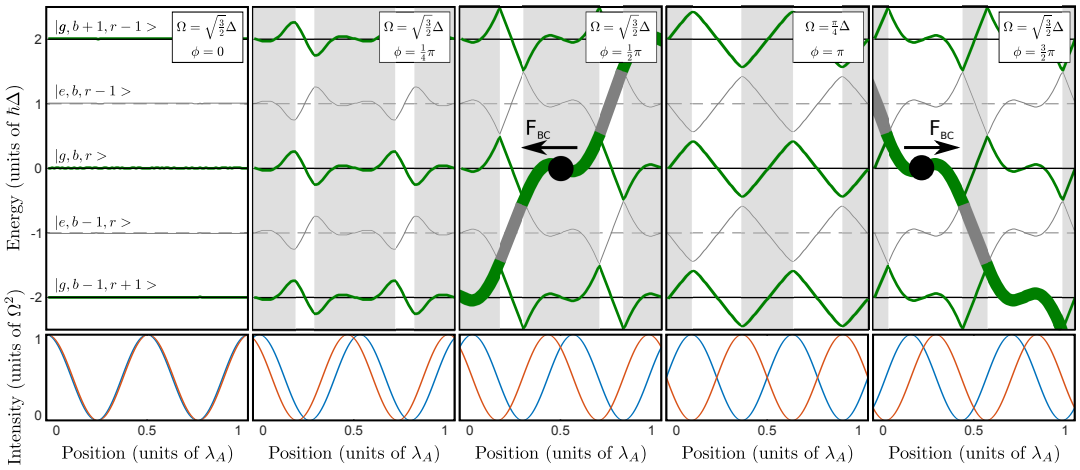

FIGURE B.1: Position-dependent energy levels of the system for different phases of the standing waves. The horizontal lines mark the uncoupled ground (solid) and excited (dashed) states. An atom will undergo transitions between the dressed states with a certain probability and will gain or lose kinetic energy in this process. The preferred direction of the bichromatic force is given by the position and the phase difference ϕ of the standing waves. For $\phi = 0$, the coupling to both modes compensate each other and the states remain uncoupled. In the case of $\phi = \frac{1}{2}\pi$, atoms which start in the shaded area of a state with larger admixture of the ground state (bold curves), will receive a force to the left side. The opposite force acts on atoms starting in the unshaded area, but due to the three-to-one ratio of the shaded area, the mean force is to the left. For $\phi = \frac{3}{4}\pi$, the sign is reversed and the average force is to the right. For $\phi = \pi$, the optimal Rabi frequency is $\Omega = \frac{\pi}{4}\Delta$, but no direction is favored. Other choices of phase difference yield non-optimal results, since the level gaps are increased. Spontaneous emission occurs more likely in the states with larger admixture to the excited state (gray curves) and will change the slope direction. However, the force is retained on average as a subsequent spontaneous emission is more likely to happen once the path has changed. Taken from (Feng et al., 2017).

The form of the coupling parameters are dependent on the chosen light fields and is

$$\Omega_{b,r}(z) = 2\Omega \cos(kz \pm \frac{\phi}{4}) \tag{B.5}$$

with wavenumber $k = 2\pi/\lambda_A$ and position z in the given case of two standing light waves with relative phase difference ϕ. Using this, the total Hamiltonian becomes

$$\hat{H}_{tot} = (b+r)\hbar\omega_A \cdot \mathbb{1}_5 + \hbar \begin{pmatrix} 2\Delta & \frac{\Omega_b}{2} & 0 & 0 & 0 \\ \frac{\Omega_b}{2} & \Delta & \frac{\Omega_r}{2} & 0 & 0 \\ 0 & \frac{\Omega_r}{2} & 0 & \frac{\Omega_b}{2} & 0 \\ 0 & 0 & \frac{\Omega_b}{2} & -\Delta & \frac{\Omega_r}{2} \\ 0 & 0 & 0 & \frac{\Omega_r}{2} & -2\Delta \end{pmatrix} \tag{B.6}$$

and the eigenenergies of the system are given by diagonalization.

Figure B.1 shows the position-dependent levels for different relative phases ϕ. A moving atom can transit through the energy levels with probability

$$P_{\mathrm{L\,Z}} = e^{-\pi U^2/\hbar v \frac{\mathrm{d}E}{\mathrm{d}z}} \tag{B.7}$$

where v is the atom velocity, U is the energy difference between the levels and $\frac{\mathrm{d}E}{\mathrm{d}z}$ the gradient of the eigenenergies.

The maximal force is given by $\Omega = \sqrt{\frac{3}{2}}\Delta$ and $\phi = \pm\frac{\pi}{2}$ and yield a force

$$F_{\mathrm{DDA}} = \frac{3}{4}\left|\frac{\mathrm{d}E}{\mathrm{d}z}\right| - \frac{1}{4}\left|\frac{\mathrm{d}E}{\mathrm{d}z}\right| = \frac{\hbar k\Delta}{\pi}. \tag{B.8}$$

Three-quarter of the atoms start in the correct state and follow the desired force direction whereas one quarter of the atoms are pushed in the opposite direction. Every spontaneous emission process with turn the direction of the force, but the choice of phase $\phi = \pm\frac{\pi}{2}$ results in a more likely subsequent spontaneous emission, restoring the direction of the force.

Appendix C

Laser System of the Test Apparatus

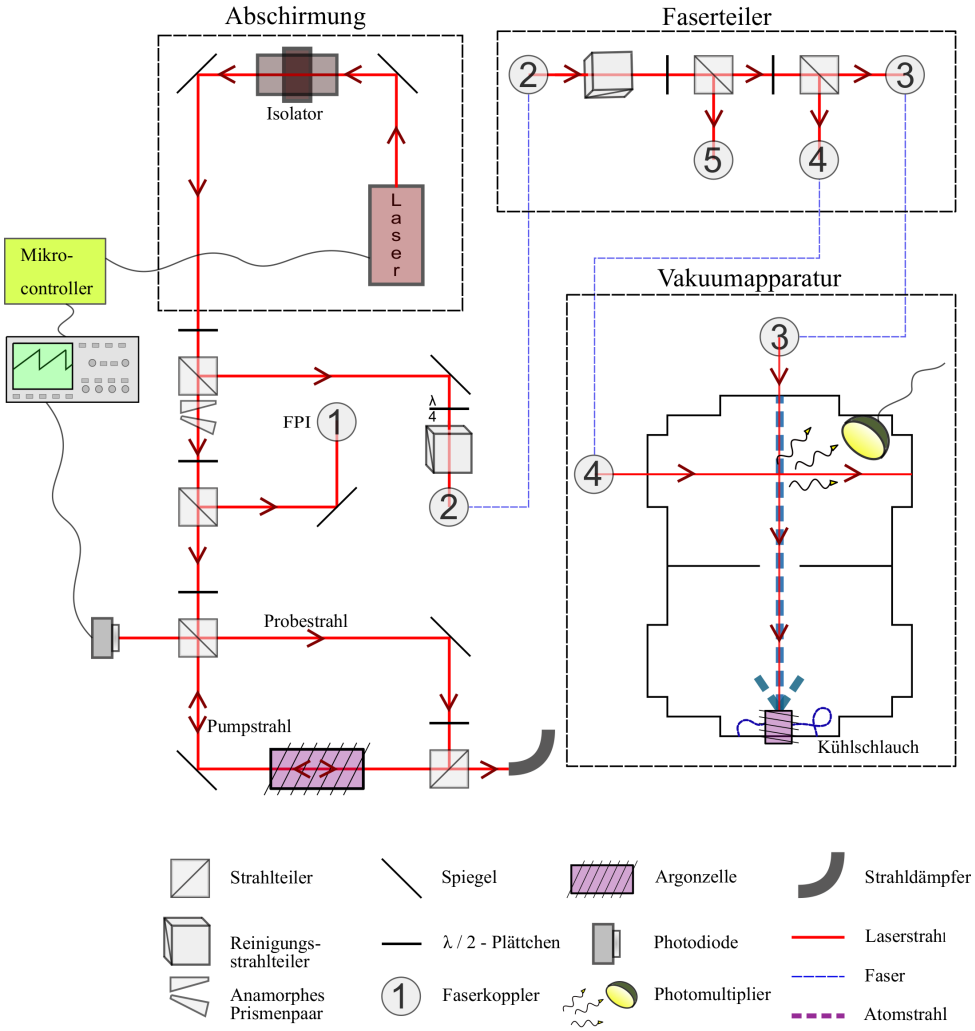

FIGURE C.1: Laser system of the test apparatus. The external-cavity diode laser (DL100) is controlled by a microcontroller (Arduino). A part of the light is analyzed with a Fabry-Pérot Interferometer (FPI) and an argon spectroscopy to have an absolute and relative frequency scale. The main part of the light is split into three fibers. One is used for the longitudinal fluorescence spectroscopy and the remaining two are placed in front of the two chambers to perform transversal absorption spectroscopy. The flux of the metastable argon source can be measured using this setup. Taken from (Hahne, 2017).

List of Own Publications

[1] Zhongyi Feng, Pascal Bohleber, Sven Ebser, Lisa Ringena, Maximilian Schmidt, Arne Kersting, Philip Hopkins, Helene Hoffmann, Andrea Fischer, Werner Aeschbach and Markus K. Oberthaler. *Dating glacier ice of the last millennium by quantum technology*. ArXiv e-prints. arXiv: 1811.03955, 2018 (currently under review).

[2] Zhongyi Feng, Sven Ebser, Lisa Ringena, Florian Ritterbusch and Markus K. Oberthaler. *Bichromatic force on metastable argon for atom-trap trace analysis*. Phys. Rev. A 96, 013424, 2017.

[3] Sven Ebser, Arne Kersting, Tim Stöven, Zhongyi Feng, Lisa Ringena, Maximilian Schmidt, Toste Tanhua, Werner Aeschbach and Markus K. Oberthaler. ^{39}*Ar dating with small samples provides new key constraints on ocean ventilation*. Nature Communications, volume 9, Article number: 5046, 2018.

Bibliography

Agnes, P. et al. (2016). "Results from the first use of low radioactivity argon in a dark matter search". In: *Phys. Rev. D* 93 (8), p. 081101. DOI: 10.1103/PhysRevD.93.081101. URL: https://link.aps.org/doi/10.1103/PhysRevD.93.081101.

Alvarado, J. A. Corcho et al. (2007). "Constraining the age distribution of highly mixed groundwater using 39Ar: A multiple environmental tracer (3H/3He, 85Kr, 39Ar, and 14C) study in the semiconfined Fontainebleau Sands Aquifer (France)". In: *Water Resources Research* 43.3, W03427. ISSN: 0043-1397 and 1944-7973.

Anderson, E.C. and W.F. Libby (1957). "The Development and Applications of Low Level Counting11Work done under the auspices of the U.S. Atomic Energy Commission." In: vol. 5. Advances in Biological and Medical Physics. Elsevier, pp. 385 –423. DOI: https://doi.org/10.1016/B978-1-4832-3111-2.50013-4. URL: http://www.sciencedirect.com/science/article/pii/B9781483231112500134.

Arnold, J. R. and W. F. Libby (1949). "Age Determinations by Radiocarbon Content: Checks with Samples of Known Age". In: *Science* 110.2869, pp. 678–680. ISSN: 0036-8075 and 1095-9203.

Beer, Jürg, Ken McCracken, and Rudolf von Steiger (2012). *Cosmogenic radionuclides. theory and applications in the terrestrial and space environments ; with ... 9 tables*. Physics of earth and space environments. Berlin ; Heidelberg [u.a.]: Springer, XVI, 426 pages. ISBN: 978-3-642-14650-3. DOI: 10.1007/978-3-642-14651-0.

Bergeman, T, G Erez, and HJ Metcalf (1987). "Magnetostatic trapping fields for neutral atoms". In: *Physical review. A, General physics* 35.4, pp. 1535–1546. ISSN: 0556-2791.

Bjorklund, G C (1980). "Frequency modulation spectroscopy: a new method for measuring weak absorptions and dispersions". In: *Optics letters* 5.1, p. 15. ISSN: 0146-9592 and 1539-4794.

Bohleber, Pascal, Helene Margarethe Hoffmann, and Johanna Katharina Kerch (2018). "Investigating cold based summit glaciers through direct access to the glacier base. a case study constraining the maximum age of Chli Titlis glacier, Switzerland". In: *The Cryosphere* 12.1, pp. 401–412. ISSN: 1994-0424. DOI: 10.5194/tc-12-401-2018. URL: http://dx.doi.org/10.5194/tc-12-401-2018.

Bonani, Georges et al. (1986). "The ETH/SIN Dating Facility: A Status Report". In: *Radiocarbon* 28.2A, pp. 246–255. ISSN: 0033-8222 and 1945-5755.

Born, M. (1926). "Zur Quantenmechanik der Stoßvorgänge". In: *Zeitschrift fur Physik* 37, pp. 863–867. DOI: 10.1007/BF01397477.

Bransden, Brian H. and Charles J. Joachain (1983). *Physics of atoms and molecules*. London: Longman, XI, 686 pages. ISBN: 0-582-44401-2 and 978-0-582-44401-0.

Bronk Ramsey, C (2017). *OxCal 4.3. 2. 2017*.

Buchholz, Bruce A. (2009). *Radiocarbon Dating*. American Cancer Society. ISBN: 978-0-470-06158-9. DOI: 10.1002/9780470061589.fsa608. eprint: https://onlinelibrary.wiley.com/doi/pdf/10.1002/9780470061589.fsa608. URL: https://onlinelibrary.wiley.com/doi/abs/10.1002/9780470061589.fsa608.

Buizert, Christo et al. (2014). "Radiometric 81Kr dating identifies 120,000-year-old ice at Taylor Glacier, Antarctica". In: *Proceedings of the National Academy of Sciences* 111.19, p. 6876. ISSN: 0027-8424 and 1091-6490.

CC BY-SA 3.0 (2018). *File:Gletscherschmelze.jpg*. [Online; accessed 13-September-2018 under licence CC BY-SA 3.0]. URL: https://commons.wikimedia.org/w/index.php?curid=469600.

Chen, C. Y. et al. (1999). "Ultrasensitive Isotope Trace Analyses with a Magneto-Optical Trap". In: *Science* 286.5442, pp. 1139–1141. ISSN: 0036-8075 and 1095-9203.

Cohen-Tannoudji, Claude, Bernard Diu, and Franck Laloë (1977). *Quantum mechanics*. Wiley-Interscience publication. New York [u.a.]: Wiley [u.a.] ISBN: 978-0-471-56952-7.

Collon, Philippe, Walter Kutschera, and Zheng-Tian Lu (2004). "TRACING NOBLE GAS RADIONUCLIDES IN THE ENVIRONMENT". In: *Annual Review of Nuclear and Particle Science* 54.1, pp. 39–67. ISSN: 0163-8998 and 1545-4134.

Dalibard, J. and C. Cohen-Tannoudji (1989). "Laser cooling below the Doppler limit by polarization gradients: simple theoretical models". In: *J. Opt. Soc. Am. B* 6.11, pp. 2023–2045. DOI: 10.1364/JOSAB.6.002023. URL: http://josab.osa.org/abstract.cfm?URI=josab-6-11-2023.

Dickin, Alan P. (2018). *Radiogenic isotope geology*. Third edition. Cambridge: Cambridge University Press, xvi, 482 pages. ISBN: 978-1-107-09944-9 and 978-1-107-49212-7.

Dobrovolný, Petr et al. (2010). "Monthly, seasonal and annual temperature reconstructions for Central Europe derived from documentary evidence and instrumental records since AD 1500". In: *Climatic Change* 101.1, pp. 69–107. ISSN: 0165-0009 and 1573-1480.

Ebser, Sven (2018). *Dating of ice and ocean samples with atom trap trace analysis of 39Ar*. Heidelberg, Online–Ressource (viii, 158 pages). DOI: 10.11588/heidok.00024512. URL: http://nbn-resolving.de/urn:nbn:de:bsz:16-heidok-245121.

Ebser, Sven et al. (2018). "39Ar dating with small samples provides new key constraints on ocean ventilation". In: *Nature Communications* 9.1. ISSN: 2041-1723 and 2041-1723.

Ehrenfest, P. (1927). "Bemerkung über die angenäherte Gültigkeit der klassischen Mechanik innerhalb der Quantenmechanik". In: *Zeitschrift für Physik* 45.7, pp. 455–

457. ISSN: 0044-3328. DOI: 10.1007/BF01329203. URL: https://doi.org/10.1007/BF01329203.

Feng, Z. et al. (2018). "Dating glacier ice of the last millennium by quantum technology". In: *ArXiv e-prints*. arXiv: 1811.03955.

Feng, Zhongyi (2012). "Implementierung einer Atomflussüberwachung für 39Ar ATTA". Bachelors thesis. Heidelberg University.

Feng, Zhongyi et al. (2017). "Bichromatic force on metastable argon for atom trap trace analysis". In: *Physical review* 96(2017. ISSN: 1094-1622. DOI: 10.1103/PhysRevA.96.013424.

Gierlich, Timo (2017). "Design of a fiber coupled argon laser spectroscopy and investigation of the metastable density in an RF source". Bachelors thesis. Heidelberg University.

Griffiths, David J. (1995). *Introduction to quantum mechanics*. Upper Saddle River, NJ: Prentice Hall, IX, 394 pages. ISBN: 0-13-124405-1 and 0-13-185513-1 and 978-0-13-185513-7 and 978-0-13-124405-4.

Grimm, R et al. (1990). "Observation of a strong rectified dipole force in a bichromatic standing light wave". In: *Physical review letters* 65.12, pp. 1415–1418. ISSN: 0031-9007 and 1079-7114.

Haeberli, Wilfried and Jürg Alean (1985). "Temperature and Accumulation of High Altitude Firn in the Alps". In: *Annals of Glaciology* 6, pp. 161–163. ISSN: 0260-3055 and 1727-5644.

Haeberli, Wilfried et al. (2004). "Characteristics and potential climatic significance of "miniature ice caps" (crest- and cornice-type low-altitude ice archives)". In: *Journal of Glaciology* 50.168, pp. 129–136. ISSN: 0022-1430 and 1727-5652.

Hahne, Felix (2017). "Stabilisierung und Implementierung einer Echtzeit Flussbestimmung von metastabilem Argon". Bachelors thesis. Heidelberg University.

Hickman, G T, J D Franson, and T B Pittman (2016). "Optically enhanced production of metastable xenon". In: *Optics letters* 41.18, p. 4372. ISSN: 0146-9592 and 1539-4794.

Hippel, Frank von, David H. Albright, and Barbara G. Levi (1985). "Stopping the Production of Fissile Materials for Weapons". In: *Scientific American* 253.3, pp. 40–47. ISSN: 0036-8733 and 1946-7087.

Hoffmann, Helene et al. (2018). "A New Sample Preparation System for Micro-14C Dating of Glacier Ice with a First Application to a High Alpine Ice Core from Colle Gnifetti (Switzerland)". In: *Radiocarbon* 60.2, pp. 517–533. ISSN: 0033-8222 and 1945-5755.

Hoffmann, Helene Margarethe (2016). *Micro radiocarbon dating of the particulate organic carbon fraction in Alpine glacier ice*. Heidelberg, Online–Ressource (184 pages). URL: http://nbn-resolving.de/urn:nbn:de:bsz:16-heidok-207128.

Hopkins, Philip (2018). "Setting up a new argon separation system for glacier ice and ocean water dating". Masters thesis. Heidelberg University.

http://www.leibniz.uni-kiel.de (2018). *Leibniz Price*. [Online;accessed 2018/11/28]. URL: https://www.leibniz.uni-kiel.de/en/ams-14c-lab/price-and-time.

http://www.radiocarbon.org (2018). *Radiocarbon Laboratories*. [Online; accessed 2018/11/28]. URL: http://www.radiocarbon.org/Info/Labs.pdf.

Hänsch, Theodor W., Arthur L. Schawlow, and George W. Series (1979). "The Spectrum of Atomic Hydrogen". In: *Scientific American* 240.3, pp. 94–111. ISSN: 00368733, 19467087. URL: http://www.jstor.org/stable/24965154.

Jian, Wei (2018). "New developments at the Laboratory for Radiokrypton and Radioargon Dating at USTC". Talk at the 3rd International Workshop on Tracer Applications of Noble Gas Radionuclides.

Jiang, W et al. (2012). "An atom counter for measuring 81Kr and 85Kr in environmental samples". In: *Geochimica et Cosmochimica Acta* 91, pp. 1–6. ISSN: 0016-7037 and 1872-9533.

Kohler, M et al. (2014). "All optical production and trapping of metastable noble gas atoms down to the single atom regime". In: *EPL (Europhysics Letters)* 108. DOI: 10.1209/0295-5075/108/13001.

Kromer, Bernd et al. (2013). "MAMS: A new AMS facility at the Curt-Engelhorn-Centre for Archaeometry, Mannheim, Germany". In: *Nuclear Instruments and Methods in Physics Research Section B: Beam Interactions with Materials and Atoms* 294, 11–13. DOI: 10.1016/j.nimb.2012.01.015.

Kutschera, W. et al. (1994). "Long-lived noble gas radionuclides". In: *Nuclear Instruments and Methods in Physics Research Section B: Beam Interactions with Materials and Atoms* 92.1, pp. 241 –248. ISSN: 0168-583X. DOI: https://doi.org/10.1016/0168-583X(94)96013-5. URL: http://www.sciencedirect.com/science/article/pii/0168583X94960135.

Lett, PD et al. (1988). "Observation of atoms laser cooled below the Doppler limit". In: *Physical review letters* 61.2, pp. 169–172. ISSN: 0031-9007 and 1079-7114.

Libby, W. F., E. C. Anderson, and J. R. Arnold (1949). "Age Determination by Radiocarbon Content: World Wide Assay of Natural Radiocarbon". In: *Science* 109.2827, pp. 227–228. ISSN: 0036-8075 and 1095-9203.

Lieberman, Michael A. and Allan J. Lichtenberg (1994). *Principles of plasma discharges and materials processing*. A Wiley-Interscience publication. Includes bibliographical references (pages 559 - 564) and index. New York [u.a.]: Wiley, XXVI, 572 pages. ISBN: 0-471-00577-0 and 978-0-471-00577-3.

Loosli, H.H. (1983). "A dating method with39Ar". In: *Earth and Planetary Science Letters* 63.1, pp. 51 –62. ISSN: 0012-821X. DOI: https://doi.org/10.1016/0012-821X(83)90021-3. URL: http://www.sciencedirect.com/science/article/pii/0012821X83900213.

Loosli, H.H. and H. Oeschger (1969). "37Ar and81Kr in the atmosphere". In: *Earth and Planetary Science Letters* 7.1, pp. 67 –71. ISSN: 0012-821X. DOI: https://doi.org/10.1016/0012-821X(69)90014-4. URL: http://www.sciencedirect.com/science/article/pii/0012821X69900144.

Lu, Z.-T et al. (2014). "Tracer applications of noble gas radionuclides in the geosciences". In: *Earth-Science Reviews* 138, pp. 196–214. ISSN: 0012-8252 and 1872-6828.

LUBW (1992). "Grundwasser Überwachungsprogramm". In: Online–Ressource. URL: http://www.bibliothek.uni-regensburg.de/ezeit/?2461075.

Martinelli, R et al. (2003). "Measuring fast neutrons in Hiroshima at distances relevant to atomic-bomb survivors". In: *Nature* 424.6948, pp. 539–542. ISSN: 0028-0836 and 1476-4687.

Mazor, E (1972). "Paleotemperatures and other hydrological parameters deduced from noble gases dissolved in groundwaters; Jordan Rift Valley, Israel". In: *Geochimica et Cosmochimica Acta* 36.12, pp. 1321–1336. ISSN: 0016-7037 and 1872-9533.

McDougall, Ian and T. Mark Harrison (1988). *Geochronology and thermochronology by the 40Ar/39Ar method*. Oxford monographs on geology and geophysics ARRAY(0x4edcb78). pages 191 - 212. New York [u.a.]: Oxford Univ. Press [u.a.], XI, 212 pages. ISBN: 0-19-504302-2 and 978-0-19-504302-0.

Metcalf, Harold J. and Peter van Straten (1999). *Laser cooling and trapping*. Graduate texts in contemporary physics. New York ; Berlin ; Heidelberg [u.a.]: Springer, XVI, 323 pages. ISBN: 0-387-98747-9 and 0-387-98728-2 and 978-0-387-98728-6 and 978-0-387-98747-7.

Meyer, Leo et al. (2014). *IPCC, 2014: Climate Change 2014: Synthesis Report. Contribution of Working Groups I, II and III to the Fifth Assessment Report of the Intergovernmental Panel on Climate Change*. Tech. rep. Geneva, Switzerland, pp. 3–87.

Möller, Detlev (2003). *Luft. Chemie, Physik, Biologie, Reinhaltung, Recht*. Berlin [u.a.]: de Gruyter, XXIII, 750 pages. ISBN: 3-11-016431-0 and 978-3-11-016431-2.

Nicolai, Florian (2017). "Design and construction of a fiber coupled tapered amplifier system". MA thesis. Heidelberg University.

Oeschger, H. et al. (1974). "^{39}Ar dating of goundwater". In: *Isotope Techniques in Groundwater Hydrology 1974* IAEA Vienna, pp. 179 –190.

Oeschger, H et al. (1976). "Extraction of Trace Components from Large Quantities of Ice in Bore Holes". In: *Journal of Glaciology* 17.75, pp. 117–128. ISSN: 0022-1430 and 1727-5652.

Ohayon, Ben and Guy Ron (2015). "Investigation of different magnetic field configurations using an electrical, modular Zeeman slower". In: *The Review of scientific instruments* 86.10, p. 103110. ISSN: 0034-6748 and 1089-7623.

Ohno, Hiroshi, Vladimir Y. Lipenkov, and Takeo Hondoh (2004). "Air bubble to clathrate hydrate transformation in polar ice sheets: A reconsideration based on the new data from Dome Fuji ice core". In: *Geophysical Research Letters* 31.21, L21401–n/a. ISSN: 0094-8276 and 1944-8007.

Ovchinnikov, Yu.B et al. (1993). "Rectified dipole force in a bichromatic standing light wave". In: *Optics Communications* 102.1, pp. 155–165. ISSN: 0030-4018 and 1873-0310.

Ozima, Minoru and Frank A. Podosek (1983). *Noble gas geochemistry*. pages [339] - 358. Cambridge [u.a.]: Univ. Pr., X, 367 pages. ISBN: 0-521-23939-7 and 978-0-521-23939-4.

Phelps, A. V. and J. P. Molnar (1953). "Lifetimes of Metastable States of Noble Gases". In: *Phys. Rev.* 89 (6), pp. 1202–1208. DOI: 10.1103/PhysRev.89.1202. URL: https://link.aps.org/doi/10.1103/PhysRev.89.1202.

Phillips, William D and Harold Metcalf (1982). "Laser Deceleration of an Atomic Beam". In: *Physical Review Letters* 48.9, pp. 596–599. ISSN: 0031-9007 and 1079-7114.

Pritchard, David E (1983). "Cooling Neutral Atoms in a Magnetic Trap for Precision Spectroscopy". In: *Physical Review Letters* 51.15, pp. 1336–1339. ISSN: 0031-9007 and 1079-7114.

Rayleigh, L and W Ramsay (1895). "Argon, a new constituent of the atmosphere". In: *American Journal of Science* s3-49.292, pp. 275–296. ISSN: 0002-9599 and 1945-452X.

Reimer, Paula J et al. (2013). "IntCal13 and Marine13 Radiocarbon Age Calibration Curves 0–50,000 Years cal BP". In: *Radiocarbon* 55.4, pp. 1869–1887. ISSN: 0033-8222 and 1945-5755.

Ricci, L et al. (1995). "A compact grating stabilized diode laser system for atomic physics". In: *Optics Communications* 117.5, pp. 541–549. ISSN: 0030-4018 and 1873-0310.

Ritterbusch, F et al. (2014). "Groundwater dating with Atom Trap Trace Analysis of 39Ar". In: *Geophysical Research Letters* 41.19, pp. 6758–6764. ISSN: 0094-8276 and 1944-8007.

Ritterbusch, Florian (2014). *Dating of groundwater with atom trace of analysis of 39Ar*, Online–Ressource (120 pages). URL: http://archiv.ub.uni-heidelberg.de/volltextserver/16651/.

Roedel, Walter and Thomas Wagner (2017). *Physik unserer Umwelt: Die Atmosphäre*. 5. Aufl. 2017. SpringerLink : Bücher. Berlin, Heidelberg: Springer Spektrum, Online–Ressource (XV, 597 pages 222 Abb., 7 Abb. in Farbe, online resource). ISBN: 978-3-662-54258-3. DOI: 10.1007/978-3-662-54258-3. URL: http://dx.doi.org/10.1007/978-3-662-54258-3.

Scheck, Florian (2007). *Quantum physics*. Berlin ; Heidelberg [u.a.]: Springer, XV, 738 pages. ISBN: 978-3-540-25645-8 and 3-540-25645-8. URL: http://deposit.dnb.de/cgi-bin/dokserv?id=2668739&prov=M&dok%5Fvar=1&dok%5Fext=htm.

Schlosser, Peter et al. (1987). "Measurement of Small Volume Oceanic 14C Samples by Accelerator Mass Spectrometry". In: *Radiocarbon* 29.3, pp. 347–352. ISSN: 0033-8222 and 1945-5755.

Schünemann, U et al. (1999). "Simple scheme for tunable frequency offset locking of two lasers". In: *Review of Scientific Instruments* 70.1, pp. 242–243. ISSN: 0034-6748 and 1089-7623.

Sears, Wheeler M. (2015). *Helium. The Disappearing Element*. SpringerLink : Bücher. Cham: Springer, Online–Ressource (XIII, 138 p. 37 illus., 9 illus. in color, online

resource). ISBN: 978-331-91512-3-6. DOI: 10.1007/978-3-319-15123-6. URL: http://dx.doi.org/10.1007/978-3-319-15123-6.

Seinfeld, John H. and Spyros N. Pandis (2016). *Atmospheric chemistry and physics. from air pollution to climate change*. Third edition. Hoboken, New Jersey: Wiley, xxvi, 1120 pages. ISBN: 1-118-94740-1 and 978-1-118-94740-1.

Söding, J et al. (1997). "Short Distance Atomic Beam Deceleration with a Stimulated Light Force". In: *Physical Review Letters* 78.8, pp. 1420–1423. ISSN: 0031-9007 and 1079-7114.

Sturchio, N. C. et al. (2004). "One million year old groundwater in the Sahara revealed by krypton-81 and chlorine-36". In: *Geophysical Research Letters* 31.5, L05503–n/a. ISSN: 0094-8276 and 1944-8007.

Ungar, P. J. et al. (1989). "Optical molasses and multilevel atoms: theory". In: *J. Opt. Soc. Am. B* 6.11, pp. 2058–2071. DOI: 10.1364/JOSAB.6.002058. URL: http://josab.osa.org/abstract.cfm?URI=josab-6-11-2058.

Wacker, L et al. (2010). "MICADAS: Routine and High Precision Radiocarbon Dating". In: *Radiocarbon* 52.2, pp. 252–262. ISSN: 0033-8222 and 1945-5755.

Warneck, Peter (1988). *Chemistry of the natural atmosphere*. International geophysics series ARRAY(0x48b0b28). San Diego [u.a.]: Academic Pr., XIII, 757 pages. ISBN: 0-12-735630-4 and 978-0-12-735630-3.

Welte, J et al. (2009). "Hyperfine spectroscopy of the 1s5 to 2p9 transition of Ar39". In: *Review of Scientific Instruments* 80.11, pp. 113109–113109–4. ISSN: 0034-6748 and 1089-7623.

Welte, Joachim (2011). *Atom trap trace analysis of Ar-39*, Online–Ressource (X, 119 pages). URL: http://archiv.ub.uni-heidelberg.de/volltextserver/volltexte/2012/12936.

Williams, R.M et al. (2017). "Development of a low-level 39Ar calibration standard – Analysis by absolute gas counting measurements augmented with simulation". In: *Applied Radiation and Isotopes* 126, pp. 243–248. ISSN: 0969-8043 and 1872-9800.

Woelfli, Willy et al. (1983). "Radioisotope Dating with the ETHZ EN Tandem Accelerator". In: *Radiocarbon* 25.2, pp. 745–753. ISSN: 0033-8222 and 1945-5755.

Young, L, D Yang, and R W Dunford (2002). "Optical production of metastable krypton". In: *Journal of Physics B: Atomic, Molecular and Optical Physics* 35.13, pp. 2985–2992. ISSN: 0953-4075 and 1361-6455.

Zappala, J.C et al. (2017). "Setting a limit on anthropogenic sources of atmospheric 81Kr through Atom Trap Trace Analysis". In: *Chemical Geology* 453, pp. 66–71. ISSN: 0009-2541 and 1872-6836.